Università degli Studi di Cagliari
Dipartimento di Ingegneria Meccanica
Dottorato di Ricerca in Progettazione Meccanica
XX Ciclo - Ing-Ind/09

CFD-RANS Study of Horizontal Axis Wind Turbines

Thesis for the degree of Doctor of Philosophy

Carlo Enrico Carcangiu

Supervisors:
Prof. Natalino Mandas
Dr. Francesco Cambuli

January 2008

Thesis for the degree of Doctor of Philosophy
by **Carlo Enrico Carcangiu**
Printed in Italy, Cagliari, 2008

Dipartimento di Ingegneria Meccanica, DIMeCa
Università degli Studi di Cagliari
Piazza d'Armi, 1
09123 Cagliari, Italy
carcangiu@dimeca.unica.it

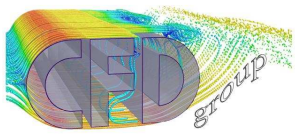

This thesis has been written in *British English* and typeset in LaTeX 2_ε. Illustrations were drawn with MsOffice, graphs and plots were created with MsExcel, Matlab and TecPlot.

(Front cover illustration shows a view of the Middelgrunden 40 MW off-shore wind farm, near Copenhagen, Denmark)

Our universe is a sea of energy - free, clean energy.
It is all out there waiting for us to set sail upon it.

Robert Adams

Vestas V52–850 kW Monte Guzzini wind farm in Sardinia ITALY

Preface

This thesis is submitted in partial fulfilment of the requirements for the degree of Philosophiæ Doctor in Mechanical Engineering from Università degli Studi di Cagliari.

The research work was carried out during the period from January 2005 to December 2007 at the Department of Mechanical Engineering - University of Cagliari (DIMeCa), and from September 2006 to April 2007 as a guest at the Department of Mechanical Engineering (MEK), Fluid Mechanics Section of the Technical University of Denmark (DTU). The visiting period at DTU was also supported by DCAMM, the Danish Center for Applied Mechanics and Mathematics.

Subject of this dissertation are modern wind turbines. On the matter, many people in recent times have expressed their personal opinions. No more than a mere point of view, a comment on aesthetics, and occasionally partial judgements were given by politicians, scientists as well as common people against wind energy exploring technologies. So, prior to dive into the technical discussion, which hopefully will be objective, let us say our personal opinion too. We like modern windmills and we think their presence in our landscape can be a view of civilization, of which too often one feels the lack in modern society.

I wish to express my sincere thanks to Professor Natalino Mandas, who has carefully supervised my PhD project, and more because I owe to him the interest for fluid dynamics and wind energy issues. He gave me the chance to spend these three years on the research within this field, he has always trusted in me and encouraged me all along.

I am grateful to Dr Francesco Cambuli, who has co-supervised this work. Like no other, he has constantly provided me helpful suggestions and has held with me valuable discussions on fluid mechanics, numerical issues...and else more! His friendly and patient support has been simply essential.

I wish my thanks to the CFD-GROUP: Giorgio C., Giorgio M., Marco, and Roberto. I will never forget the good times we spent together (underground) in the "Supersonica" Lab. I also extend my thanks to the other colleagues and friends at the DIMECA.

I would like to greatly thank Professor Jens Norkær Sørensen, who gave me the opportunity to work on the rotational effects project at DTU, for his

constant support and for sharing his great knowledge and experience in that field. Also, I wish to extend my thanks to everybody at DTU/MEK for making me feel welcome during my stay there, and especially to Clara, Gabriel, Niels and Wei Jun.

A warm thank to the "danish" friends Diego, Francesco, Luca, Marianna, Matteo, Poly, Rafael, Ulrik, and to Pinuccia and Torben for their kind hospitality.

Finally, I would thank my parents Carmen e Ivo, my grandparents and all my family that have always supported me, thanks to the "old" friends who never let me down, and devote thanks to Francesca, for her love and firm support.

Cagliari, 2008 January 23rd

Carlo Enrico

Abstract

This PhD project concerns the study of wind turbine aerodynamics with a CFD–RANS approach.

Nowadays, industrial design codes for wind turbines are still based on the BEM (Blade Element Momentum) method, which has been extended with a number of empirical correction, often not based on physical flow features. The importance of accurate design does also increase as the machines tend to become larger. Therefore, the research is today focused more on the basic aerodynamic mechanisms.

The general aim of this project was to get a better understanding of the physical behaviour of the flow field past wind turbine rotors, including the boundary layer flow as well as the wake region. Although CFD is not a practical design tool, useful suggestions for classical design methods can be derived from the analysis.

A full three–dimensional CFD–RANS approach was used, modelling the whole rotor of a wind turbine by means of periodicity and in a moving reference system. All the simulations were performed using the finite–volume solution package Fluent®. A detailed selection of results is presented, dealing with the various investigated issues. A first validation of the computational methods was done by comparing the overall power production of a BEM-designed turbine. The most important features of the investigated machines were captured with CFD, so that a broad review of wind turbine aerodynamics was given, through the post processing of the computed solutions. A study on the blade root and tip was carried out, allowing to demonstrate the advantages of some recent improvements in rotor blade design, and showing the capabilities of CFD as an optimization method. Both the near and far wake were also analysed. Finally, the rotational effect on the boundary layer of rotating blades were studied, with generating a complete solution database and a post–processing tool. Further advancements are required, for stating more about the complex issues, as wake dynamics and rotational effects are. Nevertheless, the purpose of proving the capabilities of full–3D CFD–RANS for the study wind turbine aerodynamics has been fully achieved.

Key words: wind energy, wind turbine aerodynamics, CFD–RANS, blade design, wakes, rotating boundary layer.

Sommario

Scopo generale del progetto è lo studio completo e dettagliato del comportamento aerodinamico delle pale di turbina eolica ad asse orizzontale, realizzando la simulazione numerica del problema fluidodinamico mediante l'utilizzo di un codice Navier-Stokes ai volumi finiti.

La conversione dell'energia del vento in energia meccanica deve avvenire con il più alto rendimento possibile, in modo da diminuire i costi di produzione e renderla competitiva con le fonti di energia tradizionali. Nell'ultimo decennio la ricerca nel settore ha consentito un miglioramento sostanziale della efficienza globale, tanto che attualmente l'energia eolica è sicuramente in prima posizione tra le fonti rinnovabili per competitività. Tuttavia ci sono ancora sensibili margini di miglioramento soprattutto nella progettazione aerodinamica del rotore, che rappresenta di per sé un problema complesso, tuttora oggetto di studio.

L'analisi del campo di moto di una turbina eolica può essere realizzata secondo diversi approcci: quello sperimentale, con campagne di misurazione effettuate sul campo o in galleria a vento, che risulta estremamente complesso; l'analisi mediante modelli fluidodinamici semi-empirici, tra i quali il metodo BEM (*Blade Element Momentum*) è tuttora quello più usato, con ipotesi semplificative che li rendono non universalmente attendibili; infine la CFD (*Computational Fluid Dynamic*s), che rappresenta l'alternativa preferibile alle misurazioni dirette.

Il progetto di ricerca sviluppato si prefiggeva pertanto di verificare le potenzialità delle moderne tecniche di simulazione numerica applicate a tale problema fluidodinamico complesso. Il lavoro si articola in diverse fasi, che sono state sviluppate prevalentemente secondo la sequenza indicata di seguito, benché sia evidente la interdipendenza e consequenzialità delle stesse:

1. studio della logica di modellazione del rotore di una turbina eolica di media taglia e del suo campo di moto. Scelta della geometria e dimensionamento secondo il metodo BEM;

2. simulazione del flusso attorno al modello per diverse condizioni di flusso e verifica delle prestazioni globali relativamente ai metodi di progetto di tipo BEM (validazione);

3. applicazione delle simulazioni numeriche al progetto: studio e ottimizzazione del disegno della radice e dell'apice delle pale di turbina;

4. analisi del flusso di scia;

5. studio degli effetti rotazionali sullo strato limite delle pale.

I progressivi stati di avanzamento del lavoro, descritti dalle fasi sopraelencate, sono stati presentati su riviste scientifiche e conferenze nazionali ed internazionali e vengono riassunti nel seguito.

In primo luogo è stata individuata la geometria della macchina. Si è scelto di progettare una turbina eolica di media taglia (Potenza nominale = 500 kW, Diametro del rotore = 41 m, rotore tripala) seguendo il metodo BEM. Quindi si è valutata la configurazione del dominio e della griglia di calcolo. Il dominio consiste in un unico vano palare, con la pala al proprio interno escludendo la torre di sostegno ed il terreno. La griglia di calcolo utilizzata, di tipo strutturato, è particolarmente curata in prossimità del profilo palare, seguendo una configurazione a C, per la risoluzione corretta dello strato limite e, allo stesso tempo, si estende notevolmente a valle del disco rotorico, per rilevare conformemente lo sviluppo della scia. Ipotizzato un flusso incomprimibile e turbolento-stazionario, il modello numerico è costituito dalle equazioni RANS e dai modelli di turbolenza di Spalart-Allmaras e k–ω SST. Il flusso è stato risolto rispetto ad un sistema di riferimento non inerziale solidale con la girante, in modo da ottenere condizioni di flusso relativo stazionario. Il modello è stato studiato per diverse condizioni operative, simulando valori variabili della velocità del vento.

Il confronto tra i risultati ottenuti e i valori ricavati con il metodo BEM ha permesso di verificare con buon accordo la validità della procedura adottata. Attraverso una indagine qualitativa delle caratteristiche del campo di moto è stato altresì possibile rilevare la conformità fisica del campo di moto simulato con analoghe osservazioni rilevate nella letteratura.

In seguito è stata approfondita l'analisi di alcune regioni della pala di particolare rilevanza per il comportamento aerodinamico dell'intero rotore. Si è quindi dedicata particolare attenzione alla possibilità di migliorare le prestazioni della macchina profilando aerodinamicamente le pale anche nella zona prossima al mozzo. In tal modo è possibile recuperare l'energia altrimenti persa in questa zona del rotore, che per le macchine di grossa taglia rappresenta una quota di perdita tutt'altro che trascurabile. In tale zona è infatti presente solitamente un tratto di pala a sezione cilindrica, in modo da garantire la stabilità strutturale anche a discapito del comportamento aerodinamico. La geometria della macchina è stata quindi modificata in analogia con alcune macchine moderne, che presentano una sezione palare profilata aerodinamicamente anche in prossimità della radice. I risultati ottenuti hanno permesso di valutare il contributo di tale porzione delle pale, attraverso il confronto con un rotore di configurazione tradizionale, studiato precedentemente con la stessa metodologia e si è evidenziato un contributo addizionale dell'ordine di circa 5%

alla produzione di potenza della macchina in condizioni nominali. Lo studio successivo ha riguardato il flusso all'apice della pala, ai fini di un miglioramento possibile in termini di coefficiente di potenza e comportamento strutturale. È stata realizzata la simulazione numerica del flusso attorno alla turbina per differenti configurazioni della geometria all'apice della pala, *i.e.* semplificata e di derivazione commerciale.

L'apice della pala è stato analizzato separatamente per le due configurazioni indicate, trascurando in primo approccio gli effetti dovuti alla rotazione. Quindi, sfruttando la periodicità della geometria, il dominio di calcolo è stato esteso ad un settore della turbina, comprendente al suo interno un'unica pala e considerato in rotazione analogamente a quanto fatto per le precedenti analisi. I risultati ottenuti hanno permesso di valutare in maniera critica l'influenza della geometria all'apice della pala sul campo di moto attorno alla turbina e di indicare la soluzione preferibile tra quelle proposte.

Di estrema importanza risulta inoltre la previsione del flusso a valle del rotore, sia per una corretta disposizione delle macchine in un parco eolico, sia per poter valutare i carichi dinamici a cui le macchine sotto scia sono sottoposte. Per poter descrivere il flusso a valle del rotore il dominio di calcolo è stato esteso in direzione assiale sino a 15 volte il diametro del rotore e a 5 diametri rotorici in direzione radiale, rendendo minima così l'influenza delle condizioni al contorno. Le simulazioni hanno permesso innanzitutto di valutare le prime fasi di sviluppo della scia generata dalla turbina così come, valutando le mappe di velocità assiale, si è individuato il passaggio a far wake, laddove l'intervento dei fenomeni diffusivi fa espandere la sezione complessiva della scia e rende omogeneo il nucleo centrale della stessa, prima segnato dal passaggio delle singole pale. Quindi si è descritto l'andamento del deficit di velocità, la cui conoscenza riveste grande importanza per la disposizione delle turbine in un parco eolico, confermando qualitativamente i risultati attesi dalle analisi svolte in letteratura. Infine è stato descritto il sistema di vortici generato dalla turbina eolica, mostrando una discreta corrispondenza con la struttura classica del sistema vorticoso ricavata sulla base di mere considerazioni teoriche.

L'ultima fase è stata sviluppata durante un periodo di studio di 8 mesi realizzato presso la Technical University of Denmark (DTU) di Lyngby, Danimarca. L'attività di ricerca ha riguardato alcuni aspetti più specifici del comportamento aerodinamico delle macchine eoliche. Si è cioè rivolta l'attenzione agli effetti rotazionali che intervengono nello strato limite delle pale. Tali fenomeni sono di grande importanza per la corretta previsione dei carichi aerodinamici sulle pale, in quanto alterano il comportamento dei profili alari rispetto alle caratteristiche bidimensionali, di cui si fa ampio utilizzo per il progetto e la verifica di queste macchine. Inoltre, benché l'osservazione di tali effetti rotazionali sia stata documentata con studi teorici, sperimentali e simulazioni numeriche, rimane ancora incompleta l'indagine sulle cause fisiche. Ad una fase di modellazione numerica del problema fluidodinamico si è affiancata l'analisi dei risultati a mezzo di opportuni strumenti di post-processing. La modellazione ha previsto la realizzazione di una geometria semplificata in

una prima fase e quindi di un rotore esistente in una seconda, mentre per la definizione del dominio, la generazione della griglia e la scelta del modello matematico si è proceduto secondo la logica già descritta. Per l'analisi dei risultati si è sviluppato uno strumento dedicato, costituito da un codice di calcolo per la valutazione delle grandezze fondamentali del campo di moto e dei parametri dello strato limite nel sistema di riferimento locale rotante. L'analisi fornita ha consentito di conseguire una migliore comprensione fisica dei fenomeni in esame e di produrre delle indicazioni utili per lo sviluppo di correzioni delle caratteristiche aerodinamiche dei profili alari, da impiegarsi in seguito nei metodi di progetto di tipo BEM. Tenendo conto in particolare dei valori del rapporto di solidità locale (corda/raggio), oltre che della velocità angolare di rotazione, si potranno infatti costruire delle relazioni tra i valori dei coefficienti di portanza e di resistenza valutati sulle pale 3-D in rotazione e i valori 2-D solitamente impiegati nel progetto BEM.

List of Symbols

Roman letters

a	axial induction-factor	
a'	tangential induction-factor	
A	Cross–section area	[m^2]
B	Number of blades	
C, c	Chord length	[m]
C_D	Drag coefficient	
C_L	Lift coefficient	
C_p	Pressure coefficient	
C_P	Power coefficient	
C_T	Thrust coefficient	
D	Drag force	[N m^{-1}]
e	Energy per unit mass	[J/kg]
E	Energy	[J]
F	Force	[N]
L	Lift force	[N m^{-1}]
$\dot{m}$	Mass flow	[kg s^{-1}]
M	Torque	[N m]
p	Pressure	[Pa]
P, P_0	Power, Rated power	[W]
Q	Volume flow	[m^3 s^{-1}]
R, r	Radius, local radius	[m]
Re	Reynolds number	
t	Time	[s]
T	Thrust	[N]
u, U	Velocity	[m/s]
U_∞, V_0	Undisturbed wind velocity	[m s^{-1}]
V	Volume	[m^3]
x, y, z	Cartesian coordinates	
θ, y, r	Cylindrical coordinates	
w	Induced velocity	[m/s]

y^+	Non-dimensional distance of the first grid point from the wall

Greek letters

α	Angle–Of–Attack	[deg]
β	Pitch angle	[deg]
δ	Boundary layer thickness	[m]
γ	Flow angle	[deg]
Γ	Circulation	[m^2/s]
λ	Tip speed ratio $= \omega R/V_0$	
ν	Kinematic viscosity	[m^2/s]
κ	Turbulent kinetic energy	[$m^2\ s^{-2}$]
μ	Dynamic viscosity	[Pa s]
θ	Twist angle	[deg]
θ, r, y	Cylindrical coordinates (tangential, radial, axial)	
ρ	Density	[kg m^{-3}]
σ, σ'	Solidity, local solidity	
τ	Shear stress tensor	[Pa]
$\Omega,\ \omega$	Angular speed	[rad s^{-1}]
ζ	Vorticity	[s^{-1}]

Acronyms

2D,3D	Two or Three-Dimensional
AD, AL	Actuator Disc or Actuator Line
AOA	Angle–Of–Attack
BC	Boundary Condition
BL	Boundary Layer
BEM	Blade-Element Momentum
CFD	Computational Fluid Dynamics
DTU	Technical University of Denmark
DES	Detached Eddy Simulation
FV	Finite Volume
HAWT	Horizontal Axis Wind Turbine
LES	Large Eddy Simulation
MRF	Moving Reference Frame
NREL	National Renewable Energy Laboratory
NS	Navier–Stokes
QUICK	Quadratic Upwind Interpolation for Convective Kinetics
RANS	Reynolds-Averaged Navier-Stokes

SIMPLE	Semi-Implicit Method for Pressure Lined Equations
SA	Spalart-Allmaras
SST	Shear Stress Transport
TOE	Tonnes of Oil Equivalent
UDF	User–Defined Function (*Fluent*)
VAWT	Vertical Axis Wind Turbine
WT	Wind Turbine

List of Figures

List of Tables

Contents

Chapter 1

Introduction

1.1 The global energy scenario

The world's primary energy needs are projected to grow by 56% between 2005 and 2030, by an average annual rate of 1.8% per year (IEA World Energy Outlook[1]). Demand reaches 17.7 billion tonnes of oil equivalent, compared with 11.4 billion TOE in 2005. Fossil fuels remain the dominant source of primary energy, accounting for 84% of the overall increase in demand between 2005 and 2030. Nowadays, a large portion of the demand is satisfied by petrol technologies (about 37%) and a similar amount of production comes from coal and gas power plants (23% and 24% respectively), about 5% comes from nuclear processes and the rest is given by renewable energy sources, where hydro power is still the main contribution.

Even more strongly, Italy and many others European countries are dependent on fuel imported by foreign countries and, consequently, on the geopolitical equilibria. Furthermore, it should be noted that most of the electricity directly imported by Italy for instance comes from the nuclear power plants of France and Switzerland, just beyond the national borderlines, this even if Italy has not been using that source since 1986. In June 2002, the Italian parliament ratified the Kyoto protocol on Climate Changes, formally taking account of environmental impact of burning fossils fuels, by setting a target for the reduction of CO_2 emissions by 6.5% by 2010. Other governative directives follow in the next years, within both the national and the European Union jurisdiction, aimed to support the renewable energy development. Last, in March 2007, the European Council endorsed a binding target to satisfy 20% of the EU's energy consumption with renewable energy sources by 2020 [1]. Thus, energy policy has confirmed the improvement of the environmental sustainability of energy as a primary objective, also through increasing use of renewable sources [2].

[1] `www.iea.org`

1.2 Wind energy at the end of 2007

Two large categories of energy sources are commonly indicated: *renewable* or *fluent* and *non–renewable*. The non-renewable are the classical burning technologies that have been covering the entire energy demand till now. The only renewable energy source which had been used from the early industrial age was hydro power, while the general interest toward the other sources started growing in the 70's. In the renewable energy sector, wind power represent the most mature technology. As a consequence of an intensive research carried out in industry, the global wind energy market had been increasing with a very high rate for the past 25 years and it is nowadays economically convenient for all the possible stakeholders operating in this sector.

A comprehensive history of wind energy utilization can be found in [3] and [4]. Mankind has used wind as a source of energy for thousands of years, for ship propulsion and on earth with the first flour windmills, since nearly 600 b.C. in the Middle–East. Windmills appeared in Europe in the XII century, but the golden-age of classical windmill is indicated between the XVII and the XIX century, mainly in Northern Europe and in Greece and Iberian peninsula. Still during the rising of the industrial era, wind was one of the most utilized sources of energy together with hydro power. Between the end of the nineteenth and the beginning of the twentieth century, the first experiments were carried out on the use of windmills for generating electricity, in USA with the classical steel-bladed windmills and later in Denmark, where this technologies developed in the second post–World–War. Thereafter, there was a long period of a low interest in the use of wind power. The international oil crisis in 1973 favoured the re-utilization of renewable resources on a large scale, wind power, among others. Currently, wind power is a fully established branch on the electricity market and it is treated accordingly. Energy production is not the only criterion to be considered when installing new wind turbines; cost efficiency, the impact on the environment and in the electric grid are some of important issues of interest when making decisions about new wind turbine installations. Political support and public interest in renewable energy caused a massive increase in wind power utilization and improvement of wind turbine technology is a natural consequence.

Presently, 85,000 big wind turbines are spinning on Earth (50,000 only in Europe), with an average size of 1 MW that doubles when looking at the newest installations. In the 2005 they produced electricity for 83 TWh [1][2]. Europe is the market leader among continents (Figure 1.1), for wind power meets about 2% of the total electricity demand, i.e. more than 48,000 MW of which about 7,700 MW was installed in the last year (2006) [1]. According to the main associations of wind energy stakeholders (*e.g.* GWEC, EWEA and IEA), this development is going to continue in following years, besides wind energy is the most rapidly growing technology for renewable power generation in the world.

[2] `www.ewea.org`

In Italy the first wind turbine was installed in 1989, in Sardinia. At the end of 2006, Italy resulted the 7^{th} world's (4^{th} within EU) country for installed wind power capacity, with a total amount of 2,123 MW [5] [1], and promising wind resources exist. This confirms wind energy plays there a major role. Nevertheless, there is still a lack of attention by industry and policy toward the wind energy market. Concerning research too, the wind energy field is still regarded with interest only by few people. According to GWEC [5] in Italy "*the main barriers to the development of the wind sector remain the regional authorization hurdles (i.e. in Sardinia), the uncertainty of the legislative system, and grid connection difficulties*".

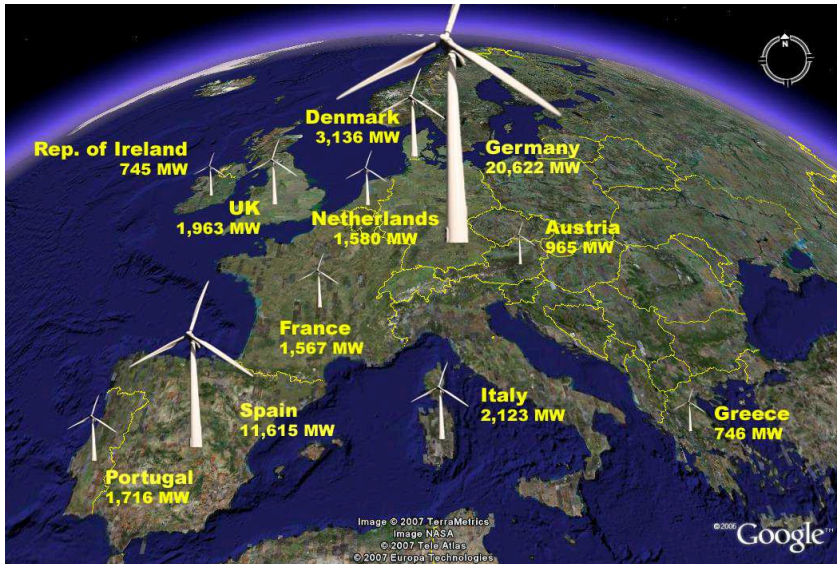

Figure 1.1: *Cumulative wind power potential in Europe by the end of 2006* (data source: EWEA, `www.ewea.org`)

1.3 Motivation and objectives

Wind energy is a low density source of power. To make wind power economically feasible, it is important to maximize the efficiency of converting wind energy into mechanical energy. Among the different aspects involved, rotor aerodynamics is a key determinant for achieving this goal. In addition, the ability to predict the downstream wake from a wind turbine is a significant factor for determining the interactions between turbines.

Research work conducted in this area has brought to a substantial improvement in the overall efficiency of the conversion process, with the result

that the capital costs of installing wind power can now compete effectively with other energy sources. Three approaches are available to analyse the flow around and downstream of a wind turbine: field or wind tunnel testing, which provides accurate results but is highly complex and expensive; analytical and semi-empirical models, which adopt simplifying assumptions and are thus not universally reliable; and CFD, which probably offers the best support or alternative to direct measurements [6].

The aim of this PhD project was to realize a comprehensive study of the *Horizontal Axis Wind Turbine* (HAWT) aerodynamics, by numerically solving the fluid dynamic problem with the help of a finite-volume Navier–Stokes CFD solver.

As a more general goal, the project was aimed at proving the capabilities of modern numerical techniques, when applying to complex fluid dynamic problems. The main purpose is hence the physics of power extraction by wind turbines. Although the significant progress in the 30-year history of modern wind energy, which has improved the efficiency of the primary process from 0.4 to nearly 0.5, many phenomena are still not fully understood [7]. Wind turbine aerodynamics involves several aspects that are unique for turbomachines:

- Wind turbines operate in the lowest part of the atmospheric boundary layer, where steady wind is an off-design condition, so that wind turbine aerodynamics is essentially unsteady.

- Unlike most of the aerodynamic devices, wind turbine does not avoid stall, but rely on it for limiting power (*e.g.* in the classical Danish-concept turbines): a thorough understanding of unsteady deep stall is hence necessary;

Moreover, the flow past a wind turbine blade is three-dimensional, particularly in the blade-tip and root region. For instance centrifugal and Coriolis forces are experienced by the boundary layer flow, mainly in the inboard, causing a stall-delay effects, by which higher lift is achieved compared to two-dimensional data.

The aerodynamic research for wind turbines has basically contributed to the fast development of modern wind energy, being the exploring techniques rather primitive just a few decades ago. Concerning the unsolved problem, mainly engineering methods have been proposed. Most of those techniques are not universally applicable, so that a better physical understanding is needed.

With this purpose, several interconnected specific issues have been faced and developed in the different phases of the project, structured as follows:

- Modelling of the middle-sized WT rotor and its flow field. Choosing the geometries and BEM-designing the blades shape;

- Flow simulation of the model, for different flow conditions and validation of the computed performances regarding to the BEM outputs;

- Design with the help of CFD: optimization of the root and tip blade;
- Wake analysis;
- Rotational effects on the boundary layer of WT blades.

Each of them is introduced together with a comprehensive literature review in the corresponding chapters.

1.4 Overview of the thesis

The functioning of modern windmills for electricity production is briefly described in Chapter 2. An overall glimpse of the classical aerodynamic models is also presented, focusing on BEM methods. The most useful definitions, found in the following through the entire thesis, are recalled.

Since the project's goals were pursued utilizing numerical tools, in Chapter 3 the computational fluid dynamics techniques are introduced. The adopted mathematical model is based on the RANS equations in a rotating reference system formulation, here rewritten together with the used turbulence models equations. Then, the commercial finite-volume solver FLUENT is shortly described, being it so often cited among the whole project. A overview of the available numerical approaches is finally given.

The results of the project are discussed in the next four chapters according to a partition into main research topics.

In Chapter 4, a validation of the computations is pursued, by means of a performance assessment and by investigating the general aerodynamic features of a middle-sized wind turbine rotor. Both a BEM-designed model and a real rotor geometry were included in the study.

In Chapter 5, CFD capabilities for the design optimization of HAWT blades are verified, analysing the effects of some modifications at the blade tip and root regions.

In Chapter 6 a general study of wind turbine wakes is reported.

Finally, Chapter 7 deals with the basics of rotating blades issues. Hereby, it concerns the investigation of the rotational effects on the boundary layer, which was partially developed during a visiting stay at the Technical University of Denmark (DTU).

The concluding remarks are summarized in Chapter 8, as well as future work suggestions.

Chapter 2

Wind Turbine functioning and aerodynamics

This thesis deals uniquely with *Horizontal Axis* Wind Turbines (HAWT). When compared to the *Vertical Axis* Wind Turbines (VAWT), the HAWTs

- present higher values of power coefficients
- operate in the high Atmospheric Boundary Layer instead of the bottom shear layer, so they see more uniform and intense wind speeds
- have a more stable mechanical behaviour and they can assume larger sizes

Although they were widely investigated in the 1980's, VAWTs have not proved to be commercially competitive and are not currently manufactured in significant number [8]. Additional information about VAWTs characteristics can be found in [3].

2.1 Wind power technology

Nowadays, wind turbines are the largest rotating machines on earth. The world's largest passengers airliner, *i.e.* the Airbus A-380, has a wing span of about 80 m, whereas a Enercon E-126/6 MW wind turbine (the world's most powerful WT) has a rotor diameter of 126 m which, being the tower even 138 m tall, makes this machine reach 200 m of overall height from tower base to blade tip[1]. They are also the oldest devices for exploring the energy of the wind on land. In fact, the only older device for utilizing wind energy in general is the sailing ship [7][9].

Mankind has needed for centuries mechanical energy, mainly for agriculture, and increasingly. In order to extract a useful form of energy from wind, that

[1] `www.enercon.de`

he saw free flowing everywhere, proper machines were necessary and here is how windmills born. Today after decades of running industrial development, modern turbines transform the same energy to electric power, that has already become no replaceable for human life in the XXI century. Moreover, the huge and still increasing size causes their design to be a real challenge for engineers.

The knowledge about the wind power technology has increased over the years (for a review of early wind turbine development see for instance [3]). The development of various windmill types from Middle-Ages to the industrial era can hardly be considered the result of a systematic research and development. However, as late as the XVII and XVIII century, when physical–mathematical thinking became more established, systematic considerations on windmill technology took their beginnings. Among the other, Leonardo, Leibniz, Bernoulli and Euler involved themselves in the matter. In about 1890 the Danish professor Poul La Cour carried out extensive scientific research in windmill blade aerodynamics and windmill design, turning later his experiments to how to generate electrical current with the help of wind power. Like no other he marked the turning point from historical windmill building to the modern technology of power generating wind turbines. Lanchester (1915) and Betz (1920) were the firsts to predict the maximum power output of an ideal wind turbine, by applying the principle that for the extraction of mechanical energy from an air flow the exact geometry of the energy converter is physically irrelevant [6]. A similar approach had already been developed by Froude and Rankine at the end of the XIX century, but for ship propellers. Nevertheless, the major break-through was achieved by Glauert who formulated the Blade Element Momentum (BEM) method in 1935, which will be discussed in Section 2.3.

2.2 Functioning of HAWT

In this section the basics of the functioning of modern HAWT are briefly summarized. Since the transformation of wind energy into electricity is not obtained directly, but consists of many complicated steps (and passing through the mechanical energy form). The latest technologies of aerodynamics, mechanics, control systems and electro technology are involved in such process.

Wind turbine blades are affected by a force distribution, which results in a mechanical torque at the rotor shaft and the rotor itself rotates. In modern airscrew that aerodynamic driving force is mainly a lift force, like for the aircraft flight, rather than drag force like it is in ancient sailing ships. The shaft transfers the torque from the blades to the generator, but this passage can be achieved in different ways. The most commonly applied wind turbine set-ups are three [9]:

- A classical turbine with gearbox, *i.e.* the so-called *Danish concept*. A gearbox with typically 3 steps connects the rotor shaft (the *slow* one) to the generator shaft (the *fast* one), which is directly joint to the electrical grid and therefore has a fixed rotational speed. Usually, in the old types,

those configurations do not present an active aerodynamic control, but blades are stall-regulated while wind changes.

- A turbine without gearbox, with the axle directly connected to the generator. It is a newer concept, where a large multi-pole generator allows the unique shaft to rotate with the low speed of the rotor.

- A hybrid concept, which combines the previous two. It is given by adopting a smaller generator and a smaller (usually 1-step) gearbox for matching the request angular speed.

With regards to the rotor-generator-grid coupling four concepts can be distinguished [10]:

- Type A - *fixed speed wind turbine concepts.*
  It corresponds to the "Danish concept", there is hence a squirrel cage induction generator (SCIG) directly connected to the grid through a transformer

- Type B - *variable speed wind turbine concept with variable rotor resistance.*
  Here is a Optisplip induction generator, where the rotor winding of the generator is connected with an optically (no need of slip-rings) controlled resistance. By changing the resistance the slip changes and thus the power output can variate in a range of 0-10 % of the synchronous speed.

- Type C - *variable speed wind turbine concept with partial-scale power converter.*
  This configuration denotes the variable speed controlled wind turbine with doubly fed induction generator (DFIG) and pitch control. The stator is directly connected to the grid, while the rotor is connected through a partial-scale power converter. The variable speed range is +/- 30% around the synchronous speed.

- Type D - *variable speed wind turbine concept with full-scale power conver*ter.
  This configuration corresponds to the full variable speed, pitch-controlled wind turbine with the generator connected to the grid through a full-scale power converter. The generator can be excited electrically (WRSG or WRIG), permanent magnet excited type (PMSG) or squirrel cage induction generator (SCIG). Typically, a direct driven, multi-pole synchronous generator (no gearbox) is used. This concept has full control of the speed range from 0 to 100% of the synchronous speed. However, it has a higher power loss in the power electronics compared to Type C concept, since all the generated power has to pass through the power converter.

Thus, it is clear that the aerodynamic control and regulation systems allow the turbine to follow the variable wind. All modern turbines have variable pitch

and variable angular velocity. As wind intensity increases the pitch changes to follow the best aerodynamic flow angles along the blades and angular speed increases for absorbing the torque exceeding the power train capacity. The turbine must also yaw into the wind. Thus, on top of the nacelle an anemometer together with a wind vane determine intensity and direction of the incoming wind. The output signal commands the electric motors located inside a cog ring at the top of the mast.

The start-up wind velocity (*cut-in*) of a wind turbine is about 3–5 m/s. While the wind speed increases the power production growths too, till the rated power is reached and then the exceeding output is limited. At a fixed value of wind speed (*cut-off*), typically around 25 m/s the turbine stops for safety reasons (*standstill*). For the correct functioning of a wind turbine control systems are therefore needed. Until rated power is reached, those systems should make the turbine work with the maximum efficiency, whereas after the peak the target is keeping the power constant. We can gather the various control systems into three families (see *e.g.* [4][9] and [10]):

- *Stall control*
  It is a passive way of controlling the power output of a wind turbine, so that is rather used in old machines. The blades are aerodynamically shaped in order to work with optimum angle of attack at the average wind speeds, whereas at higher speed the flow angle increases, separation occurs on their sections and that is how lift force is limited. As wind keeps increasing, then the lift force of the blades also decreases because of increasing stall. The exceeding loads are in such way completely dissipated and no possible control on the efficiency could be done in the low-speed operating range. None rotational speed control is here available. Small and economical turbine types adopt this regulation, as well as the elder models.

- *Pitch control*
  The blades can be pitched, *i.e.* turned around their axes by means of hydrodynamic or electrical motors. In such way they follow the optimum angles till the rated power speed is reached and then the loads are limited by loosing lift forces.

- *Active stall*
  Active stall control triggers stall intentionally. Once in stall, only very small pitch excursions are required to give shorter response times than these of pitch control. However, stall is an unstable operating condition and allows thrust remaining large.

Wind turbines must be provided by proper brake systems that are used for emergency stops and when maintenance is needed. Usually, wind turbines are equipped with both an aerodynamic and a mechanical brake. The design of the aerodynamic brake depends on the control system. *I.e.* if the blade is

stall regulated only the tip turns to decelerate the rotor, otherwise the whole blade can pitch and faces the wind in standstill operation. The aerodynamic brake activates first. When rotor has already decelerated, a mechanical brake system, which consists of a disk brake, activates too. If an emergency occurs, both brake systems are activated at the same time. Both brake systems are usually active, *i.e.* a force is acting to deactivate them during normal operation. Therefore, if something goes wrong, for example a power failure, the brakes activate automatically without any applied force or control system.

The largest turbine built today has a generator of about 6MW. In a promising wind site (2000 hours/year of nominal equivalent functioning) a turbine of that size will produce about 12 GWh of electrical energy per year. This is sufficient to provide the energy for more than 2,000 houses. But the average operational life of such machine is 20 years and the actual operational time about 120,000 hours at all. When comparing to a car that run for 300,000 km in its life at an average speed 60 km/h, *i.e.* for 5,000 hours only, we realize how accurate should be the design of a wind turbine.

In the following a few numbers and significant traits of a wind turbine are summarized:

- Number of blades: 1, 2, 3, 4... typically 3!
- Rotational speed: 20-50 RPM
- Tip-speed (ωR): less than 70 m/s for noise limitation
- Rated power: from 1 kW (*Micro-turbine*) to 6 MW (*Multi–MW* WT)
- Control system: stall-regulation, active-pitch, variable speed (rotational)
- Tower-height/Rotor-diameter ratio: H/D

The large increasing penetration of large wind turbines into electrical power systems is inspiring continuously the designers to develop both custom generators and power electronics, and to implement modern control system strategies. Wind turbine design objectives have thus changed over the years from being conventional-driven to being optimized-driven, within the operating regime and market environment. In addition to becoming larger, wind turbine design concepts have been progressing from fixed speed, stall-controlled and drive trains with gearbox to variable speed, pitch-controlled with or without gearbox.

2.3 A brief review of the aerodynamic models

The size of commercial wind turbines has increased dramatically in the last 25 years, from approximately a rated power of 50kW and a rotor diameter of 10-15 m up to today's commercially available 5-6 MW machines with a rotor diameter of more than 120 m (Figure 2.1).

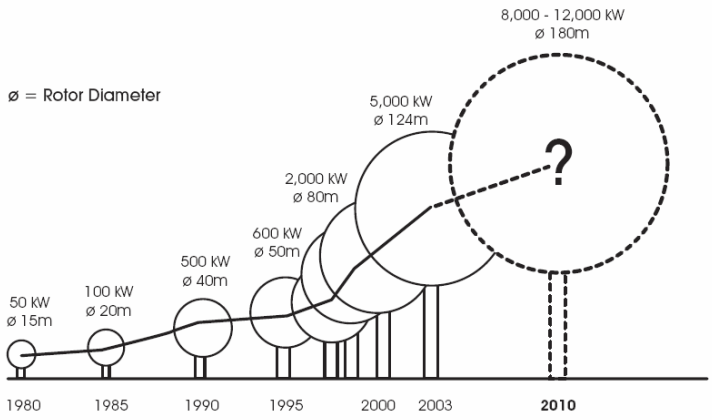

Figure 2.1: *Growth in the size of commercial wind turbines* (source: EWEA, `www.ewea.org`)

This development has forced the design tools to change, from simple static calculations assuming a constant wind to dynamic simulation software that, from the unsteady aerodynamic loads, model the aeroelastic response of the entire wind turbine construction (including tower, drive train, rotor and control system) [11].

Here, the basic theory for different classical aerodynamic models is treated. The following models will be reviewed:

- Blade Element Momentum method
- Lifting line, panel and vortex methods
- Actuator disc method
- Navier-Stokes solvers

Prior, some basic definition is introduced.

2.3.1 Basic definitions

Tip speed ratio

The tip speed ratio is a very important parameter for wind turbine design. It expresses the ratio between the tip speed and the undisturbed wind speed.

$$\lambda = \frac{\Omega R}{U_\infty} \tag{2.1}$$

where Ω is the angular velocity, R the radius of the blades and U_∞ the undisturbed wind speed. The tip speed ratio dictates the operating condition of a turbine and it affects a number of flow parameters that will be discussed later. Typical values for modern turbines are $6 \div 8$. It is commonly used a *local* tip speed ratio too, that for a certain radius r writes the same, but with r instead of R.

Solidity

The turbine solidity is defined as the ratio between the blade area to the area of the disk

$$\sigma = \frac{Total\ blade\ area}{Disc\ area} \tag{2.2}$$

and likewise a *local* turbine solidity is defined, while referring to a certain radius r, as follows

$$\sigma = \frac{Bc(r)}{2\pi r} \tag{2.3}$$

where B is the number of blades and c the chord length of the local blade section.

Power coefficient

The kinetic energy of an air mass m moving at a freestream velocity U can be expressed as

$$E = \frac{1}{2}mU^2 \tag{2.4}$$

and for unit mass is

$$e = \frac{1}{2}U^2 \tag{2.5}$$

Taking a certain cross–section area A, by which the air passes at the velocity U, the volume V flowing through during a certain time unit, the so–called volume flow Q is

$$Q = UA \tag{2.6}$$

and the mass flow with the air density ρ is

$$\dot{m} = \rho Q = \rho UA \tag{2.7}$$

With the product of the kinetic energy of the moving air and the mass flow, one yields the amount of energy passing through a cross–section A per second. This is physically a power P

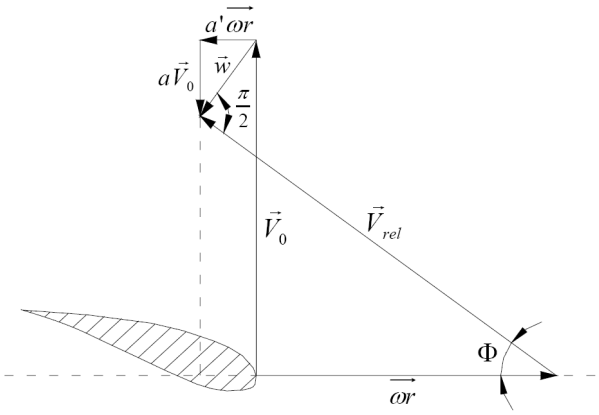

Figure 2.2: *Induction factors*

$$P_0 = \dot{m}e = \frac{1}{2}\rho U^3 A \tag{2.8}$$

This is the available power in the wind. However, if we had taken the whole energy, the flow would be arrested. Thus there should be a *power coefficient* C_P that determines the portion of the flow energy captured by the generic wind energy converter

$$P = C_P P_0 \Longrightarrow C_P = \frac{P}{\frac{1}{2}\rho U_\infty^3 A} \tag{2.9}$$

according with Betz, C_P can never exceed a value of $C_{P,max} = 16/27$ (the *Betz limit*, see *e.g.* [3] or [8]).

Thrust coefficient

In a similar way a *thrust* coefficient could be defined for the integral thrust force acting on the rotor T

$$C_T = \frac{T}{\frac{1}{2}\rho U_\infty^2 A} \tag{2.10}$$

Induction factors

The incoming wind flow is affected by the turbine blade as it approaches the rotor [12]. The effective apparent velocity seen by the blade vortex system is modified as illustrated in Figure 2.2.

By decomposing into its axial or *streamwise* and tangential component the velocity vector and introducing the induction factors a and a' we get these relationships

$$U_a = (1 - a)U_\infty \tag{2.11}$$

$$U_t = (1 + a')\omega r \tag{2.12}$$

The above mentioned properties deal with the entire wind turbine rotor. On the other hand, it is necessary to invoke some of the characteristics of the *airfoils* that one finds while sectioning the blades. This belongs to 2D aerodynamics, as for a cylindrical wing of infinite span. For even though the real wing of a modern wind turbine is not infinite and presents a 3D aerodynamic behaviour, the theory of wind section remains of practical interest. The BEM method is based on 2D aerodynamics, and Prandtl has shown that local 2D data can be used if the angle of attack is corrected accordingly with the trailing vortices behind the wing or blade.

Lift and drag coefficients

Lift L is defined as the force acting on the airfoil in a direction normal to the free stream direction. *Drag* D as the force along the free stream direction. Lift will only be present if the flow incorporates a circulatory flow about the body. The velocity above the body is increased, and so the static pressure there is reduced. Conversely, the velocity beneath is slowed down, giving an increase in static pressure. There is clearly a normal force upwards on the airfoil, a lift force. The phenomenon of lift was described by *Kutta* and *Joukowski* (see *e.g.* [8])

$$L = \rho U_\infty \times \Gamma \tag{2.13}$$

where Γ is the *circulation*, or *vortex strength*, around the airfoil, defined as the integral

$$\Gamma = \int u ds \tag{2.14}$$

around any path enclosing the airfoil, and u is the velocity tangential to the path s.

Lift and drag *coefficients* define the characteristic of an airfoil

$$C_l = \frac{L}{0.5\,\rho\,U^2\,c} \tag{2.15}$$

$$C_d = \frac{D}{0.5\,\rho\,U^2\,c} \tag{2.16}$$

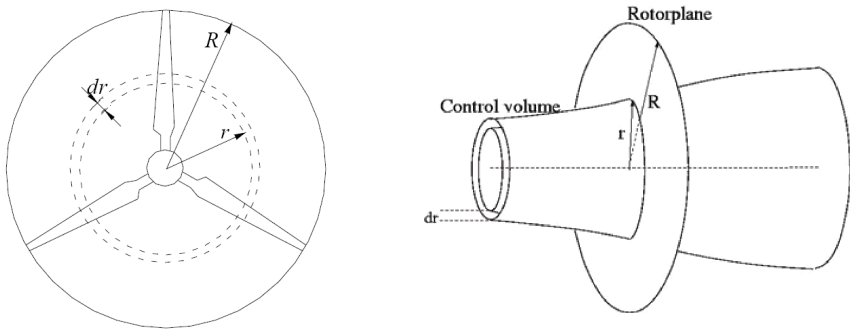

Figure 2.3: *BEM annular control volumes*

being L, D forces per unit span, U the flow speed and c the chord length. These coefficients are function of the angle of attack, Reynolds number and Mach number.

Pressure coefficient

Dealing with airfoils, pressure coefficient is often defined as follows

$$C_p = -\frac{p - p_\infty}{\frac{1}{2}\rho U^2} \tag{2.17}$$

This is inverse to the general definition, in order to have the positive the *suction*, which is the main contribution to lift generation.

2.3.2 The BEM method

Loads and performance calculations of wind turbines are today routinely performed by the Blade-Element Momentum method [6]. The method is indeed computationally cheap and thus very fast, even with providing very satisfactory results [2].

The BEM method consists on dividing the flow in annular control volumes and applying momentum balance and energy conservation in each control volume. The annuli are bounded by stream surfaces that enclose the rotor and extend from far upstream to far downstream (Figure 2.3).

Basic assumptions of the method are that the induced velocity in the rotor plane is equal to one half of the induced velocity in the ultimate wake, and that the flow can be analysed by dividing the blade into a number of independent elements. Moreover the loads for each blade are uniformly distributed

[2]For a comprehensive description of BEM see for instance [3] or [13]

azimuth-wise, which means the rotor would have an infinite number of blades. For each blade element, the aerodynamic forces are obtained using tabulated airfoil data, which stem from wind tunnel measurements and corrected for three-dimensional effects. The BEM could be a *design* as well as a *verification* method. When using BEM as a design method, the following inputs and outputs are defined:

- INPUT:
  Rated power P, power coefficient C_P, mean wind speed V_0, number of blades B
- OUTPUT:
  Rotor diameter D, chord $c_i(r)$ and twist $\theta_i(r)$ radial distribution

This is in principle the BEM method, but in order to get good results it is necessary to apply , at least, the two corrections below.

- The first is called *Prandtl's tip loss factor*, which corrects the assumption of an infinite number of blades.
- The second correction is called *Glauert's correction* and is an empirical relation between the thrust coefficient C_T and the axial interference factor a for values of a greater than approximately 0.3, where the relation derived from the one-dimensional momentum theory is no longer valid.

Since the BEM model is simple and very fast to run on a computer, it has gained an enormous popularity and is today the only design code in use by industry. However, owing to limitations of representing all the various flow situations encountered in practice, it has become necessary to introduce different empirical corrections. Such situations include phenomena related to dynamic inflow, yaw misalignment, tip loss and heavily loaded rotors. There exists thus an increasing need to establish experiments and to develop more advanced models to evaluate the basic assumptions underlying the BEM model. Although today there seems to be no realistic alternative that may replace the BEM model as an industrial design tool, a number of more advanced inviscid models have been developed to overcome the limitations of the momentum approach.

2.3.3 Lifting line, panel and vortex methods

3D inviscid aerodynamic models have been developed in an attempt to obtain a more detailed description of the 3D flow that develops around a wind turbine. The fact that viscous effects are neglected is certainly restrictive as regards the usage of such models on wind turbines. However, they should be given the credit of contributing to a better understanding of dynamic inflow effects as well as providing a better insight into the overall flow development. There have been attempts to introduce viscous effects using viscous–inviscid interaction techniques [14] but according with Hansen *et al.* [11] they have not

yet reached the required maturity so as to become engineering tools, although they are full 3D models that can be used in aeroelastic analyses.

In vortex models, the rotor blades, trailing and shed vorticity in the wake are represented by *lifting lines* or *surfaces*. The vortex strength on the blades is determined from the bound circulation that stems from the amount of lift created locally by the flow past the blades. The trailing wake is generated by the spanwise variation of the bound circulation, while the shed wake is generated by a temporal variation, and ensures that the total circulation over each section along the blade remains constant in time. Knowing the strength and position of the vortices, the induced velocity $w(x)$ can be found in any point using the Biot-Savart induction law

$$w(x) = -\frac{1}{4\pi}\int \frac{(x-x')\times\omega'}{|x-x'|^3}dV \tag{2.18}$$

with ω the vorticity, x the point where the potential is computed and x' the point of integration, which is taken over the region where the vorticity is non-zero. In the *lifting lines* models, the bound circulation is found from airfoil data table-look up, just as in the BEM method. The inflow is determined as the sum of the induced velocity, the blade velocity, and the undisturbed wind velocity.

The relationship between the bound circulation and the lift is the well-known Kutta-Joukowski theorem, and using this together with the definition of the lift coefficient, a simple relationship between the bound circulation and the lift coefficient can be derived

$$L = \rho\, U_{rel}\, \Gamma = \frac{1}{2}\rho\, U_{rel}^2\, c\, C_L \Longrightarrow \Gamma = \frac{1}{2}\, U_{rel}\, c\, C_L \tag{2.19}$$

In its simplest form the wake from one blade is prescribed as a hub vortex plus a spiralling tip vortex, or as a series of ring vortices. Actually, one of the most recurrent application of vortex methods has been wake dynamics.

The inviscid and incompressible flow past the blades can be found by applying a surface distribution of *sources* and *dipoles*. This is the approach followed by *panel methods*. The background is Green's theorem which allows obtaining an integral representation of any potential flow field in terms of singularity distribution. An external potential flow field is given, possible varying in time and space, to which is added a perturbation scalar potential. The active boundary of the flow includes both the solid boundaries as well as the wake surfaces. Dipoles are added so as to develop circulation into the flow to simulate lift.

2.3.4 Actuator disc methods

The actuator disc model is probably the oldest analytical tool for evaluating rotor performance. In this model, the rotor is represented by a permeable disc that allows the flow to pass through the rotor, at the same time as it is subject to the influence of the surface forces. The classical actuator disc model is based

on conservation of mass, momentum and energy, and constitutes the main ingredient in the 1D momentum theory, as originally formulated by Rankine and Froude. Combining it with a blade-element analysis, we end up with the classical Blade-Element Momentum Technique by Glauert. In its general form, however, the actuator disc might as well be combined with the Euler or NS equations. Thus, as will be told in the following, no physical restrictions have to be imposed on the kinematics of the flow. In a numerical actuator disc model, the NS (or Euler) equations are typically solved by a second order accurate finite difference/volume scheme, as in a usual CFD computation. However, the geometry of the blades and the viscous flow around the blades are not resolved. Instead, the swept surface of the rotor is replaced by surface forces that act upon the incoming flow. The main limitation of the axisymmetric assumption is that the forces are distributed evenly along the actuator disc, hence the influence of the blades is taken as an integrated quantity in the azimuthal direction. To overcome this limitation, an extended 3D actuator disc model has recently been developed [6]. The model combines a 3D NS solver with a technique in which body forces are distributed radially along each of the rotor blades. Thus, the kinematics of the wake is determined by a full 3D NS simulation, whereas the influence of the rotating blades on the flow field is included using tabulated airfoil data to represent the loading on each blade. As in the axisymmetric model, airfoil data and subsequent loading are determined iteratively by computing local angles of attack from the movement of the blades and the local flow field. The concept enables one to study in detail the dynamics of the wake and the tip vortices and their influence on the induced velocities in the rotor plane.

A main motivation for developing such types of model is to be able to analyse and verify the validity of the basic assumptions that are employed in the simpler and more practical engineering models. Reviews of the basic modelling of actuator disc and actuator line models can be found in [9]and [15], that also includes various examples of computations.

2.3.5 Navier-Stokes solvers

The first applications of CFD to wings and rotor configurations were studied back in the late seventies and early eighties, in connection with aircraft wings and helicopter rotors, using potential flow solvers. A shift towards unsteady Euler solvers was seen through the 80's.

Full-RANS equations were solved first for helicopter rotor computations, including viscous effects, in the late eighties and early nineties, but the first full NS computations of rotor aerodynamics were reported in the literature in the late nineties (see *e.g.* [13]).

Recently, DES and LES techniques, which are becoming increasingly important in several engineering fields, have been directed at solving turbines flow (see *e.g.* [16][17][18]), even if their high computational efforts still remain a drawback for a practical usage.

Nowadays, an extensive literature of N–S CFD studies on wind turbine exist (see Section 4.1). Since this way has been chosen for the study of WT aerodynamics, a more comprehensive description of the CFD methodologies is presented in the Chapter 3.

Chapter 3

CFD and Wind Turbines

3.1 Introducing CFD

With Computational Fluid Dynamics we indicate the numerical solution of the differential governing equations of fluid flows, with the help of computers. This technique has a wide range of engineering applications. In the field of aerodynamic research this technique has become increasingly important and it is prominent for studying turbomachinery.

A number of valuable advantages are achieved following a CFD approach to a fluid dynamic problem:

- CFD is faster and definitely cheaper. A considerable reduction of time and costs for solving the problems is offered compared to the traditional approaches. A conscious assessment of different solutions is available in the early phase of the design process, in order to fit with the requested tasks. Thus, experimental tests would be done just on few models, resulted from the CFD analysis.
- Full-size analysis is hard to perform for large systems, like modern wind turbines are, or for extreme thermo-flow conditions as well as narrow geometries. A CFD study is a favourable choice in these cases.
- A key–important quality of CFD are the detailed solutions allowed by the recent techniques (and computer technologies), even for time-dependent flows and complex systems.
- The numerical models of the physical problems have good accuracy and reliability, due again to the newest mathematical improvements of solution schemes and of turbulence models.
- Due to the last two advances, in most of the cases the prediction of a fluid dynamic problem does not require a dedicated powerful workstation and sometimes a personal computer might be sufficient.

The numerical modelling of a fluid dynamics problem implicates first a precise reading of the physical phenomena. All the relevant features of interest should be indicated at that first step, including geometry, materials, boundary conditions, to be defined in the simplest way, but without introducing extreme errors with the hypothesis. Nevertheless, a number of simplifications is always accepted, and is inevitable in order to model properly fluid dynamics problems.

3.2 The structure of a CFD code

A comprehensive overviews of the techniques used to solve problems in fluid mechanics on computers is given in [19][20][21]. In commercial codes a friendly interface gives the user the possibility of easy setting the various options and analyze the results. Three large parts are generally indicated of a CFD code, which correspond to three phases of the problem analysis:

- *Preprocessor*
  In this phase the physical problem is implemented into the mathematical model. The computational domain is now defined. Then, it is divided into a certain number of elements, which constitute the *mesh* or *grid*. The fluid properties and the boundary conditions are set. Since the CFD solution of a fluid dynamic problem is given locally, for well–defined positions within computational grid, the global accuracy strongly depends on the total number of mesh elements. A rule–of–thumb says the larger is the number of elements, the better is the solution accuracy, even though CPU effort and the total time of convergence will be higher as well. Consequently, the optimal grid should not be uniform, but finer where higher are the variables gradients and coarser in the region characterized by smooth changes in the flow. The final success of a CFD simulation strongly depends on the preprocessing and therefore a special attention might be paid to the choice of the mesh and of boundary conditions.

- *Solver*
  The numerical solution algorithm is the core of a CFD code. All the main CFD solvers work with the following procedure:

  - *Modelling* the problem unknowns by means of simple analytical functions.
  - *Discretising* the governing equations for the fluid flows, properly modified by substituting the former mentioned functions.
  - *Solving* the algebraic system of equations.

  Most of the commercial CFD codes (*e.g.* FLUENT) are based on a **finite volume** discretization and perform these operations:

  - *Integrating* the governing equations over each control volume within the computational domain. In the resulting equations, the flux terms figure.
  - *Discretising*: the flux terms, which deal with convection and diffusion processes, are approximated with a finite differential approach as well as the source terms when being present, in order to obtain an algebraic system of equations.
  - *Solving* the algebraic system of equations with iterative methods.

  The integration phase distinguishes between FV methods and other numerical techniques. By integrating the governing equations, a new set of equations even now *exact* is obtained, which states the conservation of the fundamental properties for each of the cells (finite control volumes) within the computational domain. The characteristic that makes preferable the finite volume approach, with regard to thermo-fluid dynamics problems, is the principle of conservativeness [20].

- *Post-processing*
  Under this definition we include the analysis of solution results. The solver output is a set of solution variables, associated to the given grid nodes or volumes. These data must be collected, elaborated in the most suitable way for the analysis, in order to produce a physical representation of the solution. Some CFD software package (like Fluent for instance) contains a post-processing section. Other solvers need an external tool for data treatment, which can be a commercial one (several complete packages exist for the scope) or a dedicated in–house code. Anyhow, one might be able to do the following post-processing operations :

  - Domain and grid visualization
  - Vectorial plots of solution variables
  - Linear, surface, volume integrals
  - Iso-level and contour plots of solution variables, within selected domain zones
  - Drawing two-dimensional and three-dimensional plots
  - Tracking path-lines, stream traces, etc.
  - Algebraic and analytical operations within the variables
  - Dynamic representations, animations etc.

  In general, we should refer to the solved flow field as it had been an experimental test situation. Among the given data set, we could operate as we were using real instruments, by selecting the position of “virtual” probes or control surfaces where our interest is focused.

3.3 RANS equations

When approaching the study of fluid dynamics problems, the mathematical model is based on the fundamental mass, momentum and energy conservation principles. Therefore, the conservation laws are invoked in the following, in the vectorial notation and conservative form for unsteady, three–dimensional compressible flow.

The equations for *conservation of mass*, or *continuity equation*, can be written as follows

$$\frac{\partial \rho}{\partial t} + \nabla \cdot (\rho \vec{v}) = S_m \tag{3.1}$$

where S_m is a mass source. The *conservation of momentum* is [22]

$$\frac{\partial}{\partial t}(\rho \vec{v}) + \nabla \cdot (\rho \vec{v} \vec{v}) = -\nabla p + \nabla \cdot \left(\overline{\overline{\tau}}\right) + \rho \vec{g} + \vec{F} \tag{3.2}$$

where p is the static pressure, $\overline{\overline{\tau}}$ is the stress tensor (described below), $\rho \vec{g}$ is the gravity force and $\vec{F}$ are the other external body forces. By assuming the Stokes' hypothesis for newtonian fluids, the stress tensor $\overline{\overline{\tau}}$ is given by

$$\overline{\overline{\tau}} = \mu \left[(\nabla \vec{v} + \nabla \vec{v}^{\,\mathrm{T}}) - \frac{2}{3} \nabla \cdot \vec{v} I \right] \tag{3.3}$$

These above are named as *Navier-Stokes equations*.

According to Reynolds, for each of the instantaneous dependent variables in the NS equations a time–average and a randomly fluctuating component can be found, for instance the velocity i-component will be

$$u_i = \overline{u_i} + u_i' \tag{3.4}$$

where $\overline{u_i}$ is the time–averaged component and u_i' the fluctuating one. The time-averaged term is obtained by means of the Reynolds' time-average operator, which locally applied to the velocity vector reads

$$\overline{u_i} = \frac{1}{\Delta t} \int_{t_0}^{t_0 + \Delta t} u_i dt \tag{3.5}$$

After applying the previous expression to the whole variable set in the NS equations, the incompressible *time-averaged* NS or incompressible *RANS equations* results. For compressible flows an analogous set of equation results by applying in addition a mass-averaging operator.

3.4 Turbulent modelling

Concerning the study of viscous flows, a laminar regime exists only at low *Reynolds number*

$$Re = \frac{\rho U L}{\mu} \tag{3.6}$$

where L is a characteristic length scale (*e.g.* the chord length for airfoil sections), U the undisturbed stream velocity and μ the dynamic viscosity. The Reynolds number represents the *inertial* (*i.e.* convective) to *viscous* forces ratio. Indeed, when the Reynolds number growths, the flow field structures change and time-fluctuating velocity and pressure components appear, even though boundary conditions are still steady in a time-averaged sense.

When the flow regime becomes turbulent, the fluid motion looks disorganized and single particles follow a winding path. This being even if the mean are well-established paths, which is properly defined as *main stream flow*. A turbulent flow has often high level vorticity, which means also that *diffusion* phenomena come out for all the physical properties of the flow, both vector (*e.g.* momentum) and scalar *(e.g.* temperature).

For the prediction of wind turbine aerodynamics, the Spalart-Allmaras and k–ω SST turbulence models have been chosen. Both of them can be repeatedly found in the literature, and the second furthermore is generally retained as the most proper solution for this specific issue (see *e.g.* [7][11][23]).

Spalart-Allmaras

The Spalart-Allmaras model is a relatively simple one-equation model that solves a modelled transport equation for the kinematic eddy (or *turbulent*) viscosity. This embodies a relatively new class of one-equation models, in which it is not necessary to calculate a length scale related to the local shear layer thickness. The Spalart-Allmaras model was designed specifically for aerospace applications, involving wall-bounded flows, and has been shown to give good results for boundary layers subjected to adverse pressure gradients. Moreover, it has also shown fairly good capabilities for turbomachinery applications.

In its original form, the Spalart-Allmaras model is effectively a low-Reynolds number model, requiring the viscous-affected region of the boundary layer to be properly resolved. In FLUENT, however, the S-A model has been implemented to use wall functions when the mesh resolution is not sufficiently fine. This might make it the best choice for relatively crude simulations on coarse meshes where accurate turbulent flow computations are not critical. On a cautionary note, however, one-equation models are often criticized for their inability to rapidly accommodate changes in length scale, such as might be necessary when the flow changes abruptly from a wall-bounded to a free shear flow.

The transported variable in the Spalart-Allmaras model $\tilde{\nu}$, is identical to the turbulent kinematic viscosity except in the near-wall (viscous-affected) region.

The transport equation for $\tilde{\nu}$ is [24]

$$\frac{\partial}{\partial t}(\rho\tilde{\nu})+\frac{\partial}{\partial x_i}(\rho\tilde{\nu}u_i) = G_\nu+\frac{1}{\sigma_{\tilde{\nu}}}\left[\frac{\partial}{\partial x_j}\left\{(\mu+\rho\tilde{\nu})\frac{\partial\tilde{\nu}}{\partial x_j}\right\}+C_{b2}\rho\left(\frac{\partial\tilde{\nu}}{\partial x_j}\right)^2\right]-Y_\nu+S_{\tilde{\nu}} \tag{3.7}$$

where G_ν is the production of turbulent viscosity and Y_ν is the destruction of turbulent viscosity that occurs in the near-wall region due to wall blocking and viscous damping. $\sigma_{\tilde{\nu}}$ and C_{b2} are constants and ν is the molecular kinematic viscosity. $S_{\tilde{\nu}}$ is a source term. The equation and its coefficients were calibrated from turbulent flows around airfoils. This is the reason why the S-A model is very effective for attached aerodynamic flows. Nevertheless, the model gives unacceptable results when conditions depart too greatly from what the model is calibrated for, such as separation generated by large angle of attack in airfoils flow.

k–ω SST

In the k–ω turbulence models the transport equation of the turbulent kinetic energy is solved together with the equation of the specific rate of dissipation of turbulent kinetic energy, defined as $\omega = \epsilon/k$. This model performs well with free shear flows, flat plate boundary layer flows, complicated adverse pressure gradient flows and separated flows. A problem of the standard k–ω model is the dependency on the free stream boundary conditions. The shear-stress transport (SST) k–ω model was developed by Menter to effectively blend the robust and accurate formulation of the k–ω model in the near-wall region with the free-stream independence of the k–ϵ model in the far field. The SST k–ω model is similar to the standard k–ω model, but includes a number of features that make the SST k–ω model more accurate and reliable for a wider class of flows (*e.g.*, adverse pressure gradient flows, airfoils, transonic shock waves) than the standard k–ω model. The SST k–ω model equations read [24]

$$\frac{\partial}{\partial t}(\rho k)+\frac{\partial}{\partial x_i}(\rho k u_i) = \frac{\partial}{\partial x_j}\left(\Gamma_k\frac{\partial k}{\partial x_j}\right)+\tilde{G}_k-Y_k+S_k \tag{3.8}$$

$$\frac{\partial}{\partial t}(\rho\omega)+\frac{\partial}{\partial x_i}(\rho\omega u_i) = \frac{\partial}{\partial x_j}\left(\Gamma_\omega\frac{\partial\omega}{\partial x_j}\right)+G_\omega-Y_\omega+D_\omega+S_\omega \tag{3.9}$$

3.5 The software FLUENT

Finite-Volume approach

The commercial code Fluent solve the governing integral equations for the conservation of mass and momentum, and (when appropriate) for energy and other scalars, such as turbulence and chemical species [24]. In both cases a control-volume-based technique is used [20][21], which consists of:

- Division of the domain into discrete control volumes using a computational grid.
- Integration of the governing equations on the individual control volumes to construct algebraic equations for the discrete dependent variables (*unknowns*), such as velocities, pressure, temperature, and conserved scalars.
- Linearisation of the discretised equations and solution of the resultant linear equation system, to yield updated values of the dependent variables.

Fluent is a commercial 2D/3D unstructured mesh solver, which adopts multigrid solution algorithms. It uses a co-located grid, meaning that all flow parameters are stored in the cell-centres. It is written in C-language, which allows users to introduce a number of model modification through UDFs. Processes can be easily parallelised on multiple computer nodes.

Two numerical methods are available in Fluent:

- *Pressure-based* solver
- *Density-based* solver

The first one was developed for low-speed incompressible flows, whereas the second was created for the high-speed compressible flows solution. Although they have been recently modified in order to operate for a wider range of flow conditions, in the present study, which involves incompressible flows, the pressure-based approach was preferred.

The pressure-based solver

In the pressure-based approach the pressure field is obtained by solving a pressure correction equation, which results from combining continuity and momentum equation. *I.e.* the pressure equation is derived in such a way that the velocity field, corrected by the pressure, satisfies the continuity. The governing equations are non-linear and coupled one another. The solution process involves therefore iterations, wherein the entire set of governing equations is solved repeatedly, until the solution converges.

Two types of solution algorithms are available in Fluent:

- Segregated
- Coupled

The segregated pressure-based solver uses a solution algorithm where the governing equations are solved sequentially (*i.e. segregated*) from one another. The segregated algorithm is memory-efficient, since the discretised equations need only be stored in the memory one at a time. However, the solution convergence is relatively slow, inasmuch as the equations are solved in a decoupled manner.

Unlike the segregated algorithm described above, the pressure-based coupled algorithm solves a coupled system of equations comprising the momentum equations and the pressure-based continuity equation. The remaining equations (*i.e.* scalars) are solved in a decoupled fashion as in the segregated algorithm. Since the momentum and continuity equations are solved in a closely coupled manner, the rate of solution convergence significantly improves when compared to the segregated algorithm. However, the memory requirement increases by 1.5 - 2 times that of the segregated algorithm since the discrete system of all momentum and pressure-based continuity equations needs to be stored in the memory when solving for the velocity and pressure fields (rather than just a single equation, as is the case with the segregated algorithm). An overview of the two pressure-based solution methods is showed in Figure 3.1.

For our computation, the segregated pressure-based solver has been used.

Pressure-Velocity Coupling

Solution of Navier-Stokes equation is complicated even because of the lack of an independent equation for the pressure, whose gradient contribute to each of the three momentum equations. Moreover, for incompressible flows like we have been dealing with, the continuity equation does not have a dominant variable, but it is rather a kinematic constraint on the velocity field. Thus, the pressure field (the pressure gradients when incompressible) should be generated by satisfying mass conservation. Several approaches for pressure-velocity coupling are possible. We choose the classical SIMPLE and SIMPLEC(consistent) schemes, which are useful mainly for steady computations and low-skewed grids, even if some unsteady case was run, and in spite of the high degree of distortion within the mesh. This because convergence appeared acceptable, even when compared to the PISO scheme which is usually the best option for transient computations. Proper under-relaxation factors were set for the different investigated solutions.

Discretisation scheme

The following discretisation scheme have been used within the project

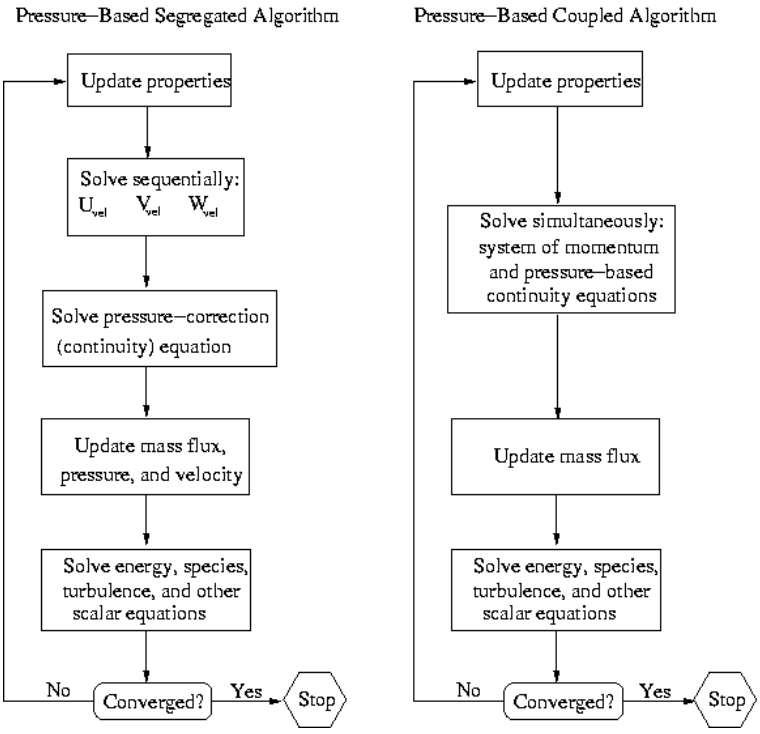

Figure 3.1: *Overview of segregated and coupled pressure-based algorithms [24]*

- First-Order Upwind scheme
- Second-Order Upwind scheme
- QUICK scheme

The temporal discretisation used for unsteady computations was first order accurate. For pressure interpolation, the schemes adopted were the default interpolation, which computes the face pressure using momentum equation coefficients and the PRESTO (*PREssure STaggering Option*).

The first procedure works well as long as the pressure variation between cell centres is smooth. When there are jumps or large gradients in the momentum source terms between control volumes, the pressure profile has a high gradient at the cell face, and cannot be interpolated using this scheme. Flows for which the standard pressure interpolation scheme will have trouble include flows with large body forces, such as in strongly swirling flows, natural convection and the like. In such cases, it is necessary to pack the mesh in regions of high gradient to resolve the pressure variation adequately. Another source of error is that Fluent assumes the normal pressure gradient at the wall is zero. This

is valid for boundary layers, but in the presence of body forces or curvature is not. Again, the failure to correctly account for the wall pressure gradient is manifested in velocity vectors pointing in/out of walls.

The PRESTO scheme uses the discrete continuity balance for a *staggered* control volume about the face, to compute the staggered (*i.e.* , face) pressure. This procedure is similar in spirit to the staggered-grid schemes used with structured meshes.

Modelling flows with rotating reference frames

The equations of fluid flow are usually solved by Fluent in a stationary (or *inertial*) reference frame. However, there are many problems that require the equations be solved in a moving (or *non-inertial*) reference frame. A rotating rotor of a wind turbine is such case. With a moving reference frame, the flow around the moving part can be modelled (with certain restrictions) as a steady-state problem, with respect to the moving frame.

Fluent's moving reference frame modelling capability allows to model problems involving moving parts by activating moving reference frames in selected cell zones. When a moving reference frame is activated, the equations of motion are modified to incorporate the additional acceleration terms which occur due to the transformation from the stationary to the moving reference frame. By solving these equations in a steady-state manner, the flow around the moving parts can be modelled.

For simple problems, it may be possible to refer the entire computational domain to a single moving reference frame. This is known as the single reference frame (or SRF) approach.

Defining Boundary Conditions

Boundary conditions (BCs) specify the flow variables on the boundaries of the chosen physical model. They are therefore a critical component of a simulation, and it is important they are specified appropriately. The utilized boundary conditions follows, named as reported in the next chapters

- *Wall (no-slip)*
  Wall BC are used to bound fluid and solid regions, for instance the blade surface in a wind turbine model. The no-slip condition is the default setting for viscous flows and the shear-stress calculation in turbulent flows follows the adopted turbulent model.

- *Wall (Euler)*
  Instead of the no-slip condition, a *ideal-slip* or *Euler-slip* can be specified, which might be useful to limit the influence from artificial boundaries too close to the model, *e.g.* the computational domain shell.

- *Velocity-Inlet*
  Velocity inlet boundary conditions are used to define the flow velocity, along with all relevant scalar properties of the flow, at flow inlets. This BC is suitable for incompressible flows, whereas for compressible flows will lead to a non-physical result because stagnation conditions are floating. It is possible so set both constant and variable parameters, as well as they can be alternatively uniform or non-uniformly distributed along the boundary itself.

- *Pressure-Outlet*
  It means that a specific static pressure at outlet is set, and allows also a set of backflow conditions to minimize convergence difficulties. The radial equilibrium distribution is also added for rotating domain simulations, so that pressure gradient is given as a function of the distance from the axis of rotation r and the tangential velocity component v_θ

$$\frac{\partial p}{\partial r} = \frac{\rho\, v_\theta^2}{r} \tag{3.10}$$

- *Symmetry*
  It is the analogous of a zero-shear slip wall in viscous flow. Zero normal velocity is at a symmetry plane and zero normal gradients of all variables exist there as well.

- *Periodic*
  They are used to take advantage from the periodically repeating nature of both the geometries and flow patterns. Periodic boundaries are always in pair and the overlooking volumes on the two surface are direct neighbours, *i.e.* the outcoming flow from one, the incoming flow is into the other.

Post-processing

Fluent allows a complete post-processing of solution data. Most of them are the listed operation at page 23. Moreover, the solution data can be easily exported in a number of common file formats, to be analysed with other post-processing tools.

3.6 LES and DES approach

As an alternative to the Reynolds-averaged methodology, *Large Eddy Simulation* (LES) techniques have been widely explored in the past years. Although LES gives a better physical representation of the eddy dynamics in separated flows, it is still limited to flow problems at moderate Reynolds numbers.

As the RANS equations fail to simulate massive separation, even when simulations are performed in a time-true sense, and large eddy simulations

(LES) are unaffordable, hybrid LES/RANS approaches, such as detached eddy simulation (DES), represent an attractive compromise between computing costs and accuracy. The idea behind hybrid approaches is to combine fine-tuned RANS technology in the boundary layers, and the simple power of LES in the separated regions. In the RANS regions, the turbulence model has full control over the solution through the eddy-viscosity based closure. In the LES region, little control is left to the model, the larger eddies are resolved both in space and time, and grid refinement directly expands the range of scales in the solution. This reduces considerably the computing costs, as compared to a full blown LES.

The DES technique has recently been applied on the NREL Phase VI wind turbine blade under parked conditions by Johansen et al. [17].

Chapter 4

Validation of CFD-RANS computations

In this chapter, wind turbine performances evaluation is carried out and their general aerodynamic behaviour is studied.

4.1 Literature review

Today, industrial design codes for wind turbine rotors are still based on BEM [6][7]. Nevertheless, in the last decade the opinion has been advanced that aerodynamic modelling of HAWT rotors by means of the conventional engineering methods has reached a point where no further improvement can be expected without a full understanding of the flow physics [25]. Thus, the last years have seen the rise of numerical studies on all HAWT aerodynamics features, performed on many different levels, ranging from BEM methods integrated by CFD calculations, to full 3D Navier-Stokes models.

Many authors have used the generalized Actuator Disk Method, which represents roughly an extension of the BEM method, integrated in a Euler or NS frame [15][26]. To overcome its main limitation, *i.e.* the forces are distributed evenly along the actuator disk in the azimuthal direction, a 3D N-S solver has been combined with the so-called *Actuator Line Technique*, in which the loading is distributed along lines representing the blade forces [6][9][15].

In the few past years, Sankar and co-workers [23][27][28][29] developed a hybrid Navier-Stokes/Full-Potential/Free Wake Method, mainly for predicting 3D viscous flow over helicopter rotors and then extended it to the HAWT flow field. The computational domain is divided into different region, each one is solved by the proper approach: N-S solution near the blades, potential flow representation on the outer field, and a collection of vortex methods for the vorticity field modelling.

Full three-dimensional computations, employing the Reynolds averaged Na-

Table 4.1: *Characteristics of the investigated turbines*

	BEM-designed	**NREL-Phase VI**
B, *number of blades*	3	2
D[m], *rotor diameter*	41	10.058
Ω[rad/s], *rotational speed*	2.836	7.5398
airfoil sections	NACA 63-4xx	S809

vier Stokes (RANS) equations, have been carried out by Kang and Hirsh [25], focused on 3-D effects on a HAWT. They have used the EURANUS/Turbo solver with either algebraic and κ–ω turbulence models for closure. Also, at Risø and at DTU/MEK several numerical investigations were carried out on HAWT, using their in-house Navier-Stokes solver EllipSys2D/3D, and dealing with overall performances, loads, design of rotors and blade sections (see for instance [6] and [30]), extreme operating conditions [17], tip shape [31].

At the Department of Mechanical Engineering of the University of Cagliari (DIMeCa) the commercial CFD package Fluent was used to perform a detailed analysis of HAWT flow (see the List of Publications at page 103). The steady flow field around an isolated rotor of a middle-sized HAWT was predicted in a non-inertial reference frame, using both the Spalart-Allmaras turbulence model and the κ–ω SST model, and specifying a constant axial wind velocity at the inlet. The classical BEM method was adopted for the design of a first turbine model, extending the active part of the blade close to the hub. This blade region is aerodynamically redesigned following the tendencies of modern wind turbines [32], as treated in Chapter 5. Several 2D and 3D simulations were carried out, to yield information on the different aspects involved by this problem, ranging from performance calculations to wake development. The results of the computations on the well-known NREL-Phase VI turbine are also presented in this chapter. In table 4.1 the characteristics of the two investigated turbines are summarized.

4.2 Mathematical model

The mathematical model included the Continuity and Momentum equations. These equations were solved in a single Moving Reference Frame (MRF or SRF) attached to the rotor blades, with the assumption of incompressible and turbulent-steady flow. Basically, they are the incompressible steady-RANS classical equations (eq. 3.1 and 3.2), which are written here in tensor notation [33]

$$\frac{\partial \bar{u}_i}{\partial x_i} = 0 \tag{4.1}$$

$$\rho \frac{\partial}{\partial x_j}\left(\bar{u}_i \bar{u}_j\right) = -\frac{\partial \bar{p}}{\partial x_i} + \frac{\partial}{\partial x_j}\left(\bar{\tau}_{ij} - \rho\overline{u_i' u_j'}\right) \tag{4.2}$$

where the tensor takes on the reduced form

$$\bar{\tau}_{ij} = \mu \left(\frac{\partial \bar{u}_i}{\partial x_j} + \frac{\partial \bar{u}_j}{\partial x_i} \right) \tag{4.3}$$

The one–equation Spalart–Allmaras model with standard wall functions (hence with $y^+ \geq 30$) was chosen for the turbulence closure, because it represents a good compromise between accuracy and computing costs (see, *e.g.* [24]). For some calculation, the κ–ω SST eddy viscosity model was used, yielding nearly analogous results. The system of non-linear equations was solved through a segregated approach in all simulations. As the code solves the incompressible flow equations, no equation of state exist for the pressure, and the SIMPLE algorithm was adopted to enforce the pressure-velocity coupling. Second order and QUICK spatial discretisation schemes were chosen for continuity and momentum equations.

4.3 BEM-designed blade geometry

The classical Blade Element Momentum method was adopted for the design of the turbine rotor, using the specifications for an existent HAWT, found in literature [12]. This is the Nordtank NTK 41/500 turbine, equipped with three LM 19.1 blades, which has a rotor diameter of 41 m and a 500 kW rated power. The turbine is of the fixed pitch type, stall regulated. It rotates at a fixed speed of $\omega = 2.836$ rad/s and the nominal wind speed is 6.8 m/s.

The blade sections consist of NACA 63-4xx (in the *outer* part) and FFA-W3-xxx (in the *inner* part) series airfoils. However, the exact distribution of chord and twist angle was not available, neither detailed information on airfoil sections was given. Only NACA 63-4xx profiles data were therefore used in the BEM method computations, and polars were taken from [34]. The computed chord and twist angle distribution along the blade radius are shown in Appendix A, Table A.1.

Figure 4.1: *View of the BEM-designed blade model*

4.4 Computational grid and domain

Neither the tower nor the ground were included into the model, and a uniform wind speed profile was assumed at the entrance of the domain. To generate the volume mesh for the three bladed rotor, the 120 degrees periodicity of the rotor was exploited, by only meshing the volume around one blade. The remaining two blades were included in the computations using periodic boundary conditions.

The pre-processor GAMBIT was used to build an hexahedral mesh of approximately 1.5 million volumes. Around the blade, the grid was H-shaped (Figure 4.2) and it was optimized by means of 2-D simulations, up to a final 70x53 balance, at least sufficient to model the boundary layer with the help of wall functions. Also, the mesh has been refined along both spanwise (with 58 elements in the final mesh) and axial domain direction. Indeed, the first coarse grid, which counted in less than 1 million volumes, even if affected the overall predicted loads for less than 1%, showed a rough resolution of the flow field past the blades, mainly in the near wake region.

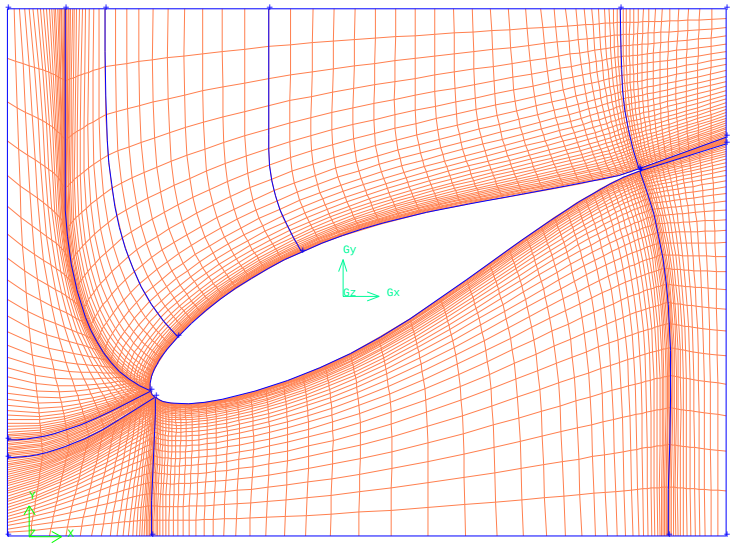

Figure 4.2: *H-mesh around the blade sections*

The computational domain was conical shaped, extending in the axial direction roughly 5 diameters upstream and 10 diameters downstream of the rotor. In the plane of the rotor, the domain diameter was five times that of the rotor. These dimensions have been resulted from a a dedicated study on outer boundaries dependency (Figure 4.3). While keeping the first narrow dimensions, the

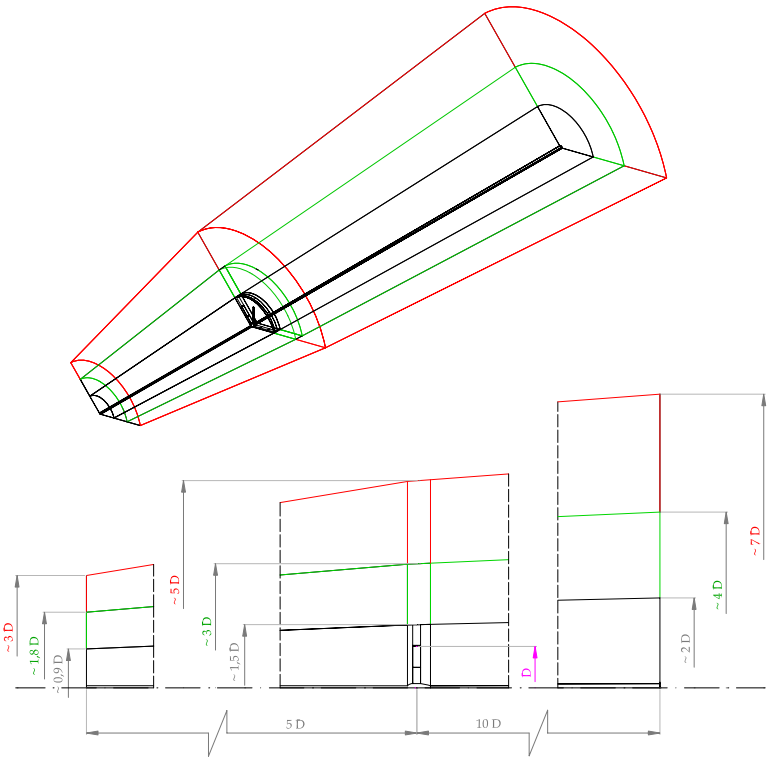

Figure 4.3: *Determination of the domain extension*

rotor worked as in ducted configuration, resulting in a sensible over-prediction of the overall performance (nearly +10% respect to the largest domain, in design conditions). Moreover, the flow tended to accelerate in between the rotor disc and the boundaries, so that the wake too resulted affected by the vicinity of the boundary

In Figure 4.4 are also shown the boundary conditions imposed: at the inlet face and at the lateral boundary undisturbed uniform wind velocity and turbulence were fixed; static pressure was set at the outlet; no-slip condition was selected for the blade and nacelle surfaces.

Mesh generation has presented many difficulties, owing to the different range of geometric scales represented: length of the domain (600 m), size of the rotor (41 m), typical chord lengths (0.5÷3 m), and boundary layer thickness (10 mm). A modular procedure for generating the grid was therefore utilized, in order to take care of the local geometric scales for all those different "levels". A representative image of the mesh generation process is shown in Figure 4.5. By following this logic, a selective modification of each part that constitutes

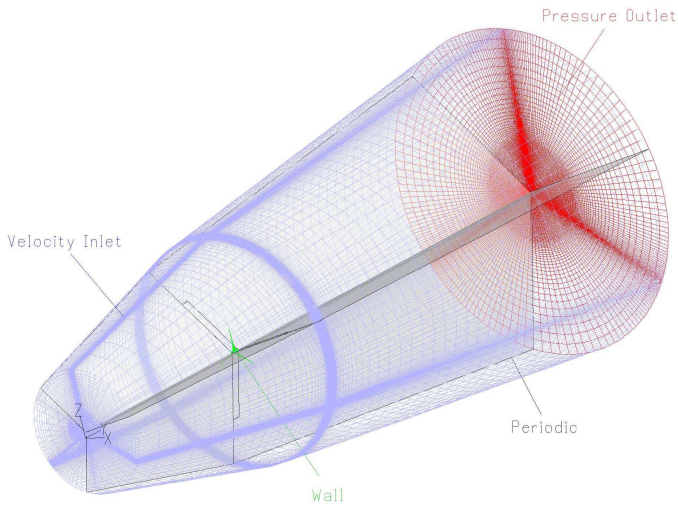

Figure 4.4: *Computational domain and boundary conditions*

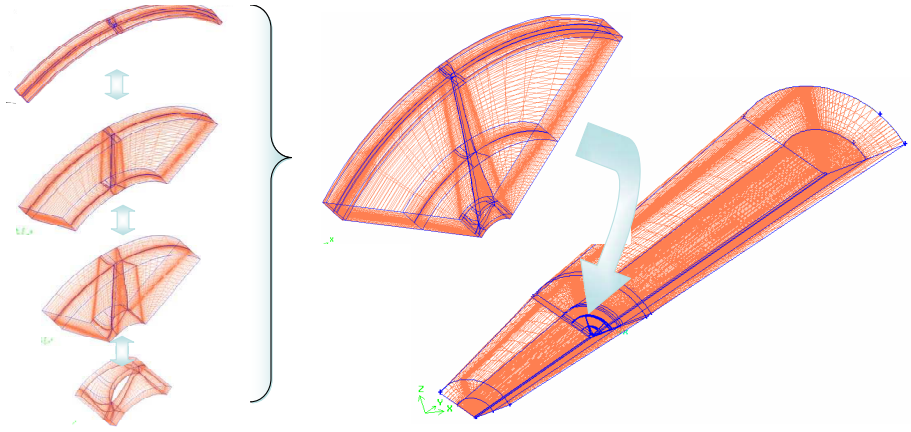

Figure 4.5: *Mesh generation procedure*

the domain is straightforward. Anyway, a critical constraint was imposed by the available computing resources, since all simulations must be run on normal personal computers.

For the far wake prediction, a slightly different configuration of the computational domain was adopted, as will be illustrated in Chapter 6.

4.5 Performances: CFD *vs.* BEM

The commercial code Fluent was used in all the calculation presented. To validate the numerical model, the overall performances for the new designed turbine were computed and compared to BEM calculations.

The performance of a wind turbine can be characterized by three main indicators power, torque and thrust and letting them vary with wind speed [8]. The power determines the amount of energy captured by the rotor. The torque determines the size of the gear box. Finally, the rotor thrust has great influence on the structural design of the tower. Regarding aerodynamics and the subject of this work, the most important among the three is indeed power.

It is convenient to express the performance by means of non-dimensional, characteristic performance (power, torque and thrust coefficients) as functions of tip speed ratio.

The shaft mechanical power as a function of the wind velocity is showed in Figure 4.6, together with the corresponding power coefficient C_P as a function of the global tip speed ratio. The CFD results are found to be in good agreement with those obtained using the BEM method, for the tested undisturbed wind velocities, ranging from 6.8 to 12 m/s, *i.e.* for generally attached flow conditions. At higher wind speeds, however, there are significant discrepancies and unsteady computations are preferable. For deep stall conditions, the lack of the RANS models in predicting the aerodynamic loads is well-known [11].

A comparison to the "inspiring" Nordtank wind turbine data is given in Figure 4.7. The computed Fluent and BEM power coefficients are plotted together with the analogous output from the actuator disc model by Mikkelsen [15], who also provided the power curve measured by Poulsen at Risø. Moreover, the NS computations performed by Sørensen [35], who introduced a suitable transition model to the Risø-DTU EllipSys3D code, are included. The data are not expected to match exactly, at least because the BEM-designed blade does not follow exactly the real shape of the Nordtank turbine. However, it is interesting to note that the CFD computation performed with Fluent have a similar trend to the measured power curve. The last computed value, at 4 m/s free-stream speed, has been not included, resulting in a too high tip-speed ratio, anyway the dashed line gives the tendency for the lower lambdas. It is noticeable that the maximum computed value of C_P is only about 0.49 (and around 0.5 regarding the measurements), achieved at the nominal wind speed of 6.8 m/s. The value is much less than the Betz limit, due mainly to the drag and tip losses for the attached flow conditions (the simple BEM-method adopted here is indeed not able to catch them correctly, and overpredicts the C_P), whereas at the lower tip speed ratios is the stall who plays a major role, in reducing the overall aerodynamic efficiency.

In Figure 4.7 once more, the thrust coefficient computed with Fluent is compared to the results from the actuator disc method. The thrust force on the rotor is directly applied to the tower on which the rotor is supported, so that considerably influences the structural design of the tower.

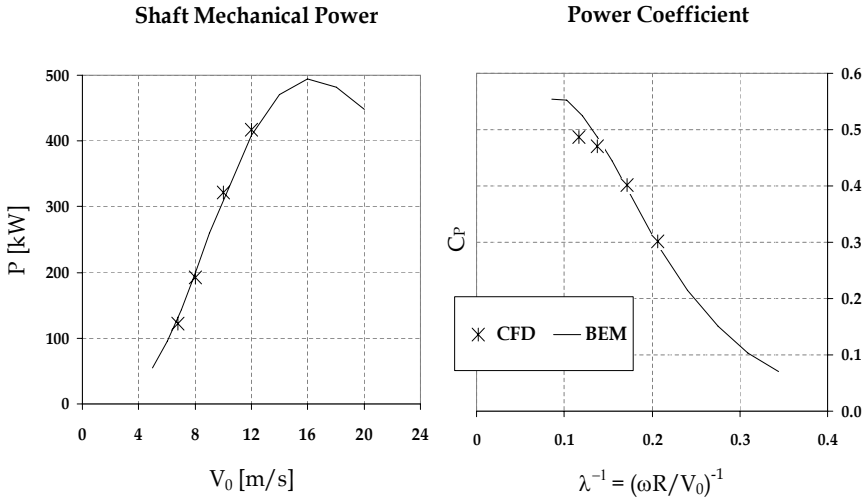

Figure 4.6: *Mechanical power P and power coefficient C_P: BEM method vs. CFD calculations, for different wind velocities, V_0, and tip speed ratios, λ*

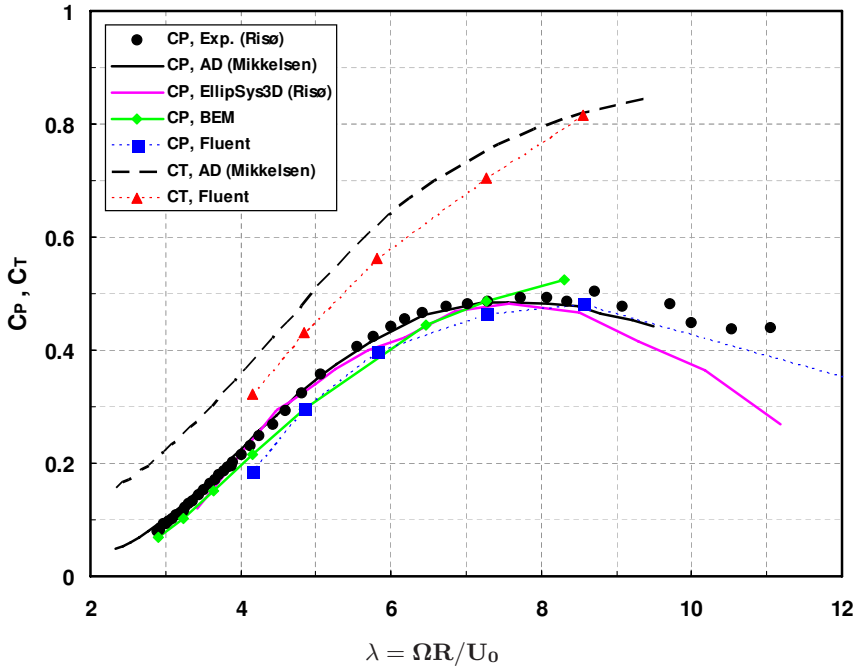

Figure 4.7: *BEM-designed blade, computed C_P and C_T coefficients compared to the Nordtank NTK-500/41 wind turbine measurements and computations*

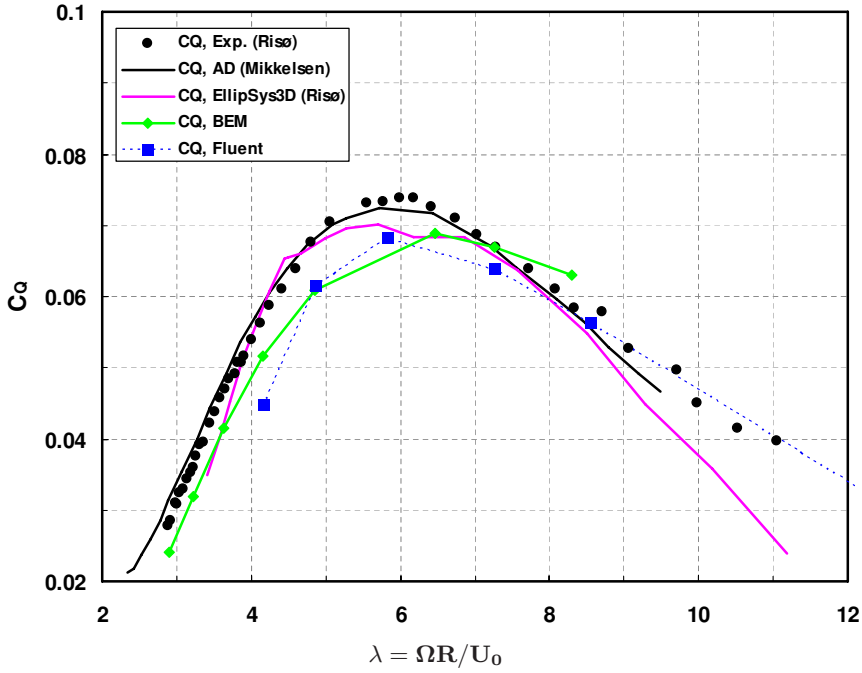

Figure 4.8: *BEM-designed blade, computed C_Q coefficient compared to the Nordtank NTK-500/41 wind turbine measurements and computations*

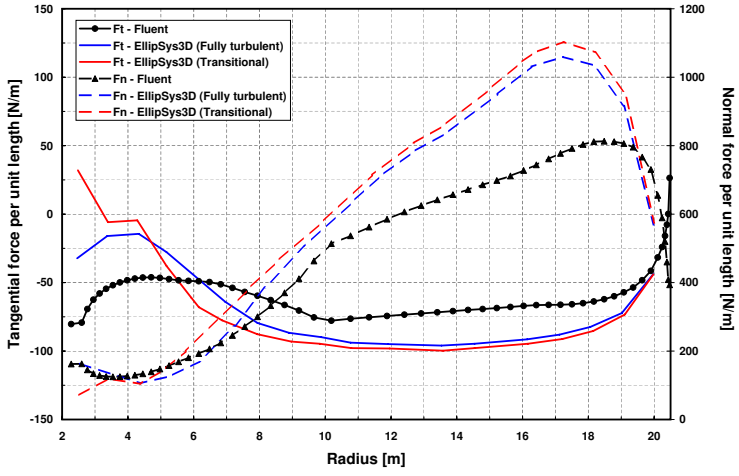

Figure 4.9: *Spanwise variation of the tangential and normal force per unit length. Fluent results (U_0 = 6.8 m/s) are compared to the EllipSys computations on the LM19.1 (U_0 = 7 m/s), stemmed from [35]*

Both the CFD and BEM predicted torque coefficients are compared to the results stemmed from [15] in Figure 4.8. The torque coefficient, C_Q is derived from the power coefficient simply by dividing the tip speed ratio and so it does not give additional information about the turbine performance. The principal use of the resulting curve is for torque assessment purposes when the rotor is connected to a gear box and generator.

Finally, the computed spanwise distribution of tangential and normal forces per unit length are plotted in Figure 4.9. Fluent results are compared to the EllipSys3D computations performed at Risø by N.N. Sørensen on the real LM19.1 blade [35]. The operating conditions are slightly different, but the two geometries are evidently more. The local sections are expected to behave differently, whereas the global values tend to agree better, since the same global parameters were set as an input to the BEM-design method. However, a qualitative agreement is found between the curves. It is noticeable that the driving force of the BEM-designed blade, which is generally lower, is larger in the inner part, since the real LM19.1 presents there a cylindrical connection to the hub. The heavily loaded part of the blade ranges anyway from the middlespan up to the tip, where a natural decay in loading exist.

4.6 Rotor aerodynamics

In the following, some representative numerical results, dealing with rotor aerodynamics, are collected.

First, in Figure 4.10 the limiting streamlines on the suction side of the BEM-designed turbine blade are outlined, for a freestream velocity of 10 m/s. For the lower speed range, analogous traces were plotted, evidencing attached flow for the whole blade surface up to 7 m/s, whereas separation originated only at 8 m/s, in in the very inboard portion, with an early vortex structure, whose development is still visible for the 10 m/s case. But is the 10 m/s case that shows a large stalled area on the blades. At the root, the flow is also influenced by the nacelle, strong recirculation are visible, even with radially downward secondary flow. While going outward, the tendency is opposite, as expected. In the separated zone the radial flow direction is mainly centrifugal and the limiting streamtraces merge into a separation line, which runs along as longer as the three-fourths of the whole blade span. The predicted results can be qualitatively compared to the CFD-RANS computations performed with EllipSys3D on the Nordtank wind turbine by Johansen and Sørensen, *e.g.* in [36], resulting in a fair agreement. They also remarked how fully-turbulent CFD-RANS computations usually overpredict power at high wind speed for such stall-regulated turbine.

Figure 4.11 shows the distribution of the axial interference factor, $a = 1 - V_a/V_0$, in the rotor plane. A large change in a takes place across the blades, due to the effects of the bound vorticity located on the blade.

The tip geometry was obtained by simply truncating the blade with a cylin-

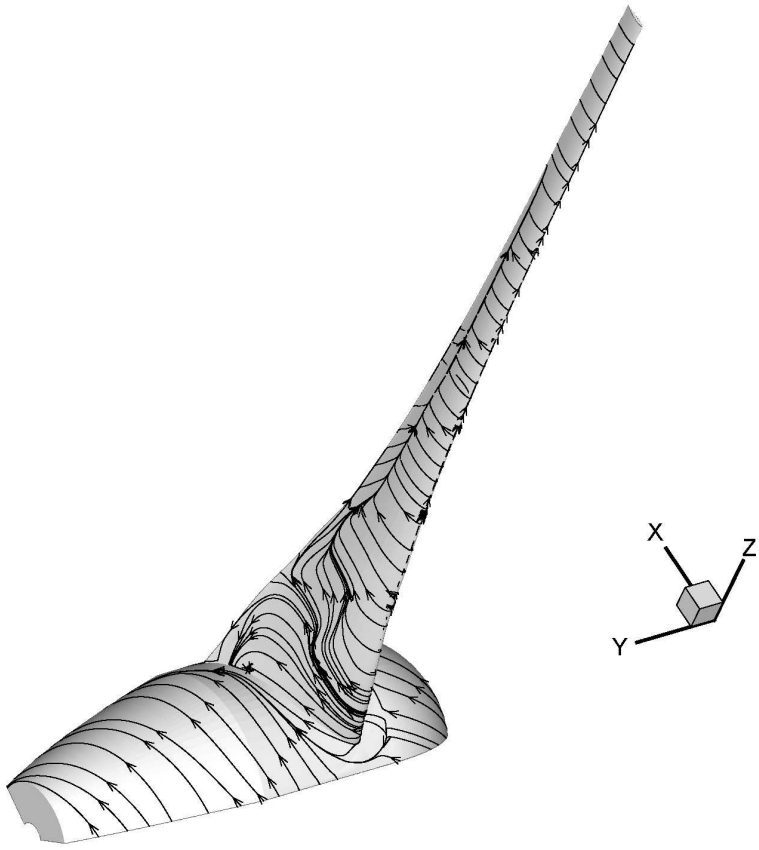

Figure 4.10: *Streamtraces on blade surface, BEM-designed blade at U = 10 m/s*

drical surface. Hence, the simulations revealed the formation of strong tip vortices Figure 4.12, which in Figure 4.11 appear as a localized region with negative a-values: here the axial velocity is higher than the inflow wind speed. In Chapter 5, the study of different tip geometries has been presented, more accurately shaped, in order to verify if this allows a reduction of fluid dynamic and consequently acoustic tip effects. The pathlines are coloured with the radial velocity component, evidencing the high values of spanwise directed flow at the blade tip (the tangential velocity is there about 58 m/s).

Finally, pathlines even coloured with the radial velocity component (Figure 4.13) show the relative flow field patterns near the blade root, where strong 3–D effects can also be found. Just as a vortex is shed from each blade tip, and a vortex would also have been shed from each blade root, if the classical hub connection had been kept. However, it is evident the origin of a *core*, or *root*,

vortex behind the nacelle. This root vortex is also responsible for inducing a tangential velocity in the wake.

Further discussion on tip and root vortices is carried out in Chapter 6, which is focussed on the wake analysis.

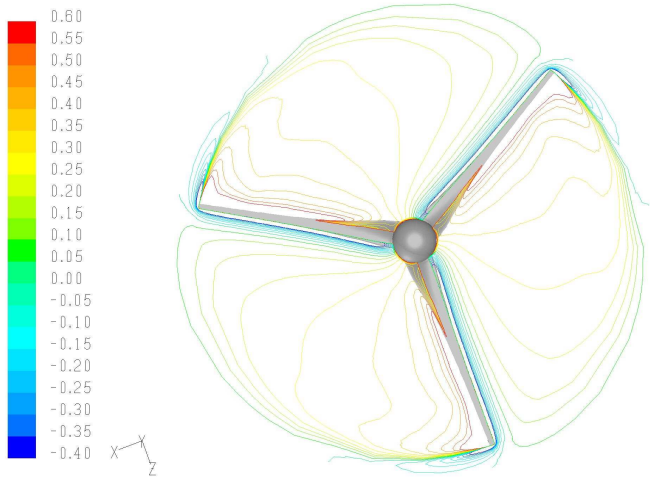

Figure 4.11: *Axial induction factor, a*

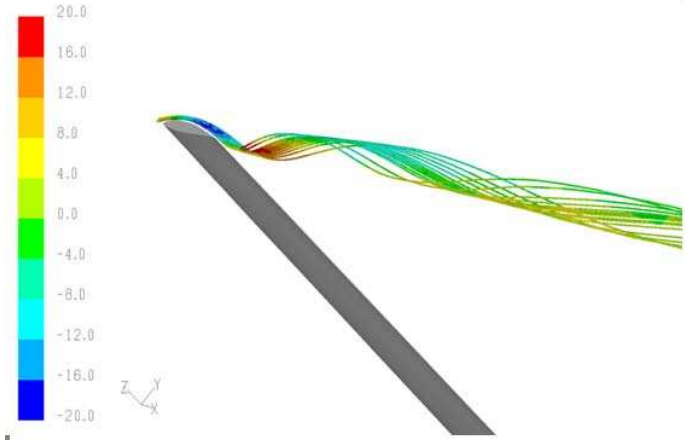

Figure 4.12: *Pathlines at the tip for the BEM-designed rotor, coloured with the radial velocity component, at $U = 6.8$ m/s*

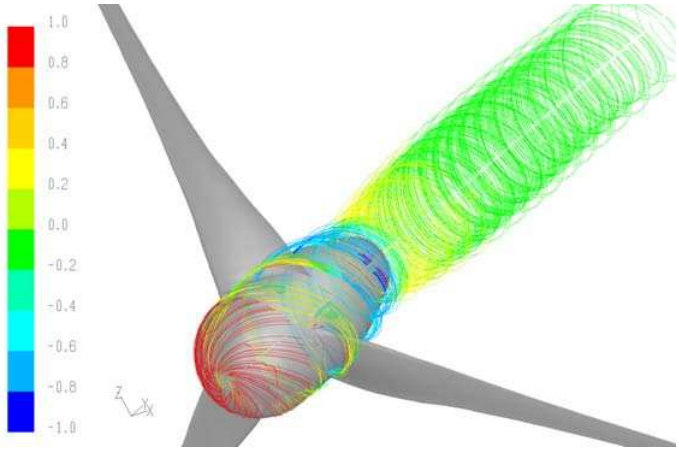

Figure 4.13: *Pathlines at blade root for the BEM-designed rotor, coloured with the radial velocity component, at U = 6.8 m/s*

4.7 The NREL/NASA Ames rotor

The release of the measurements on the NREL Phase-VI rotor has heavily influenced the CFD activities dealing with wind turbine rotor aerodynamics. This unique data set, with several well-documented cases, has given a new possibility to test details of state of the art CFD codes. In the years since the release of the measurements nearly half of all published CFD studies of wind turbine rotors deals with these measurements [11].

The NREL/NASA PHASE VI experimental campaign [37], carried out at Ames wind tunnel (which is the world's largest wind tunnel) was chosen for a broad validation of the computed results, as well as for the late analysis on the rotational effects (see Chapter 7).

The NREL/NASA Phase VI test turbine was built from a Grumman Wind Stream-33. A 10 m diameter, stall-regulated turbine with full-span pitch control, which and had a power rating of nearly 20 kW. Many modifications were made to this turbine, prior to the wind tunnel test. The turbine used during the wind tunnel test was a two-bladed turbine, with twisted and tapered blades, and was tested in both upwind and downwind rotor configurations. The main characteristics of the turbine are summarized in Table 4.1, together with the BEM-designed one.

The effective geometry of the turbine and all details of the tunnel facilities and the experimental setup are even found in [37], while a sketch of the planform dimension is illustrated in Figure 4.14. A picture of the turbine during wake measurements in Nasa Ames wind tunnel is also reported, in Figure 4.15.

The NREL turbine has been simulated under a freestream wind speed ranging from 4 to 12 m/s, with low inflow turbulence levels (1% and length scale

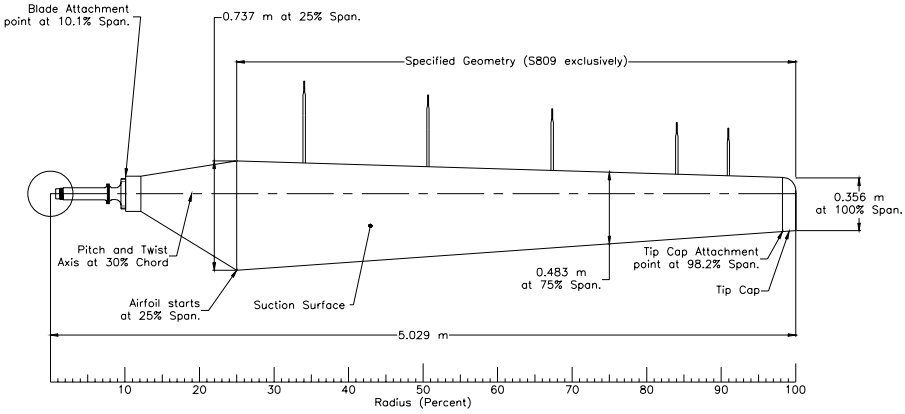

Figure 4.14: *NREL Phase VI, Blade planform dimensions (see [37], p.21)*

Figure 4.15: *NREL 10-m Wind Turbine Testing in NASA Ames 80'x120' Wind Tunnel* `http://wind.nrel.gov/amestest/`

of 0.1 m). The blades rotated counterclockwise. The experimental tests were performed for different blade pitch angles. Nevertheless, the available data set are mainly referred to the 3-degree pitched case. Till now, the CFD study only provides the results for the *zero-degree* pitch, so that the validation comparison should be qualitative.

Since the tunnel test section size was 36.6 x 24.4 m, a circular section of same area was chosen for the computational domain, *i.e.* 32 m wide.

The mesh resolution was refined in the proximity of the wall boundaries, in order to get y^+ of around 2-3, which means that a direct solution of the BL flow was affordable (using the k-ω SST turbulence model). Around the blade sections a 140x50 structured H-mesh has been generated, while 74 cells have been distributed along the blade span. At the tip, an unstructured mesh block was added, with 2600 *pave* quadrilateral cells over the tip surface and 34 elements along the span, as is shown in Figure 4.16.

The total number of cells was about 3.5 millions, see Figure 4.16.

Unsteady computations

Unsteady flow computations were run, with two main goals. The first was to perform a gradual change in the boundary conditions at inlet (i.e. the constant axial–velocity variable), which allowed the convergence to be reached faster. At that purpose, a simple UDF-function was written in C++ language and interpreted in Fluent environment, with a time–step-dependent law, for incrementing the velocity magnitude.

Second, since concerning rotational effects the main interest is on the separated flow regions, a unsteady flow solution was preferred, for the whole operating range of the NREL turbine. Results have been compared to the steady computations, as well as with the UAE Phase VI experiment data. Consequently, the mathematical model was modified, regarding momentum equations 4.2, while continuity equation (4.1) was kept the same, being the fluid incompressible.

$$\frac{\partial}{\partial t}\left(\rho\bar{u}_i\right) + \rho\frac{\partial}{\partial x_j}\left(\bar{u}_i\bar{u}_j\right) = -\frac{\partial\bar{p}}{\partial x_i} + \frac{\partial}{\partial x_j}\left(\bar{\tau}_{ij} - \rho\overline{u_i^{'}u_j^{'}}\right) \tag{4.4}$$

Reminding there is no difference between mass-weighted and conventional variables for incompressible flows.

4.7.1 Results analysis

shaft-power curves of the turbine. The dashed line represents the measurements, whereas the computed cases are marked with squares. In the wind tunnel test, the pitch was kept equal to 3 degree. On the other hand our simulations were all run with zero pitch. Consequently, even if a general agreement is visible between the two curves, a sensible offset had to be expected. When

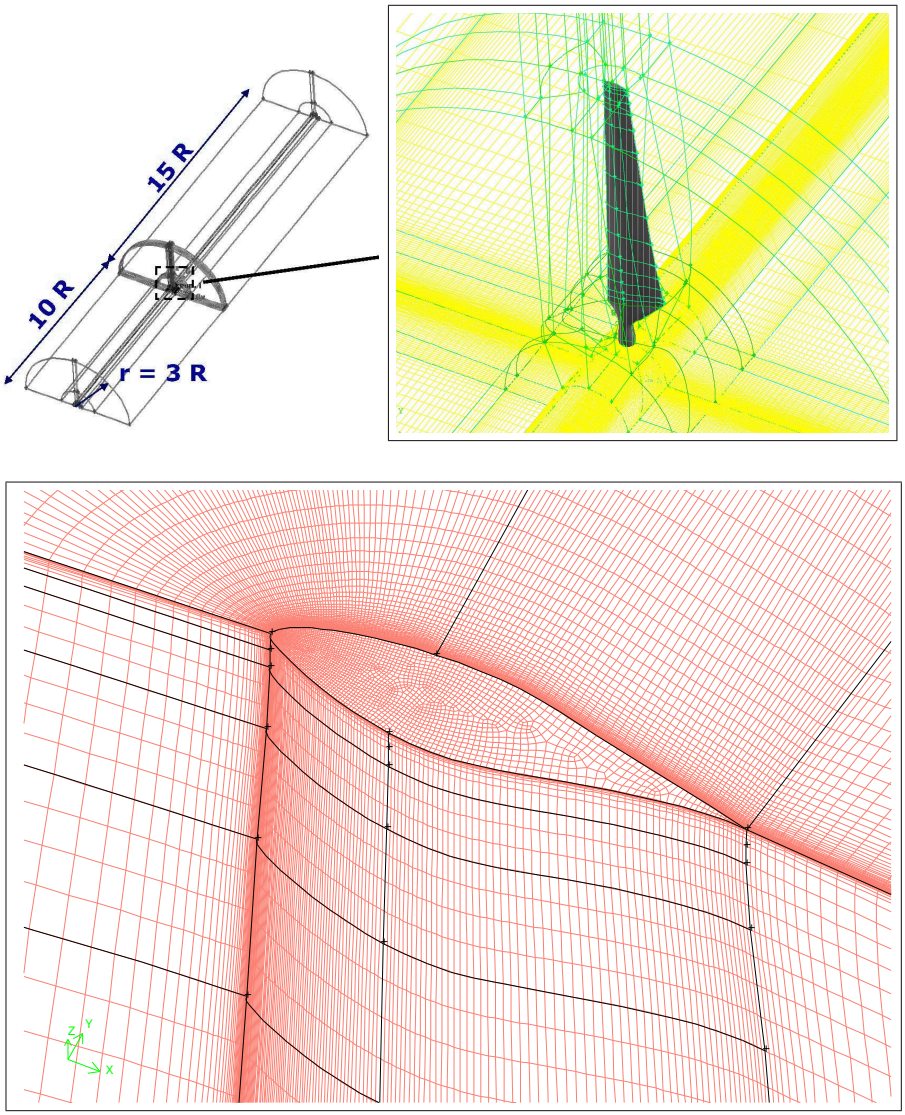

Figure 4.16: *NREL Wind Turbine: domain and close up of the grid around the blade and at the tip*

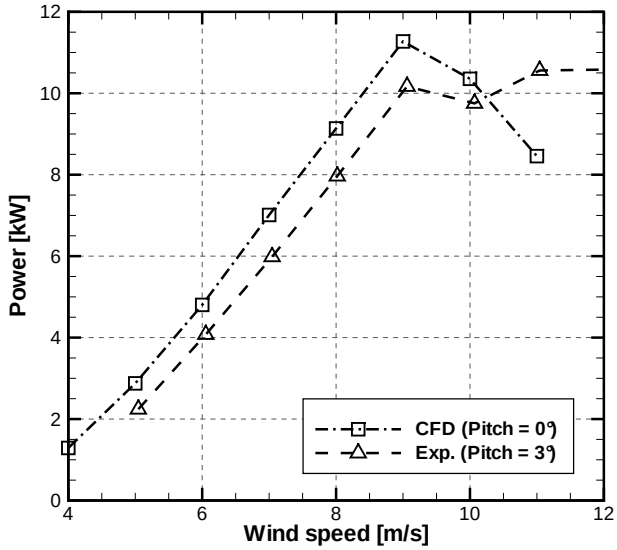

Figure 4.17: *NREL Wind Turbine, measured and predicted rotor power*

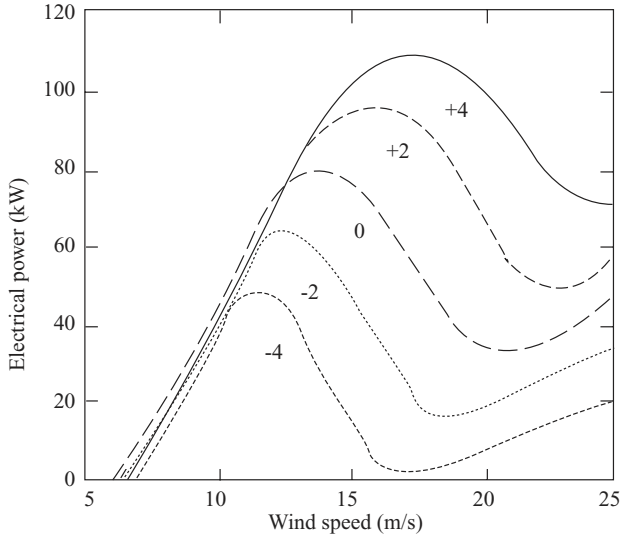

Figure 4.18: *Effect on extracted power of blade pitch set angle (BEM) [8]*

comparing to the typical power characteristic of a pitch-controlled wind turbine (in Figure 4.18 is a BEM-computed dataset, stemmed from [8]), a similar trend to that in the previous plot is found. Nearly before the peak, the two curves look parallel. After the peak, together with the occurrence of stall, the zero-pitched curve descends below the 3-degree one (again the problems in predicting correctly the stall with RANS are evoked).

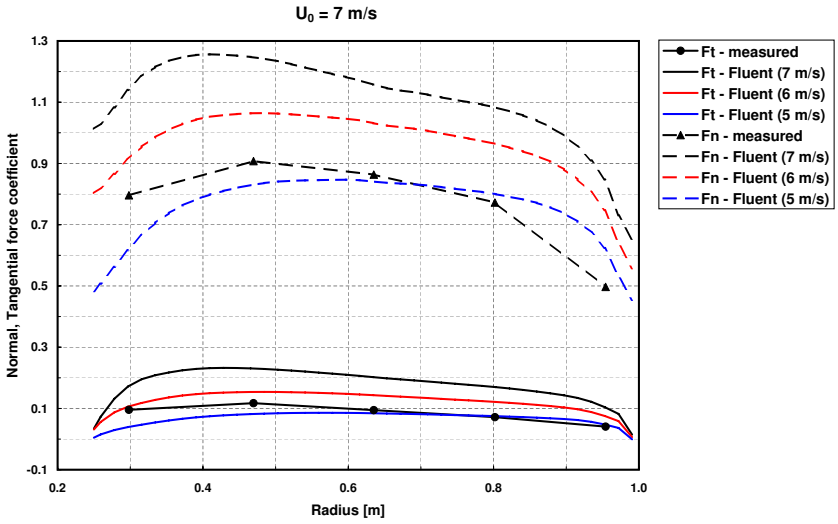

Figure 4.19: *NREL blade, spanwise distribution of tangential and normal force coefficients*

In Figure 4.19 the spanwise distribution of normal and tangential force coefficients is plotted. The measured data for the 7 m/s freestream speed case (see [23]), which is characterised by fully attached flow, are reported for a qualitative assessment. Since the computed case concerns a zero-pitched condition, the three-degree pitch angle of the experimental tests causes the forces coefficient to be generally lower, as well the effective flow incidences are minor. Thus, C_N and C_T values for the 5 m/s and 6 m/s wind speed cases are included and it is noticeable that the lower speed has a good agreement with the measured data in the outer part of the blade, whereas at the inboard the distance between the 7 m/s curves is smaller, due to the large twist angles that make the pitch variation less sensible. Nevertheless, the general tendency appears to be consistent. About the radial loading distribution, further comments will be addressed in Chapter 7, dealing with rotational effects, and particularly with lift and drag forces.

Chapter 5

Design analysis and optimization

This chapter deals with the aerodynamic design of modern wind turbine blades. The capabilities of CFD-RANS as an optimisation method have been investigated and the root and tip blade shapes have been studied. The chapter is split in two main sections, one referring to the root blade design, the other dealing with the tip geometry analysis.

5.1 Root blade design

In the last years, improved performances have been declared for some commercial turbines with an innovative blade design, in which the aerodynamic active part of the blade is extended to the hub and their distinctive drop-shaped generator housings are conceived with the help of famous architects (*e.g.* Norman Foster for Enercon®, see *e.g.* figure 5.1. Is this a matter of fashion and commercial strategies, or valuable benefits can be really achieved by adopting the new rotor shapes? Believing in the wind turbines manufacturers, considerable advantages really exist.

It was almost outstanding to read in 2004 the article by Rohden [32], who stated that for the new 2 MW Enercon E-70 (71 m rotor diameter), which had adopted the new blade root section, even if together with more slender blades and a new optimized tip, "*the new blades generate a measured and certified increased yield of 12-15 per cent compared to neighbouring E-66/20.70 (70 m rotor diameter) wind turbine*".

Note that the re-designed hub region characterizes our WT models since the early studies, which are summarized within this thesis, so that more details about the geometry can be found in the Chapter 4.

The effect of increasing the blade sections chord and twist angle in the vicinity of the nacelle, with regards to the rotor aerodynamic efficiency, has

been recently investigated by other authors. Johansen and his colleagues at Risø [38] for instance approached the problem with three different aerodynamic methods, *i.e.* the BEM method, an Actuator Disc (AD) method and a full 3D Navier-Stokes (NS) solver.

The issue of optimizing the inboard of wind turbine rotors is indeed a rather new matter. For years, on most wind turbines the classic rotor blade design was characterized by a cylindrical connection to the hub. This solution, while overcoming structural limits, caused a lack of yielded power. Generally, it was believed the amount of produced power in the inner part of the rotor was not significant. Also observing that with classical BEM methods the local power coefficient goes to zero when local tip speed ratio λ tends to zero as well, *i.e.* while approaching the root.

Otherwise, as theoretically noticed several decades ago by de Vries [39], including the effect of wake expansion together with the deficit of the static pressure in the wake, the local C_P can exceed the Betz limit when $\lambda \to 0$. This effect is not taken into account by standard BEM methods, so that could result in non-optimal blade design of the inner part of the blade.

Only in recent years, significant progress in new materials and structural design, with the contribution of accurate CFD studies, has led to a new rotor design, where the active part of the blade is extended to the hub, which has normally a greater diameter.

The purpose of our study was therefore to investigate whether an increase in chord and twist distribution will result in an increase in power production and global power coefficient.

Hence, we performed the computations on a middle-sized HAWT with this innovative aerodynamic design tendencies (Figure 5.2), as well as on a classically shaped turbine, *i.e.* a rotor for which the inner part is configured only on structural issue (look at Figure 5.3). The model geometry in both cases is inspired by the Nordtank NTK 41/500 wind turbine, equipped with three LM19.1 blades. The general characteristics of the real turbine (Table 4.1) were used as an input for the BEM-design code and a *new* blade geometry was generated. Since from the early model, which has been already presented in Chapter 4, the innovative inner part design was adopted. For the present study, the inboard sections were changed into the classical concept, *i.e.* a cylindrical mast ranging from 10% (up to the nacelle) to nearly 20% of the whole blade span. Concerning the outer sections, the two blades are identical. Also the nacelle was kept the same, in order to perform a proper comparison, even though in the classical concept should have been certainly smaller.

5.1.1 CFD-RANS simulations

The NS solver Fluent® has been used for the full 3–D RANS wind turbine rotor computations. The mathematical model has already been presented in Chapter 4. Here again all computations are performed by assuming a steady state condition, within a moving reference frame, and the turbulent eddy vis-

Figure 5.1: *Classical and innovative hub-region in real-life*

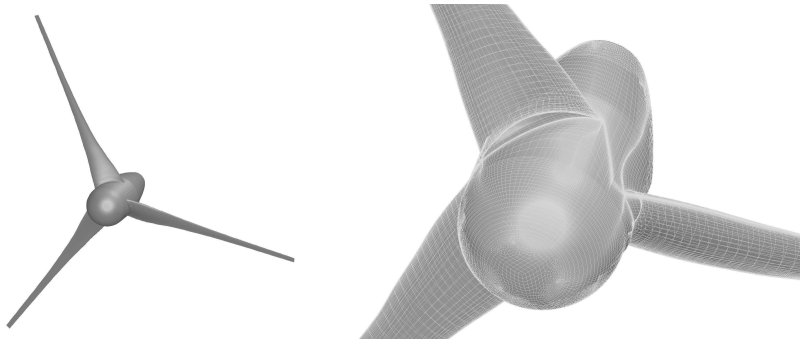

Figure 5.2: *Innovative blade inboard design*

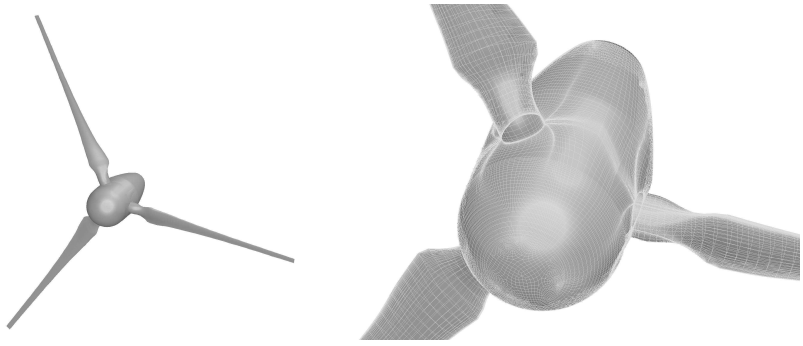

Figure 5.3: *Classical blade inboard design*

cosity has been modelled using the SA turbulence model. Constant inflow velocity was set at inlet, with a low turbulent intensity, and a pressure outlet condition was placed approximately 5 rotor diameters downstream. No–slip condition has been assumed for the surface of the blades and the nacelle. The generator housing is rotating together with the blades, in contrast to the real applications where only a small portion (*hub*) rotates, but this allowed to keep the model simple. Indeed, the *Single Moving Reference Frame* model (SRF) was utilized, instead of a *Multiple* one that is required if portions of the computational domain rotate at different angular speed (or one rests when others move).

A considerable effort was put in generating the computational grid, which is of the structured type. The volume mesh has been generated with Gambit and consists in about one–and–a–half millions of volumes in total. The grid topology is better described in Chapter 4 and was generated modularly, so that the inner block of the blade has been changed within the studied cases. The mesh resolution resulted from the study carried out on the early 3D model and on the 2D airfoil sections, as well as the domain size determination. By choosing the wall function approach to model the boundary layer flow, y^+ values between 30 and 60 were kept all along the blade surface.

As already noted, the two configurations only differ for the very inner sections of blade, while the egg-shaped housing has been kept the same. Otherwise, in real classical applications the nacelle is typically a sort of parallelepiped box, with a quite small hub at one side, which is the only rotating part, together with the blades that are joint just on this part. Moreover, it is important to point out the new design is merely based on BEM considerations and no accurate methods for the spanwise coupling at the root were accounted.

Three wind speeds have been computed, *i.e.* 4, 6.8 (nominal speed) and 8 m s^{-1} at fixed rotational regime. Results are presented as global power and power coefficients. The values found are compared in Table 5.1, showing that innovative blade allows a 5 percent increment of the power coefficient, for design conditions, and even more at lower wind speed. Indeed, this new machines start to operate at very low wind speed (the *cut-off* is around 2.5 m/s), also for adopting sophisticated control systems. Nevertheless, it should be said that, according with Johansen and co–workers [38], global C_P and C_T increase only slightly, indicating complex spanwise dependency not accounted for in BEM methods, which are of course more optimistic, while accurately shaping the blade inboard.

5.2 Blade-tip study

In modern wind turbines the global tip–speed ratio λ assumes high values. However, even if such a small portion of the whole blade has a limited influence on power, it is important for noise emissions control, for the structure and dynamic behaviour of the blade itself.

Table 5.1: *Global performances of the traditional and the innovative blade root design*

Wind speed [m/s]	Rotor design	Power [kW]	Power coefficient	
4.0	*Traditional*	11.6	0.224	
	Innovative	13.5	0.263	(+17.4%)
6.8	*Traditional*	117.0	0.465	
	Innovative	122.7	0.487	(+4.9%)
8.0	*Traditional*	185.6	0.448	
	Innovative	192.5	0.470	(+4.9%)

On the other hand, understanding tip aerodynamics is rather a complex problem and the classical BEM methods and lifting line techniques, widely used in industry, result inadequate. Moreover, detailed full-scale measurements of pressures and velocities for modern multi-megawatt wind turbines are often unfeasible, whereas small machines (*mini* and *micro* wind turbines) and scaled models can be tested in wind tunnel.

The preferable approach for the aerodynamic analysis of blades tip is then the numerical solution of Navier–Stokes equations. However, a detailed analysis of both aerodynamic and aeroacoustic features would need large computational resources, if the last numerical techniques were applied without any model simplification. Arakawa *et al.* [16] for instance performed a compressible-LES simulation on a full-scale wind turbine, aimed at the reduction of tip blade noise. Due to the fine grid employed for modelling directly by LES the acoustic near field of the entire blade, the total number of grid nodes was 320 million and simulations could have been run on the powerful workstation named Earth Simulator.

In this study the steady CFD-RANS approach has been directed to the tip shape analysis, and the problem has been modelled in two steps.

- First, only a frame of the flow field around blade tip has been considered.
- In a next phase, the entire rotating blade has been considered.

In the first model, rotation has been neglected for the sake of simplicity (see *e.g.* [40]) and a steady wind flows over the tip blade portion at rest. Nowadays this simplification can be seen as out-of-date regarding to modern powerful computers, but it is considered a proper first approach to the problem, since we wanted to focus the study on a restricted area including the very near wake.

The analysis has been later extended to the whole rotor, taken while rotating according to newer studies [41][31][42][18]. The considered blade geometry is the same as in the previous chapters, *e.g.* the BEM-modified LM19.1. All the results obtained are compared to the simplified approach for a rough validation.

In the following, some features of the tip blade design problem are introduced, then two different geometrical configurations are presented. The

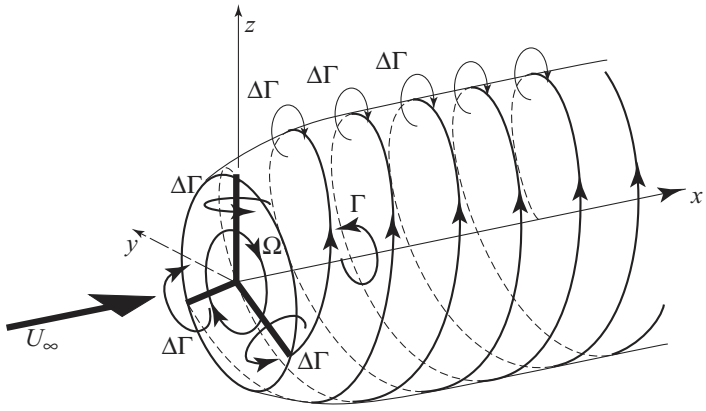

Figure 5.4: *Scheme of the helical wake which origins from the wind turbine rotor, by considering a constant circulation* $\Delta\Gamma$ *on each blade, [8] p.53*

adopted mathematical model is summarized, as well as the solver settings are indicated. While describing the simulation for the no–rotating tip–portion of the blade, the grid is shown together with the imposed boundary conditions. This first step is completed with a depiction of the yield results. By means of various graphical representations of the variables of interest, the differences between the two modelled geometries are put into evidence. Afterwards the full–rotor study simulations take place. We used periodic boundary conditions, solving in the moving reference system only one blade, by neglecting the tower, the nacelle and the terrain. Finally, the whole results are proposed.

5.2.1 Blade-tip of wind turbines

Blade tip's flow is strongly 3–D and is often associated with separation. It means that viscous effects are key determinant. Hence, simple models (*e.g.* inviscid/potential flow, actuator disc and BEM) cannot solve such a complex flow field (see Figure 5.4) accurately. On the other hand, the main phenomenon which one relate to the tip blade, *i.e.* vortex system which origins from there and propagates into the wake, is easy to find out even using simpler methods like lifting line or lifting panel methods [40]. Indeed, the bound vortices produce modifications of the local flow incidence and consequently of the aerodynamic loads. Such change can be estimated with a lifting line model too, even though it does not solve correctly the flow field in the proximity of the blade surface.

More recently, the research conducted on tip blades has developed new design solutions, some of them borrowed from aeronautics like the so-called *winglets* [42]).

A wide set of tip geometries has been proposed within industry, probably

because of the lack of a theoretical approach to the problem. The design of tip blades is still rather empirical and for a long time no distinction was made between the tip portion and the rest of the blade. The same criterion was used everywhere, *i.e.* maximizing efficiency, but following that approach the tipŠs profile, chord length and twist angle choice were derived from the BEM theory, despite the inadequateness of the method to take into account the complex problem associated to that part of the blade.

In the last years a new design concept has been introduced, finalized at minimizing the cost of the produced energy. The goal is no more the maximum energy efficiency in–design conditions, but a balance between energy production and structural resistance to both static loads and fatigue (*multi-point* design). Consequently, the present tendency is at tapering off the blade while going outwards, by reducing the chord length as much as possible (at least zero). Thus, a more slender blade results from the multi-point design.

Blade-tip design

The optimum design of tip blade of a wind turbine can be pursued taking into account of the following issues:

- noise reduction
- aerodynamic and aeroelastic behavior
- robustness and transportability
- aesthetics

For many years the dominant tendency for blade design was given by the first manufacturers with their well–established experience. The geometry of tip blades comes from some practical considerations and from the popularity of the existing products. On the other hand, the aerodynamics of wind turbine blades have been the object in recent times of increasingly attention by designers and manufacturers. The blade shape has been refined, new dedicated airfoils have been arranged and the classical design methods have been improved. Moreover, on the outboard are focused the aeroacoustic studies, which are becoming more relevant for the environmental sustainability of the wind market growth.

Rectangular and tapered blade-tip

Two different geometries for the blade tip of a middle-sized HAWT (D = 41 m, P = 500 kW) are considered here. The rectangular one follows the indications of the BEM method up to the end section, hence is simply truncated (see Figure 5.5). The other one is tapered according with the classical industrial tendencies (see Figure 5.6). However the more recent machines, with the help of new studies and overtaking the well–established concepts, present an evolved shape, sometimes with tip devices borrowed from aeronautics. This becoming

Figure 5.5: *Rectangular tip blade*

Figure 5.6: *Tapered tip blade*

more and more important especially for the modern big turbines, *i.e.* the so–called *Multi-Megawatt*.

Mathematical model

The mathematical model of the whole rotor is the same we showed for the inboard design analysis. On the other hand, the outboard portion solution has been modelled in a fixed reference system. In both cases the turbulence models adopted are the Spalart-Allmaras and the κ–ω SST. Wall functions have been used for the whole rotor, while the smaller domain of the tip region case allowed to use a direct solution of the boundary layer flow. For further details we cross–refer to the previous sections.

5.2.2 The tip frame case

At first rotation has been neglected and the two investigated geometries have been studied at rest. For such introductory issue, the computational domain contains a small portion of the blade, from R = 19.4 to the end (R = 20.5). It is about 5% of the whole length, *i.e.* three times the local chord length. The chosen computational domain is shown in figure 5.7, where dimensions refer to che chord length at the bottom of the cut portion of blade (C = 0.545 m). In figure 5.8 the grid structure generated with Gambit ® is presented.

A *C-mesh* has been generated, and a refinement study has been carried out, resulting in increasing the volume number in the proximity of the walls. The total number of elements was $0.5 \cdot 10^6$. A sketch of the grid is visible in figure 5.9 and figure 5.10, together with a detail of the actual tip.

Boundary conditions are indicate in figure 5.10. The detailed description of the boundary conditions set-up at inlet is reported in Table 5.2: a uniform

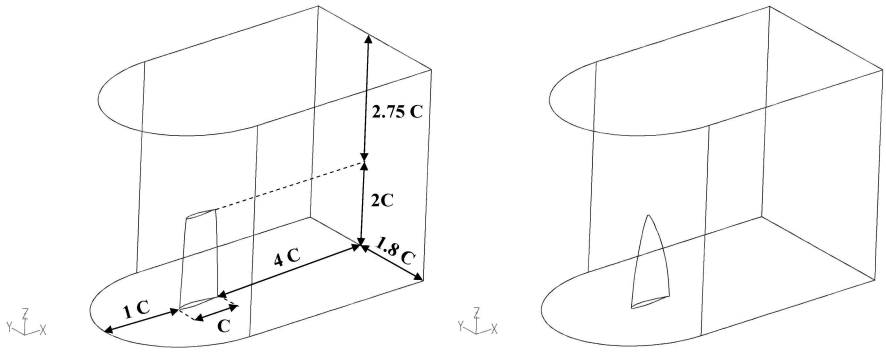

Figure 5.7: *Computational domain including the outboard portion of the blade*

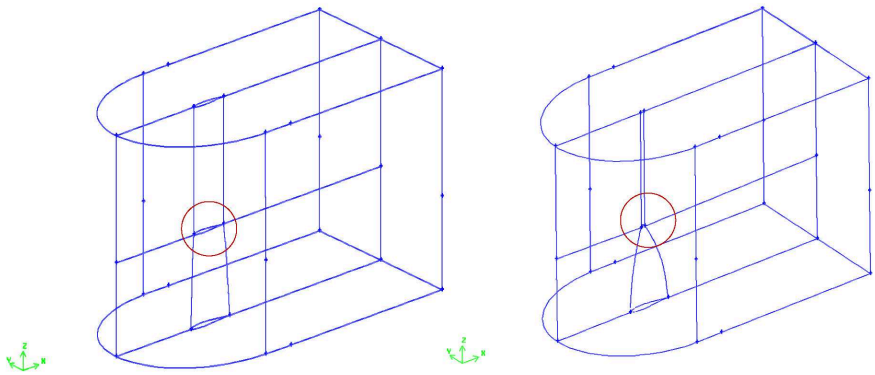

Figure 5.8: *Grid pattern generated with GAMBIT*

velocity value has been imposed for the front and lateral sides, estimated from the whole turbine operating regime. Turbulence parameter are taken from [41]

Results

Information about the aerodynamic loads have been collected. Two contributions can be identified, the pressure and the viscous stresses, which are reported in Table 5.3.

The tangential force (*i.e. driving* force, aligned with the $-x$ or chordwise direction, see Figure 5.10) results substantially unchanged between the two cases, while the tapered tip allows a reduction of the axial loads (the y-axis

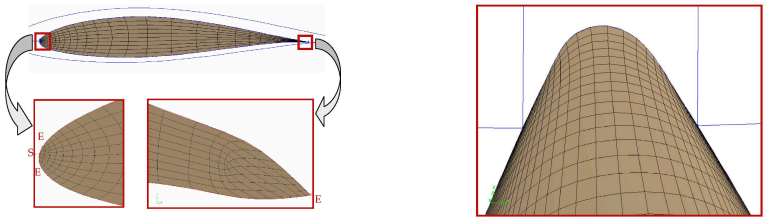

Rectangular tip blade *Tapered tip blade*

Figure 5.9: *Details of the mesh at the tip*

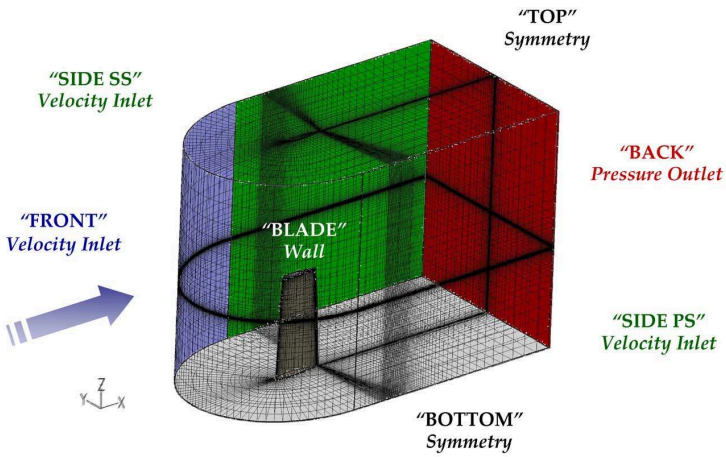

Figure 5.10: *Mesh and boundary conditions*

Table 5.2: *Boundary conditions at inlet for the fixed blade tip portion*

Tangential Velocity [m s^{-1}]	Axial Velocity [m s^{-1}]	Kin. Turb. Energy κ [m s^{-2}]	Turb. Diss. Rate $\Omega = \epsilon\kappa^{-1}$ [s^{-1}]
56.72	6.8	0.03	0.9375

Table 5.3: *Aerodynamic loads for the fixed blade tip portion*

	Axial force [N]			**Tangential force [N]**		
CASE	*Press.*	*Visc.*	*Total*	*Press.*	*Visc.*	*Total*
Rectangular	780.0	0.9	780.9	34.9	−9.9	25.0
Tapered	571.2	0.7	571.9	33.0	−7.3	25.7

in Figure 5.10). The tapered geometry allows the viscous tangential forces to decrease, due to a definitely minor surface (about 60% of the rectangular one). Thus, the relative smaller decrement of pressure forces, also along the tagential direction, is balanced.

The spanwise trend of axial loads has been plotted in figure 5.11. The values refer to the only pressure component and have been computed by dividing the tip blade in 11 portions of equal span (0.1 m). Aerodynamic loads are bigger outward for the rectangular tip blade and consequently circulation goes to zero more abruptly if compared to the tapered case. Therefore, tip vortex must be stronger and condensed, for its intensity is proportional to the radial derivative of the linear circulation about the blade.

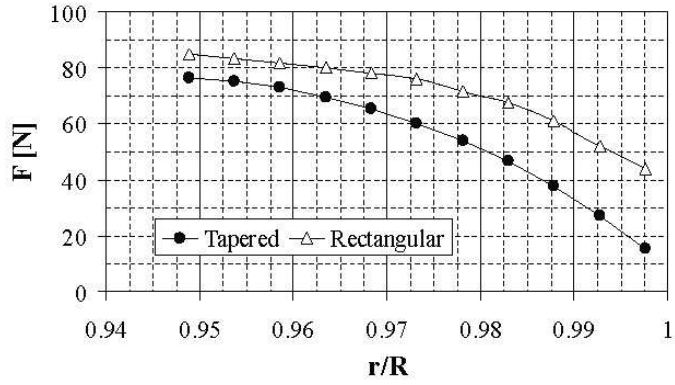

Figure 5.11: *Axial forces along the spanwise for the fixed blade tip case*

A qualitative representation of the relative path lines (figure 5.12), coloured with the vorticity intensity, gives a confirmation of the above considerations.

Furthermore, looking at the iso-velocity lines of the radial component (figure 5.13) is clearly visible that the rectangular tip experiences a stronger tip vortex, also more focused in the outward compared with the tapered tip blade. After the blade passage, opposite radial flows exist, which in the rectangular tip case double in magnitude the analogous spanwise component of the tapered case.

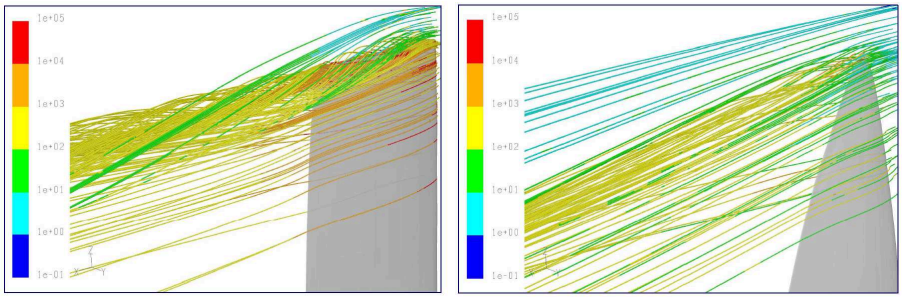

Rectangular tip blade *Tapered tip blade*

Figure 5.12: *Relative path lines coloured with the vorticity magnitude* [s^{-1}]*, for the fixed tip portion case*

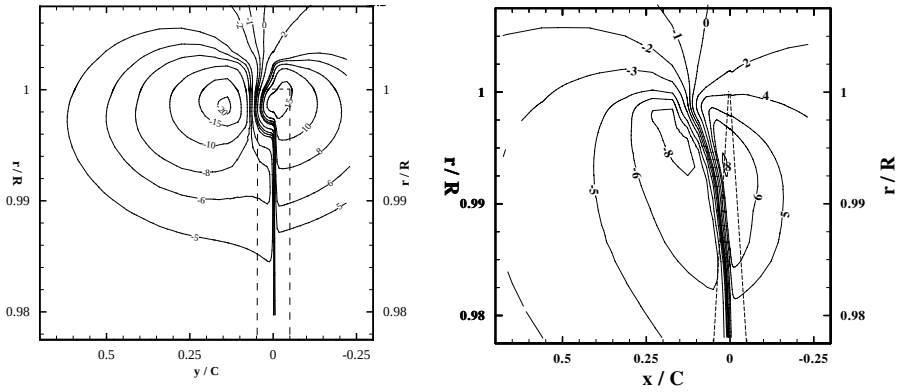

Rectangular tip blade *Tapered tip blade*

Figure 5.13: *Iso-velocity lines (m/s), radial component in a meridional plane located at the blade trailing edge*

5.2.3 The rotating blade case

In this section the study of the whole rotor case is described. The full–geometry HAWT, BEM–designed and shaped with rectangular tip has been already presented in Chapter 4. Respect to that study, the domain axial extension has been shortened to one diameter downstream (figure 5.14).

The detailed analysis of the flow concentrates on the design conditions, *i.e.* wind speed V_0= 6.8 m/s and 27.1 RPM. Alike a model of the full–rotor with a tapered tip blade has been then created. Only the tip portion (between r= 19.4 m and the end) of the blade changes within the two cases.

As the studied turbine blade is not identical to the inspiring LM19.1, but the

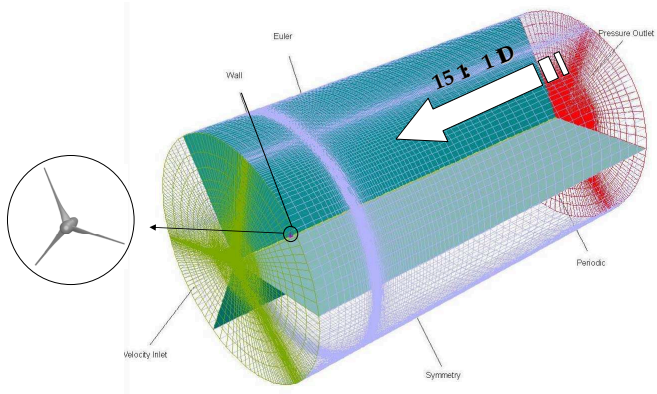

Figure 5.14: *Computational domain for the whole rotor case*

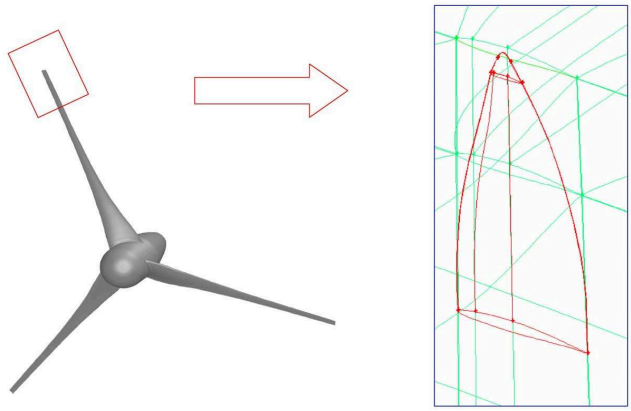

Figure 5.15: *Modification of the tip portion for the rotating blade*

BEM re-designed version, likewise the tip part has been shaped to resemble the typical modern turbine types (see figure 5.15), even though does not proceed exactly from one of them.

In both cases the total amount of computational volumes was $1.4 \cdot 10^6$. It should be retained that the validity of this study is for a comparative analysis of the two situations.

Table 5.4: *Mechanical power, power coefficient and thrust force for the full–rotor simulation*

CASE	**P [kW]**			C_P	**T [kN]**
	Press.	*Visc.*	*Total*		
Rectangular	127.7	−8.9	118.8	0.472	28.7
Tapered	126.6	−8.3	118.3	0.474	29.4

Results

First, it is possible a comparison of the yield mechanical power within the two rotor configurations (see Table 5.4. Keeping the same operating conditions, it is found that power holds substantially unchanged too. Looking back at the simplified study (Table 5.3), it is confirmed that a decrease of viscous stresses compensates the consistent reduction of pressure loads. It is otherwise obvious that the thrust is bigger for the rectangular tip blade rotor, due to the larger resistant surface.

From the contour plots of axial and radial velocity in a meridional plane section passing through the blade the differences can be seen of the flow field structures downstream of the rotor within the two studied tip geometries (see figure 5.16 and figure 5.17).

In Figure 5.18 the vorticity magnitude contours are plotted in a meridional cut 1 tip-chord downstream the blade, for the two tip geometries. The more intense tip vortex intensity at the rectangular tip respect to the tapered one qualitatively agrees with the fixed tip–portion study results.

5.2.4 Concluding remarks

The problem of studying the tip portion of a wind turbine blade by solving the flow field with the CFD is far to be an easy issue. In first instance, only the extreme outboard of the blade has been indeed considered, even at rest. Then the full rotor has been included in the simulations, by steady rotating. The analysis carried out gives the tools for evaluating the advantages of a tapered geometry for the tip blade and shows its capability for a more comprehensive blade design optimization study.

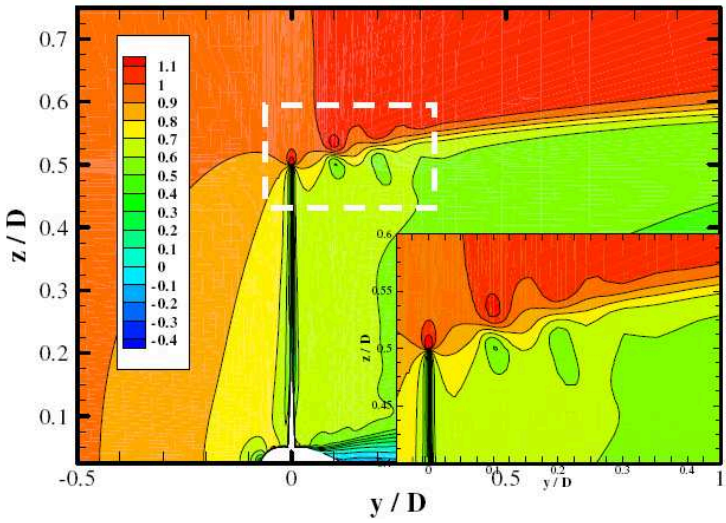

Rectangular tip blade

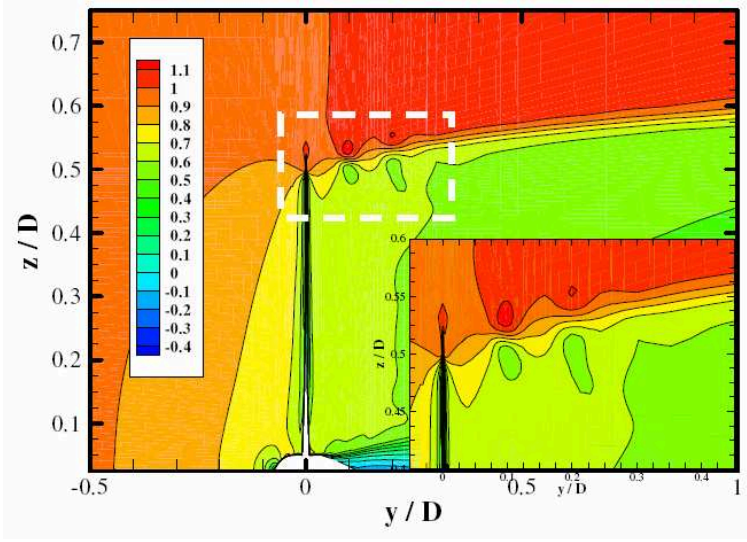

Tapered tip blade

Figure 5.16: *Iso-velocity contours, axial component* [m s^{-1}], *for the full–rotor case*

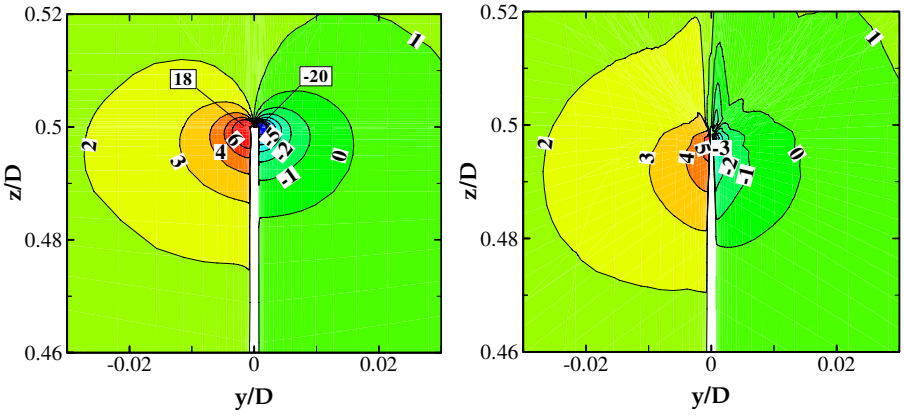

Rectangular tip blade *Tapered tip blade*

Figure 5.17: *Iso-velocity contours, radial component* [m s^{-1}], *for the full–rotor case*

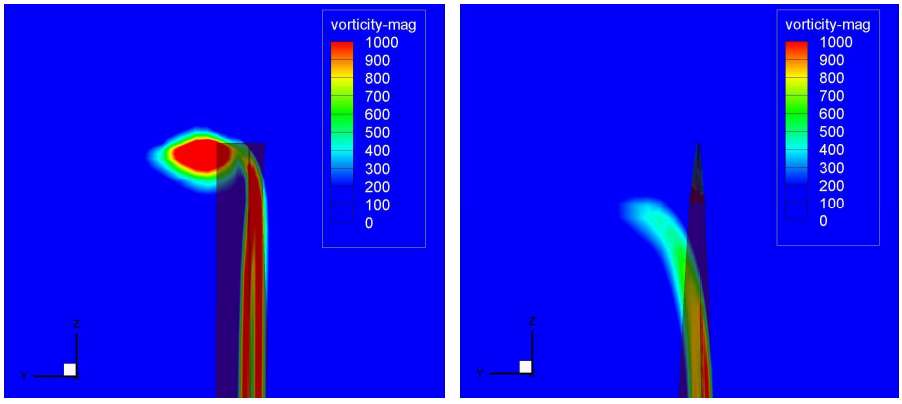

Rectangular tip blade *Tapered tip blade*

Figure 5.18: *Contours of vorticity magnitude* [$1/s$], *for the full–rotor case, meridional plane 1 tip-chord downstream of the blade*

Chapter 6

Wakes study

6.1 Introduction

Even if the contents of this thesis is mainly directed to the physics of the power extraction by wind turbines, a preliminary study of both the *near* and the *far wake* region has been likewise conducted. Indeed, between , between other factors, efficiency of wind farms is strictly tied to the relative positioning of wind turbines and to the presence of orographic obstacles. As in most of the engineering problems, two main targets exist but opposed. On one hand, we would avoid wake effects by putting the wind turbines far away from obstacles and other turbines. On the other hand, due also to the lack of available sites (at least for complying with all the environmental restrictions), it is necessary to place the machines as close as we can.

One of the goal is therefore to find a balance between this opposed needs, by quantitatively estimating wake effects. It is clear the handiness of CFD for the scope, being the wake aerodynamics particularly hard to face with experimental techniques.

Moreover, since wind turbine located in wind farms are subject to the unsteady wake flow of the upstream turbines, they are also affected by strongly fatigue loadings and not only by power losses.

Thus, the manufacturers consider an higher level of turbulence intensity while designing wind turbines, with regards to wake effects. Nevertheless, this is not completely sufficient while accounting for the complex wake dynamics.

As it is for other aspects of the wind turbine functioning, wake aerodynamics is only apparently a simple matter.

- Wind blows randomly, regarding both intensity and direction, and turbulence is dominant as well within the Atmospheric Boundary Layer.

- Wakes interact when positioning the turbines in clusters.

- Both stall-regulated machines and modern wind turbine experience deep stall for high wind speeds.

For all this reasons wake description is complicate. Even though, wind turbine wakes have been a topic of research from the early start of the renewed interest in wind energy utilisation in the late 1970s [6].

A complete survey of the literature on the wind turbine wake analysis is given in [7].

Some experimental work has been carried out in the past years, both in wind tunnel with scaled models as well as in real operating conditions. Nevertheless, most of them simply concluded by realizing how hard is addressing the problem with measurements. In general most of the experiments are wind tunnel campaigns, so that an effect of scaling on the representation of real world is always found (in most of the cases the Reynolds number too is lower). On the other hand, full-scale field experiments have the drawback of random operating conditions (*e.g.* wind shear, turbulence, unsteadiness, etc.).

The most reliable source regarding wind turbine experiments is the NREL Unsteady Aerodynamic Experiment carried out in the NASA Ames wind tunnel [37]. The focus of those measurements was put on the pressure and force distributions along the blade and hardly any wake measurements were performed. A similar project has been more recently completed, *i.e.* the famous "MEXICO" (*Model rotor EXperiments In COntrolled COnditions*), and data are currently given for the studied three-bladed rotor model of 4.5 m diameter, tested in the DNW wind tunnel [43].

It is CFD that in the last decades has become the favourite approach for the wake analysis.

At TÜV-Nord in 2002, Hahm and Kröning [44] used the code Fluent to predict the wakes behaviour. The whole turbine was modelled (*i.e.* the three-bladed rotor and the tower), and the terrain was also included into the model. A multiple reference frames model was used to account for the rotation of the blades, while terrain and tower rest. Also Ruith *et al.* [45] predicted the wake of a cluster of five small wind turbines (*i.e.* the Grumman Wind Stream 33) by adding a virtual blade model (VBM) via UDF to Fluent, in order to keep the computational mesh manageable (less than 2 million cells were used). Several numerical studies, among those already mentioned in the previous chapters, deal also with wakes (see *e.g.* [6][9][15]). Finally, the combined AL-LES method adopted by Troldborg *et al.* [46] represents the last tendency in approaching wake dynamics. The promising LES techniques are successfully used for capturing the strong unsteadiness of the wake field, while their high computational needs are balanced by adopting a "simple" actuator line for the blade loadings.

6.2 Wind turbine wakes

The air that passes through the cross-section of a wind turbine rotor exerts a torque on the rotor shaft, and an equal and opposite torque is imposed upon

the flow stream by the rotating blades. Consequently, downstream of the rotor the air flow must rotate in a direction opposite to that of the rotor. The angular momentum is thus increased in the wake, so that each air particle has a tangential velocity component as an axial one, instead of flowing merely streamwise.

In the basic Momentum theory, the air that passes through the disc undergoes an overall change in velocity and a rate of change in momentum, which corresponds to a force. The force causing the change of momentum comes from the pressure difference among the rotor disc, whereas outside the stream-tube the pressure is atmospheric. According to this simple approach, the pressure drop can be determined by applying the Bernoulli's equation to the upstream and downstream sections of the stream-tube.

When introducing the wake rotation, the tangential component of the rotor wake flow produces an increase of its kinetic energy which has to be compensated for by an additional fall in the static pressure to that of the one-dimensional theory [8]

$$\delta p_r = \frac{1}{2}\rho \left(2\Omega a' r\right)^2 \tag{6.1}$$

A measure of that phenomenon, which takes place abruptly across the rotor, is the tangential induction factor a', which is zero upstream of the rotor, where the flow is assumed not to rotate , whereas is different from zero immediately downstream, due to the tangential equal to $2\Omega r a'$. The values of a and a' that maximize the power coefficient are [8]

$$\begin{cases} a = 1/3 \\ a' = \frac{a(1-a)}{\lambda^2 \mu^2} \end{cases} \tag{6.2}$$

The axial flow induction for maximum power extraction is the same as for the non-rotating wake case, and is uniform over the entire disc. On the other hand a' varies with radial position. The tangential velocity increases with decreasing radius because a' increases according with equation 6.2, and so the pressure decreases creating a radial pressure gradient. The radial pressure gradient balances the centrifugal force on the rotating fluid. The pressure drop across the disc caused by the rate of change of axial momentum as mentioned before is thus additional to the pressure drop associated with the rotation of the wake and is uniform over the whole disc. The usable part of the wind's total available energy is therefore reduced: in the extended momentum theory power coefficient must be smaller than in the simple momentum theory.

On the other hand, the rotational pressure drop would not contribute to the change of axial momentum if the wake did not expand. Actually the wake does expand. The inclusion of flow expansion and wake rotation in a fully integrated momentum theory shows that the axial induced velocity in the developed wake is greater than $2a$ but the effect is only significant at tip speed ratios *lambda* less than about 1.5, which is probably outside of the operating range for most

modern wind turbines. However, it is demonstrated that the kinetic energy of wake rotation is accounted for by reduced static pressure in the wake.

It is of interest to know the turbulence characteristics in wind farms in order to predict the mechanical loads on the wind turbines and their performances, and to evaluate the velocity deficit created in the wind stream by the drag of the turbines.

A distinct division can be made into *near* and *far wake* region.

- The *near wake* is taken as the region just behind the rotor, where the properties of the rotor flow can be noticeably discriminated, roughly up to one rotor diameter downstream. In this region the presence of the rotor is visible because of the aerodynamic perturbation created by the blades, including stalled flow, 3–D effects and tip vortices. The near wake survey is focused on the physical process of energy conversion.

- Otherwise, the *far wake* is the region beyond the near wake, where the focus is put on the mutual influence of wind turbines in farm situations. The main research interest is to study how the far wake decays downstream, in order to estimate the effects produced on the downstream turbines, *i.e.* lower velocity and higher turbulence intensity, which make the power production decrease and the unsteady loads increase.

6.3 Methods

The purpose of investigating the wake was included in this project since its early phase.

Even the first analysis, described in Chapter 4, deals with the wake issues and some of the results presented referred to the near wake development.

- The mathematical method, the computational domain and the discretisation grid that were used for that part of the thesis are the same utilized for the first wake study, which will be reffered as *CASE-01* (see Figure 4.4). The geometry studied was the BEM re-designed LM19.1 blade.

- However, the first domain was short and narrow with regards to the wake development and the external boundaries influenced the solution. A boundary condition sensibility study was performed in order to verify how relevant those influences can be. Different shapes and greater and greater size both axially and radially directed were tested. Finally, a substantially different domain has been chosen. Such last pattern is sketched in Figure 6.1 and will be referred as *CASE-02*. It has a axial length 17.5 times the rotor diameter ($2.5\,D$ upstream and $15\,D$ downstream) and the radial span is $5\,D$. Moreover, a small inner cylindrical surface, axial centred, has been introduced as additional boundary. In this way the axial region, more difficult to mesh, is totally removed and an Euler-slip condition has been imposed for the internal surface.

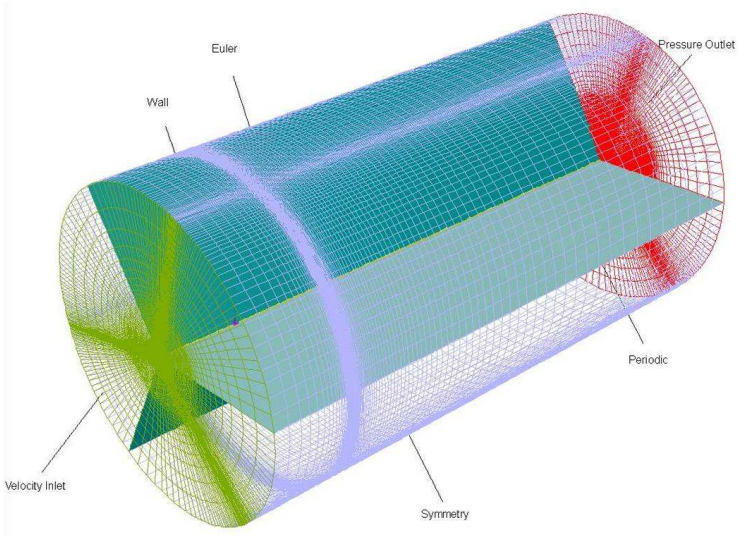

Figure 6.1: *Computational domain and boundary conditions (CASE-02)*

- The NREL Phase VI turbine model has been also included in the wake analysis as *CASE-03*. The model turbine is a small two blade machine, so rather different to the other turbine model, and has been widely described in Chapter 4, where are summarized also the characteristics of the computational domain. The mesh has been highly refined for a direct resolution of the boundary layer, as required by the study on the rotational effects at which this model was aimed. Moreover, CASE-03 refers to unsteady computations, and this is preferable when dealing with wake dynamics.

Both CASE-01 and CASE-02 refers to a freestream wind speed of 6.8 m/s, which is the nominal speed for the BEM-modified LM19.1. Since wind turbulence intensity and length scales are key-important parameters together with field geometry particular care was taken for inlet BCs. A turbulence intensity of 10% and a 1 m length scale were chosen in the presented cases. For CASE-03 the considered freestream speed have been 5 m/s and 7 m/s and a 1% turbulence intensity was set at the inlet, the blade was zero-pitched and rotated at a constant angular speed of 72 RPM.

6.4 Results

In the following some representative numerical results that characterize the aerodynamics of HAWT wakes are presented.

A visual depiction of the wake development past the rotor blades of a wind

turbine is given by the vorticity field (with the vorticity ζ defined as $\nabla \times \vec{v}$). In Figure 6.3 a surface of constant vorticity magnitude for *CASE-01* is reported. The plot shows how the tip and root vortices moves downstream. Since the blade tip follows a circular orbit but under a freestream axial-directed wind, a trailing vortex of helical path is shed downstream. In the near wake the shed tip vortices appear first as distinct vortex tubes and then merge into a continuous vortex sheet at a short distance from the rotor plane (Figure 6.2). At the blade root a counter-rotating central vortex is also shed downstream, but slower because the radial circulation gradient is normally lower than at the tip. It is the sign of the radial circulation gradient that determines the sense of rotation of the vortex behind the blade, at it is opposite at the tip and root blade. The vorticity field structure follows hence the classical signature, derived from merely theoretical considerations (Figure 6.3) [47]. Experimental results show that the spiral pattern is maintained at a distance from the rotor longer than that found by CFD [6]. Future works will be addressed to show the importance of Reynolds number and grid resolution, in order to achieve a better resolution of this feature.

Tip vortices are again visible in the axial velocity contour plot of Figure 6.4, where the velocity distributions (solid lines), mass-averaged along the pitchwise direction, are also depicted for different axial positions. The plot allows to evaluate the wake expansion, and moving from the internal to the external region the figure shows strong gradients in the interface between the wake and the undisturbed region. These gradients identify the position of the trailing vortex shed from the tip. Between the wake core and the tip vortex path a low speed region, which gives the characteristic shape (see *e.g.* [6] [38]), is barely recognisable only in the near wake and smoothed (the first black line). Moving downstream the velocity deficit curve is smoothed, perhaps because of the axially coarse mesh so that the improvements indicated regarding the previous figure are confirmed. Even though, the general distribution of the axial velocity is fairly correct.

Axial velocity contours can be used also to identify the transition from the near wake to the far wake. In Figure 6.5 the axial velocity component is plotted on radial cut at different position within the wake. Close to the rotor the presence of each blade perturbations is clear, as well as at each tip the trailing vortex path is recognisable. Moving downstream, the wake becomes a pitchwise uniform field, which gradually expands. The low-speed wake core is also expanding, while the boundary between the undisturbed flow and the wake field is marked by a strong velocity gradient, which corresponds to a uniform vortex curtain in lieu of the tip trailing vortex.

The velocity distributions in the far wake are predicted for *CASE-02*. In the contour plot of Figure 6.6 velocity distributions (solid lines) are shown, for different axial positions, as for the near wake. The axial velocity gradually grows up to the freestream value, so that at the domain outlet the deficit is about 10-20%. The wake field boundary shows now a smoother gradient and the far wake is dominated by diffusion phenomena, so that the wake is

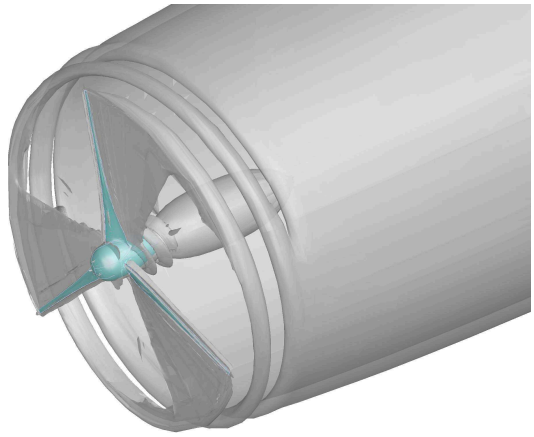

Figure 6.2: *Iso-surface of computed vorticity* $\xi = \left|\nabla \times \vec{U}\right| = 1\ s^{-1}$, *at* $U_0 = 6.8\ m/s$ *(CASE-01)*

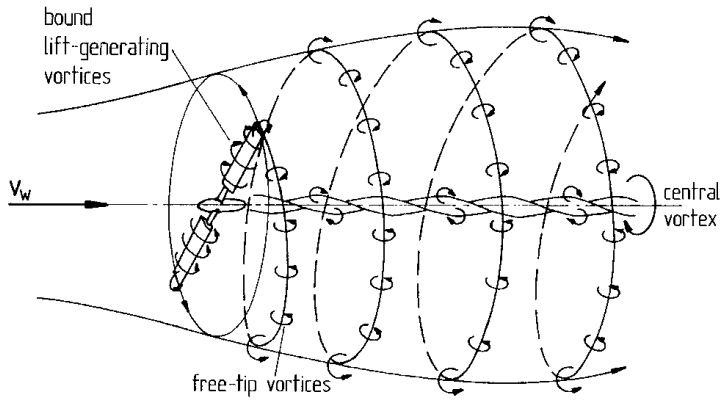

Figure 6.3: *Theoretical scheme of vortex structure [47]*

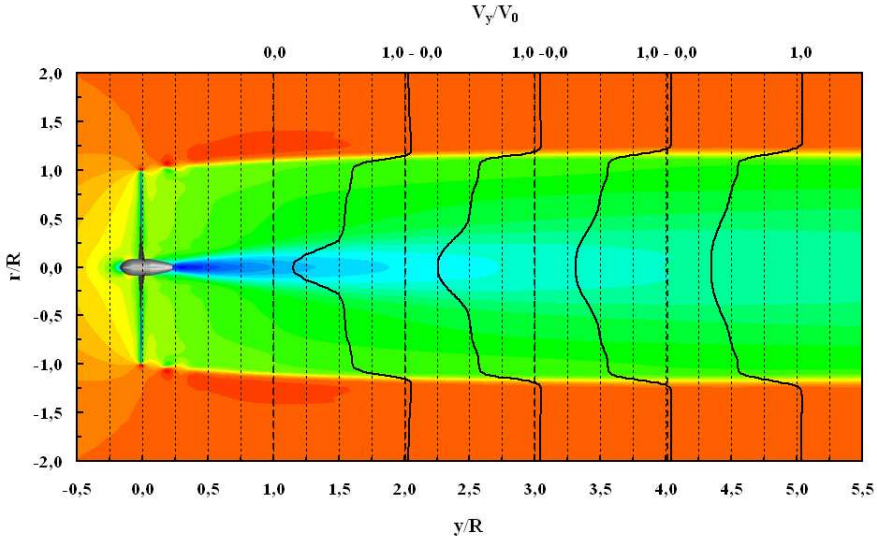

Figure 6.4: *Near wake axial velocity distributions, at $U_0 = 6.8$ m/s (CASE-01)*

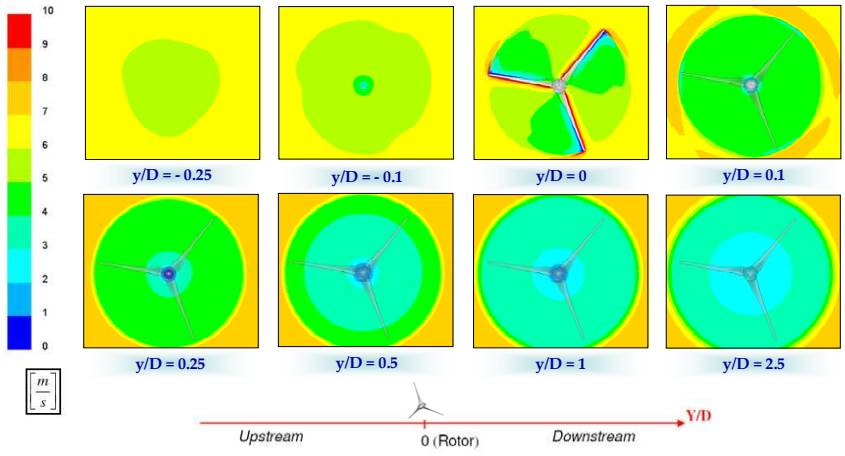

Figure 6.5: *Contour of axial vorticity in wake sections, at $U_0 = 6.8$ m/s (CASE-01)*

forced by the external flow. Nevertheless, turbulence intensity was found not to decade. With both the SA and the k-ω SST models, after a first decrease in the turbulent properties values, they keep increasing all along the domain.

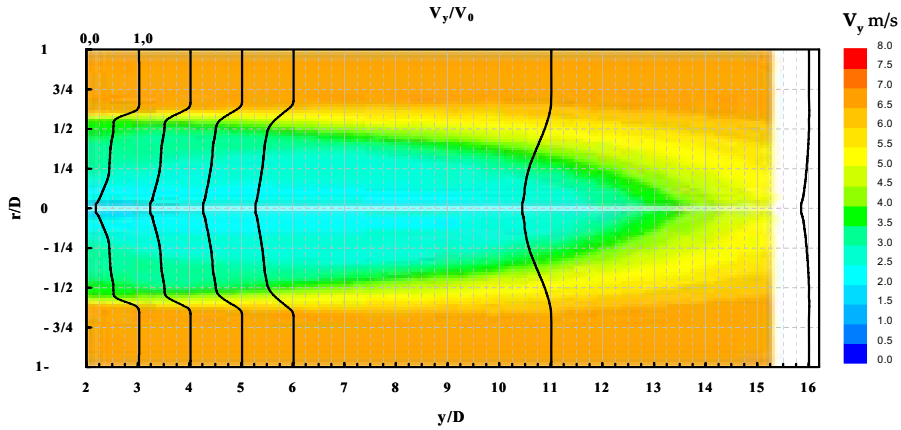

Figure 6.6: *Far wake axial distribution, at $U_0 = 6.8$ m/s (CASE-02)*

Finally, the contour plots of the non-dimensional axial velocity component are computed for CASE-03, at 5 m/s and 7 m/s freestream speed. In Figure 6.7 a representation of the whole domain and a close-up on the blade are shown. Unsteady computations were run, and this is favourable for predicting such dynamic phenomena. This, together with the fine mesh adopted in CASE-03, allows to better predict some wake features that were hardly captured by the previous cases. For instance, it is clearly visible in the 5 m/s case the presence of the low-speed region between the tip trailing vortex and the wake core, coloured in cyan. At the higher freestream wind, this decelerated area almost disappears. The wake expansion is more pronounced as the wind speed increases, even if more gradual too, whereas the 5 m/s case shows a sudden growth, as it is visible from the close-up, but then the span is kept almost constant. The tip vortex position, as well as its merging into a continuous trailing sheet, depends on the rotational frequency, the number of blades and the freestream speed. Here the blades are two, and this means two passages per each rotor revolution instead of three. But the rotational speed is almost three times that of the CAS-01 and 02. So, considering that the freestream speed are comparable (more for the 7 m/s case), the distance between the trailing vortex passages is right comparable. Likewise, as the wind speed decreases (in the 5 m/s case) the trailing paths get also closer, and one more single vortex-print appears, before they merge together.

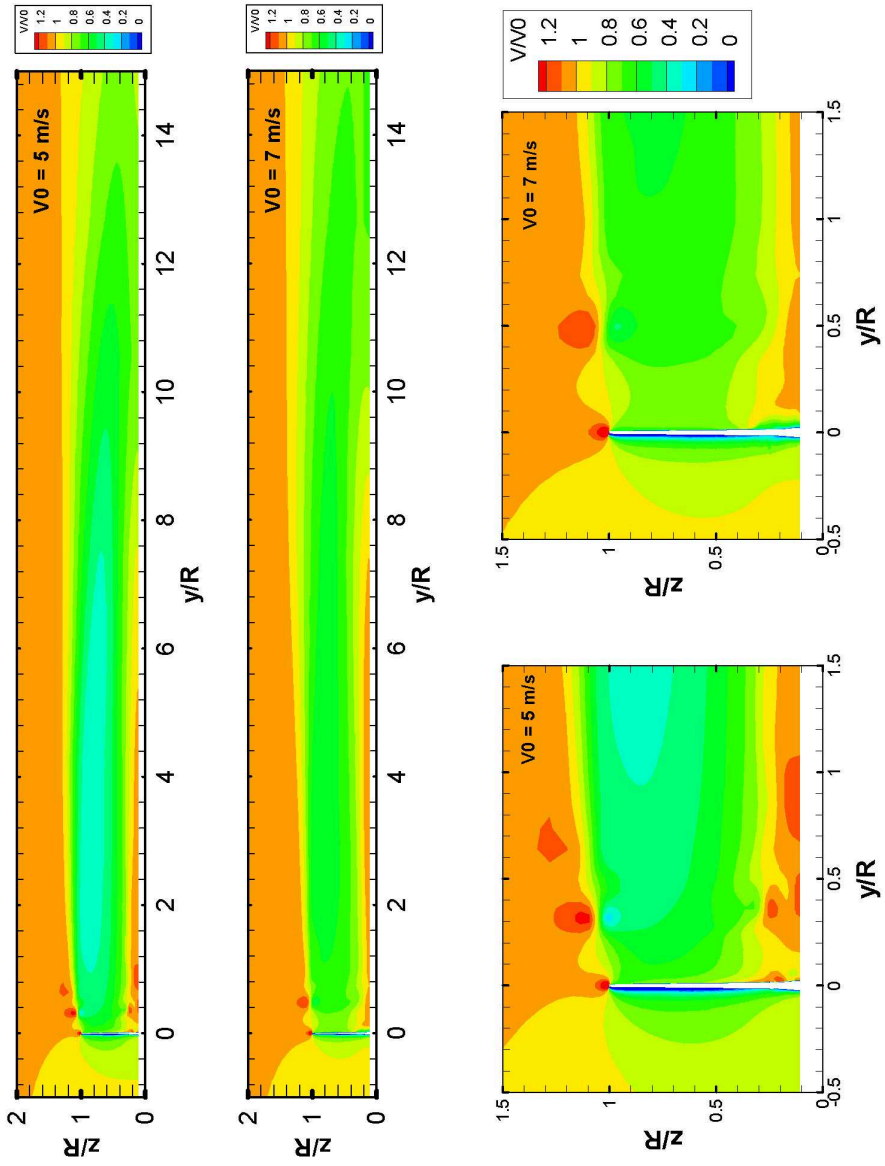

Figure 6.7: *Contours of non-dimensional axial velocity V/V_0 in the meridional blade plane, at V_0 5 m/s and 7 m/s for the NREL turbine (CASE-03)*

6.5 Concluding remarks

As we expected, we must conclude a real challenge the complete discovering of wind turbine wake aerodynamics by CFD-RANS. It might be also said that our approach was probably not the most effective one to solve the problem, especially if compared with the very recent techniques appeared in the last years in the literature. Moreover, significant effects on the wake structures play the presence of the tower and the terrain, which have neglected here for the sake of simplicity.

Anyhow, according with [6] full Navier-Stokes simulations can be regarded as the most important predictive tool for understanding aerodynamics of modern wind turbines. However, a DES or LES approach is rather preferable for solving the wake phenomena [7], where sometimes especially in the far wake *simpler* (for instance vortex methods) methods still perform better.

Chapter 7

Rotational effects

7.1 Introduction and literature review

Wind turbine blades are strongly affected by rotational and 3–D flow effects and they often operate in deep stall. Nevertheless, the actual design approach is typically based on employing the blade–element momentum–theory (BEM), with lift and drag forces determined from 2–D measurements. The results obtained are reasonable accurate in the proximity of the design point, but in stalled condition the BEM is known to underpredict the forces acting on the blades, as shown in the literature (see, *e.g.* [48]). Furthermore, the accurate prediction of rotor loads even in stalled conditions is of great importance for sizing the generator and other mechanical components.

The radial flow component present in the bottom of separated boundary layers of rotating wings is the reason of altered lift and drag characteristics of the individual blade sections with respect to the 2–D airfoils [49]. Two main contributions are commonly indicated for the rise of those phenomena, but the discussion about them is still open. One is Coriolis force, which acts in the chordwise direction as a favourable pressure gradient that tends to delay separation. On the other hand, centrifugal forces produce a spanwise pumping effect, resulting mainly in boundary layer thinning.

The present work aims at giving a better understanding of the main influence of rotational effects on the boundary layer that develops over wind turbine blades.

In 1945 Himmelskamp [50] first described through measurements the 3–D and rotational effects on the boundary layer a rotating propeller, finding lift coefficients much higher moving toward the rotational axis (Figure 7.1). Further experimental studies confirmed these early results, indicating in stall–delay and post–stalled higher lift coefficient values the main effects of rotation on wings. Measurements on wind turbine blades were performed by Ronsten [51], showing the differences between rotating and non–rotating pressure coefficients and aerodynamic loads and by Tangler and Kocurek [52], who combined results

from measurements with the classical BEM method to properly compute lift and drag coefficients and the rotor power in stalled conditions.

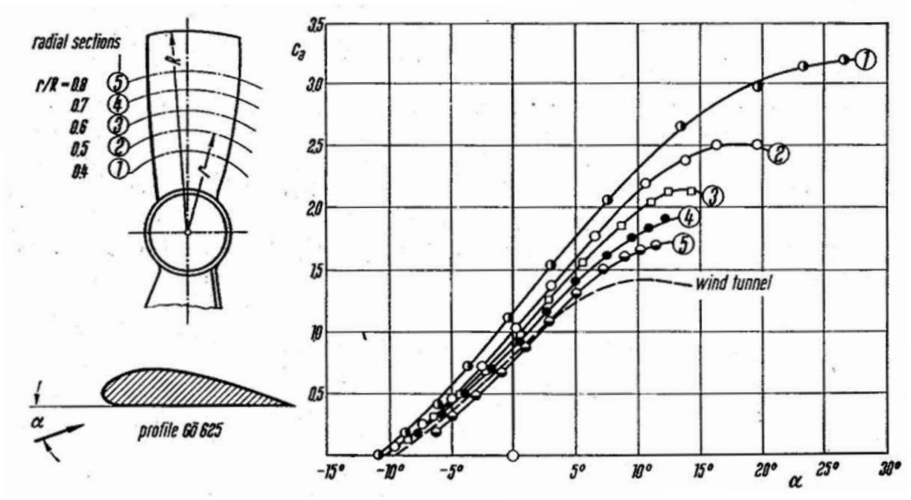

Figure 7.1: *Lift coefficients at various radial sections on a rotating propeller, measured by Himmelskamp in 1945 [53]*

The theoretical foundations for the analysis of the rotational effects on rotating blades come to the late 40's, with Sears [54], who derived a set of equations for the potential flow field around a cylindrical blade of infinite span in pure rotation. He stated that the spanwise component of velocity is dependent only upon the potential flow and it is independent of the span (the so–called *independence principle*). Then, Fogarty and Sears [55] extended the former study to the potential flow around a rotating and advancing blade. They confirmed that, for a cylindrical blade advancing like a propeller, the tangential and axial velocity components are the same as in the 2–D motion at the local relative speed and incidence. A more comprehensive work was made once more by Fogarty [56], consisting of numerical computations on the laminar boundary layer of a rotating plate and blade with thickness. Here he showed that the separation line is unaffected by rotation and that the spanwise velocities in the boundary layer appeared small compared to the chordwise, and no large effects of rotation were observed, in contrast to [50]. A theoretical analysis was done by Banks and Gadd [57], focussed on demonstrating how rotation delays laminar separation. They found that the separation point is postponed due to rotation, and for extreme inboard stations the boundary layer is completely stabilized against separation. In the NASA report done by McCroskey and Dwyer [58], the so-called secondary effects in the laminar incompressible boundary layer of propeller and helicopter rotor blades are widely studied, by means of a combined numerical and analytical approach. They showed that

approaching the rotational axis, the Coriolis force in the crossflow direction becomes more important. On the other hand the centrifugal pumping effect is much weaker than generally was supposed before, but its contribution increases as the magnitude of the adverse pressure gradient increases.

The last two decades have known the rising of computational fluid dynamic and the study of the boundary layer on rotating blades has often been carried on through a numerical approach. Twenty years ago, Sørensen [59] numerically solved the 3–D equations of the boundary layer on a rotating surface, using a viscous–inviscid interaction model. In his results the position of the separation line still appears the same as for 2–D predictions, but where separations are more pronounced a larger difference between the lift coefficient calculated for the 2–D and 3–D case is noticed. A quasi 3–D approach, based on the viscous–inviscid interaction method, was introduced by Snel *et al.* [48] and results were compared with measurements. They proposed a semi–empirical law for the correction of the 2–D lift curve, identifying the local chord to radii (c/r) ratio of the blade section as the main parameter of influence. This result has been confirmed by Shen and Sørensen [60] and by Chaviaropoulos and Hansen [61], who performed airfoil computations applying a quasi 3–D Navier–Stokes model, based on the streamfunction–vorticity formulation. Du and Selig [62] approached the problem solving the 3–D incompressible steady boundary layer equations. Their analysis stated that the stall delay depends slightly on the pressure effect and mainly on the acceleration of the boundary layer flow, *i.e.* on the Coriolis forces. Both rotational effects become smaller going outward according with [60] and [61]. Hu and co–workers [63] carried out a study of the stall–delay for wind turbines by means of boundary layer analysis, full N–S computations and wind tunnel experiments. The boundary layer analysis resulted in an extension of the work by Snel *et al.* [48]; for the full N–S computation the commercial code Fluent has been used, modelling the geometry accordingly to the experimental set–up.

3–D correction of 2–D airfoils characteristics has been made by Lindenburg [64], taking the local tip speed ratio into account and introducing a drag force correction, and by Bak *et al.* [65], using the different pressure distributions of rotating and non-rotating airfoils. Both of these papers present a comparison with experimental data.

7.2 The CFD-RANS approach

Making use of the CFD code Fluent, the governing equations for the viscous incompressible 3–D flow field around a rotating blade of a wind turbine have been solved, considering a non–inertial reference system moving with the rotor. 3–D and 2–D turbulent flow simulations were performed, with different angles of attack. The rotational speed is constant for all the computations, $\Omega = 3$ rad/s. A constant–chord, non–twisted and zero–pitched blade (to whom we will refer as *cylindrical blade*) was used and a non–uniform incoming flow was considered

(Figure 7.2). The geometric angle of attack is kept constant along the span by specifying the axial flow component as $(\Omega z)/V(z) = const$, where z is the radial coordinate and Ω the rotational speed. The idea is to build a database of different flow conditions, varying angle of attack, Reynolds number and radial position. In order to analyse the output data, an ad-hoc post-processing tool has been developed, allowing the evaluation within the computational domain of all the terms in a modified form of the Prandtl's boundary layer equation.

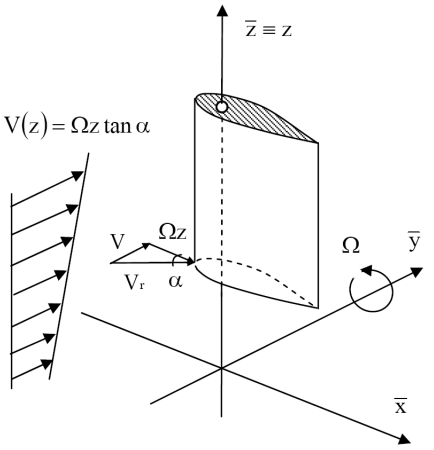

Figure 7.2: *Incoming wind velocity profile.*

7.2.1 Mathematical model

Consider a blade section performing a steadily rotating motion. Two different reference systems are now introduced. One is a global reference system attached with the blade and moving with that. The second one is a local reference system, still fixed with the blade, but aligned point by point with the local tangential and normal directions of the blade surface (Figure 7.3). In the first system the steady incompressible time–averaged Navier–Stokes equations (see *e.g.* [22]) for a rotating frame of reference are defined and numerically solved

$$\nabla \cdot \vec{V_r} = 0 \tag{7.1}$$

$$\nabla \cdot (\vec{V_r}\vec{V_r}) + 2\vec{\Omega} \times \vec{V_r} + \vec{\Omega} \times \vec{\Omega} \times \vec{r} = -\frac{1}{\rho}\nabla p + \nabla \cdot \bar{\bar{\tau}} + \vec{f} \tag{7.2}$$

where we have: the relative velocity vector $\vec{V_r}$, the rotational speed $\vec{\Omega}$, the fluid density ρ, the stress tensor τ

$$\bar{\bar{\tau}} = \nu \left(\nabla \vec{V} + \nabla \vec{V}^T \right) \tag{7.3}$$

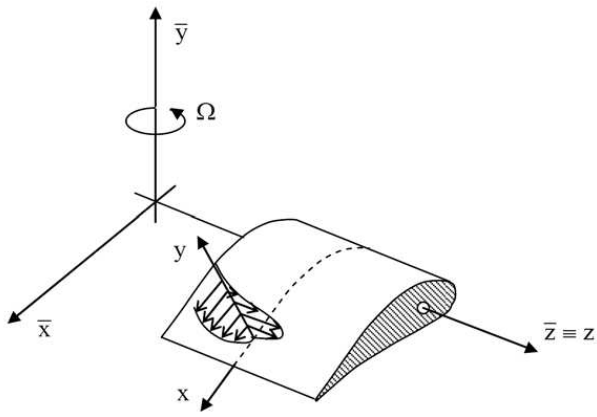

Figure 7.3: *Reference systems of coordinates, global* $(\bar{x}, \bar{y}, \bar{z})$ *and local* (x, y, z).

and the external body–forces $\vec{f}$. Let us identify then the Coriolis force term $2\vec{\Omega} \times \vec{V_r}$ and the centrifugal force term $\vec{\Omega} \times \vec{\Omega} \times \vec{r}$.
The second reference system refers to the boundary layer equations, which will be recalled in the post–processing step.

The effect of Coriolis forces

When the motion is referred to axes which rotates steadily with the bulk of the fluid, the fictitious Coriolis and centrifugal forces must be supposed to act on the fluid (see [22], pp. 555-556). They are called fictitious forces because they are a by-product of measuring coordinates with respect to a rotating coordinate system. Both those contribution appear in equation 7.2. The Coriolis force tends to change the direction of the component of the local velocity vector in the plane normal to the rotational axis. The sense of this change of direction is opposite to that a point with coordinates fixed relative to the rotating axis experiences in an absolute frame. As shown in Figure 7.4, if the rotation in the plane normal to the rotational axis is clockwise, the Coriolis force tends to turn the local in-plane direction of motion to the left, even with respect to the rotating frame. It should be noticed that the relative distance of the fluid element considered to the rotational axis has no influence and that the Coriolis force is linear in the velocity.

7.2.2 Numerical model

All the computations have been performed using the finite–volume code Fluent 6.3 with a steady–RANS approach. One untwisted blade, consisting of a symmetric NACA 0018 airfoil with constant chord, has been modelled, by applying periodicity for the three–bladed rotor. The blade geometry has been

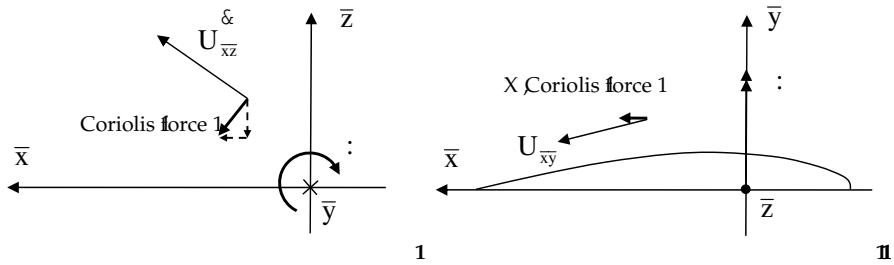

Figure 7.4: *To show the direction of the Coriolis force that acts in the rotating reference system of coordinates*

scaled using a constant chord length, $C = 1$ m. The radius is 2 C and 20 C, at the root and at the tip of the blade respectively. A computational domain enclosed by two cylinders has been chosen, with the blade starting at the inner cylinder and ending at the outer cylinder (Figure 7.5). The full axial extension of the domain is 2 times the rotor diameter and is centred on the blade. These proportions resulted from the best balance found between computational efforts and boundaries independence.

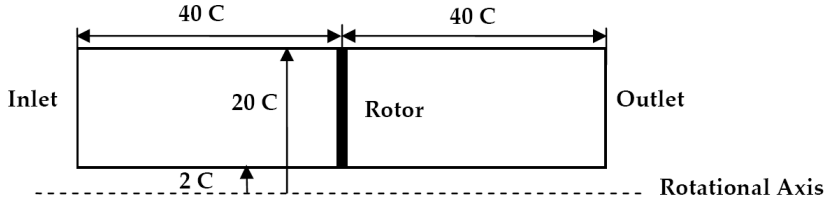

Figure 7.5: *Computational domain (C = chord length).*

The grid has been generated modularly with Gambit. It consists of a C–shaped region around the blade (Figure 7.6) blended with a cylindrical external block (Figure 7.7).

In the core, one counts 35 cells from the airfoil to a normal distance of approximately half–chord (with a first cell height of 10^{-5} chord length), 120 cells for each side of the profile and 45 cells along the spanwise direction. The boundary layer has been solved directly, with y^+ values limited between 1 and 3 and the κ–ω SST turbulence model by Menter has been used for turbulent computations. Regarding laminar/turbulent transition, since it is known how important is to include it to model the physics as close as possible [11][28], a low-Re correction was implemented [24] to damp the turbulent viscosity as the

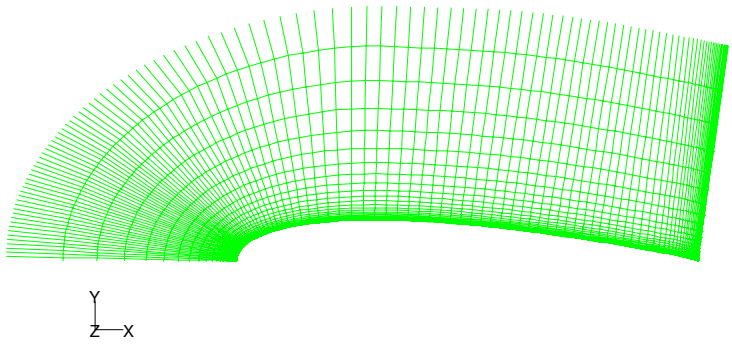

Figure 7.6: *C-mesh around NACA 0018 airfoil* ($120x35$)

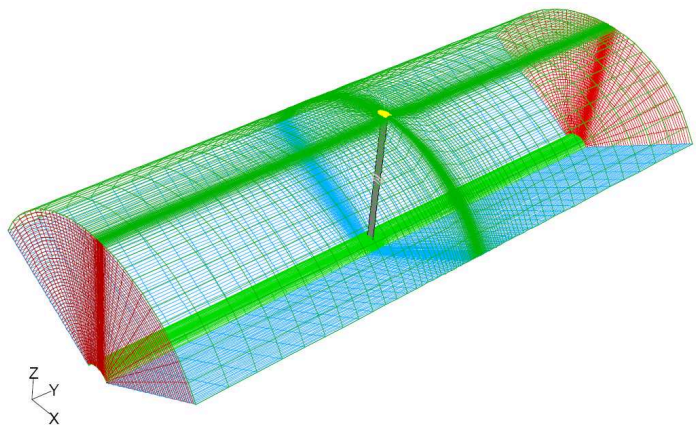

Figure 7.7: *Computational grid* ($0.9 \cdot 10^6$ *volumes*)

Reynolds number gets low.

Dirichlet for velocity at the inlet and Neumann for pressure at the outlet were imposed as consistent boundary conditions, while the inner and outer cylindrical surfaces have been regarded as Euler–slip walls. In the 3–D case the standard grid had about one million control volumes and a refinement study was made with a two millions cells grid. With the same set–up 2D computations have been performed, in order to show differences and analogies.

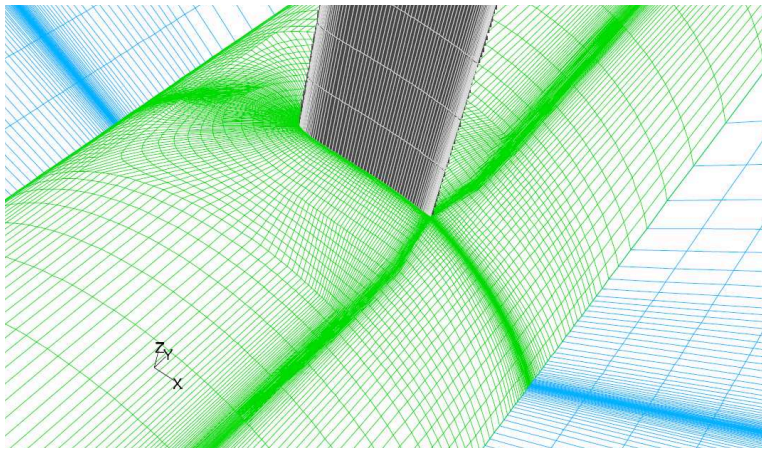

Figure 7.8: *Computational grid, detail of the blade root*

A fundamental problem is the determination of the actual angle of attack and the followed procedure is presented in the next paragraph.

7.2.3 Determination of 3–D angle of attack

The rotational effects could be studied and identified, by comparing the full 3–D rotating blade computations with the corresponding 2–D situations. Nevertheless, the flow conditions in the two cases must be carefully chosen, *i.e.* in a consistent manner. It is well known that the flow similarity property could be achieved if the Reynolds number is kept the same, but in the theory of wing sections another key–parameter has to be considered, *i.e.* the angle of attack. Angle of attack is a 2–D concept. It is defined as the geometrical angle between the relative flow direction and the chord of the airfoil. Consequently, finding an equivalent local angle of attack for 3–D flows is not trivial. For a rotating blade, for instance, the flow passing by a blade section is influenced by the bound circulation on the blade. Moreover, a further complication arises from the 3–D effects from tip and root vortices, neglected for the sake of simplicity in our model. Here, to determine the local angle of attack from the computed 3–D flow field two different techniques were considered. The first technique is the averaging technique suggested in [13] and then, slightly modified, employed in [36]. The second technique has been recently proposed by Shen *et al.* [66] as a method suitable for more general flow conditions and it is based on the determination of the local induced velocities created by bound vortices. After verifying the agreement between the outputs from the two strategies, the latter has been finally chosen for all further investigations. A more detailed insight into the angle-of-attack determination is included in Appendix B.

7.2.4 Postprocessing tool

In order to analyse the output data from the N–S code a code has been developed in Matlab environment, to evaluate the relative importance of the various terms in the boundary layer equations with respect to the arising of rotational effects.

The 3–D incompressible boundary layer equations for a steady rotating flow, based on the Prandtl's boundary layer equations (see [53]), read

$$\frac{\partial u}{\partial x}+\frac{\partial v}{\partial y}+\frac{\partial w}{\partial z}=0 \tag{7.4}$$

$$u\frac{\partial u}{\partial x}+v\frac{\partial u}{\partial y}+w\frac{\partial u}{\partial z}=-\frac{1}{\rho}\frac{\partial p}{\partial x}+2\Omega w\cos\theta+\Omega^2\overline{x}\cos\theta+\frac{\partial}{\partial y}\left(\nu\frac{\partial u}{\partial y}-\overline{u'v'}\right) \tag{7.5}$$

$$u\frac{\partial w}{\partial x}+v\frac{\partial w}{\partial y}+w\frac{\partial w}{\partial z}=-\frac{1}{\rho}\frac{\partial p}{\partial z}+2\Omega u\cos\theta+\Omega^2\overline{z}+\frac{\partial}{\partial y}\left(\nu\frac{\partial w}{\partial y}-\overline{v'w'}\right) \tag{7.6}$$

where (u, v, w) are the velocity components in directions (x, y, z), *i.e.* the axes of the local system of coordinates, and with theta defining the angle between the tangent to the airfoil and the $x - z$ plane.

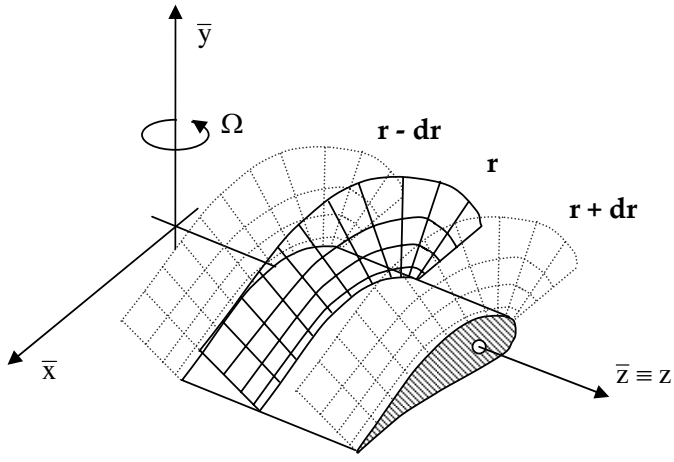

Figure 7.9: *Postprocessing sections of the computational domain*

The desired output variables are computed in some proper surfaces of constant radius, extended to a distance of half chord length from the blade wall Figure 7.9. The variables of interest are sorted in a new order, according to

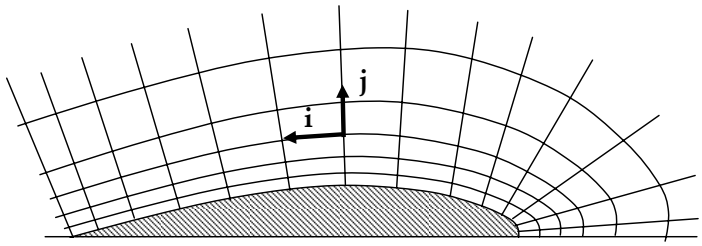

Figure 7.10: *Grid around the airfoil and new nodes indices*

the boundary layer tangential and normal directions (see local system of coordinates in Figure 7.3 and Figure 7.10).

The derivatives are estimated taking a 2^{nd} order CDS polynomial fitting of the output data for non–uniform spaced grids.

The boundary layer height is also found, by checking both the vorticity magnitude and the velocity gradient values, along the normal direction, as diagnostic methods. The last technique has been suggested by Stock and Haase [67]. A more detailed insight into the post-processing tool is included in Appendix B.

7.3 Results

7.3.1 Cylindrical blade

The present section reports the analysis of the computed flow solution, focussed on the general features of the flow field around rotating blades and aimed at showing the effects of rotation, on pressure coefficient distributions and integral aerodynamic coefficients. Further studies are required for stating more about the specific goal of our project, however a first glance into the post-processing phase is given. A number of different flow condition have been simulated and analysed, with geometric angles of attack ranging from 0 to 16 degrees. The effective values of local angle of attack for inboard sections can be higher than 20 degrees and a large portion of the blade suction side is dominated by separation phenomena (Figure 7.11). As expected, in the attached flow portion of the blade, the limiting pathlines are aligned with the main stream, so that they can be regarded as in a 2D-alike condition. This is true mainly for the outboard of the cylindrical blade, whose behaviour resembles there that of an ideal wing of infinite span. On the other hand, where separation dominates, *i.e.* in the blade inboard, the flow pattern evidences strong radial components. Within the deep stalled region, secondary flows become the most.

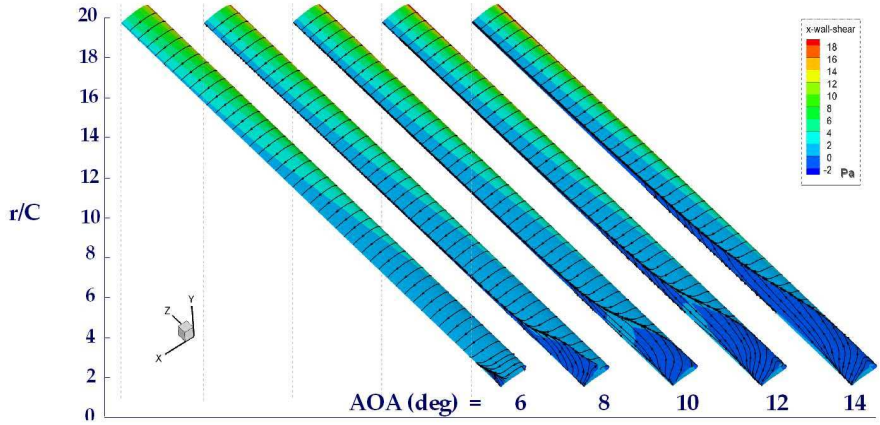

Figure 7.11: *Limiting streamlines on blade suction side for different geometric flow incidences.*

In the turbulent flow computations Reynolds number along the blade varies between $1 \cdot 10^6$ and $6 \cdot 10^6$ from root to tip. The radial stations chosen for the analysis are located at $r/R = 0.16$, 0.54 and 0.75. A detailed depiction of the boundary layer velocity profiles in a local coordinate system is available for different spanwise positions along the blade. The pure rotating blade, without inflow and with zero pitch angle, is presented as a reference case in laminar flow regime. The velocity profiles shape (Figure 7.12) looks physically correct

and the crossflow becomes important after separation, which in this case occurs near 80% of the chord length.

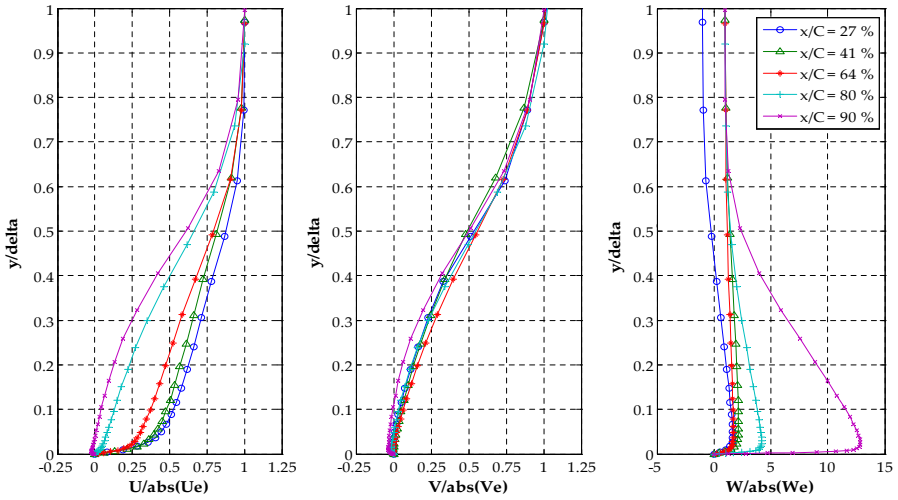

Figure 7.12: *Velocity profiles in the local coordinate system for different chordwise positions x/C, plotted against the non-dimensional boundary layer thickness y/δ and non-dimensionalised with the values at boundary layer edge (3–D, $r/R = 0.16$, $AOA = 13.4$ deg, $Re = 10^2$)*

In Figure 7.13 the in–plane streamlines around the rotating blade section and the corresponding pure 2–D airfoil are plotted, in a situation of deep stall. It is visible that the main effects of rotation are to stabilize vortex shedding and limit the growth of the separation cell. Moreover, the stagnation point moves downstream, and separation tends to approach the leading edge.

This is confirmed by Figure 7.14, where pressure coefficients evaluated with 3–D and 2–D simulations have been compared. Dealing with airfoils, the expression of the pressure coefficient is the 2.17. The stagnation point is therefore the negative peak, which is shifted toward the trailing edge in the rotating case in agreement with the streamlines pattern. After the upper "suction" peak, the 2D curve falls abruptly ,whereas the 3D trend is smoother. The distance between pressure and suction side, *i.e.* the area of the graph, looks considerably larger in the 3D rotating case. An higher lift must be expected in such a situation.

Further observations are stemmed from the static pressure and vorticity contours plotted in Figure 7.15 and Figure 7.16. Different radially spaced slices of the domain around the blade, have been considered. These planes are curved surfaces of constant radius (the value reads on the labels), covering a normal distance of 1 chord all around the blade wall. A unique colormap has been used, within the graphs. The higher is the distance from the axis

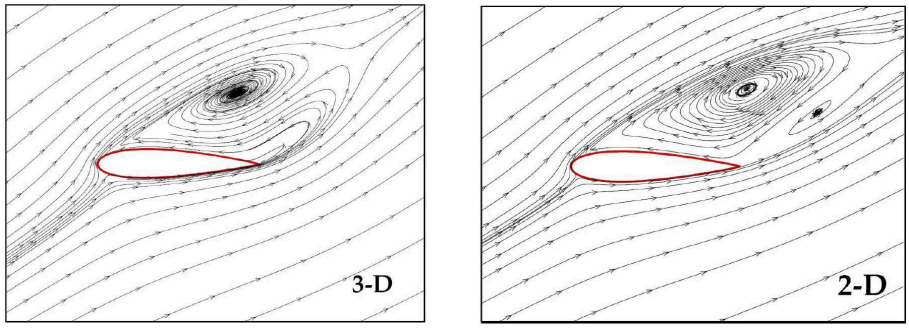

Figure 7.13: *Streamlines around the 3–D rotating blade section at* $r/R = 0.16$ *and the corresponding 2–D case with local incidence of* 26.9 *degrees and Reynolds number about* 10^6

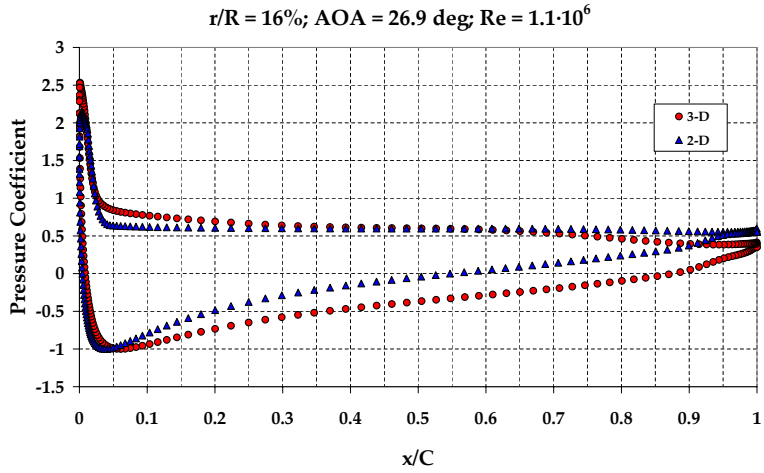

Figure 7.14: *Pressure coefficient distribution of the 3–D rotating blade section at* $r/R = 0.16$ *compared to the 2–D case (angle of attack = 26.9 degrees, Reynolds number =* 10^6*)*

of rotation, the greater are the extreme values within the pressure field. The outward sections operate with the lower angles of attack, much closer to the optimum value designed with such airfoil sections. Consequently, the suction is the strongest effect and none or only small separation occurs, leading to values of lift coefficient resembling the 2D ones.

The vorticity field is also meaningful (Figure 7.16). The blue colour that fills almost each entire slice is the potential field past the blade. Here vorticity cannot be different from zero. Despite the boundary layer is clearly visible

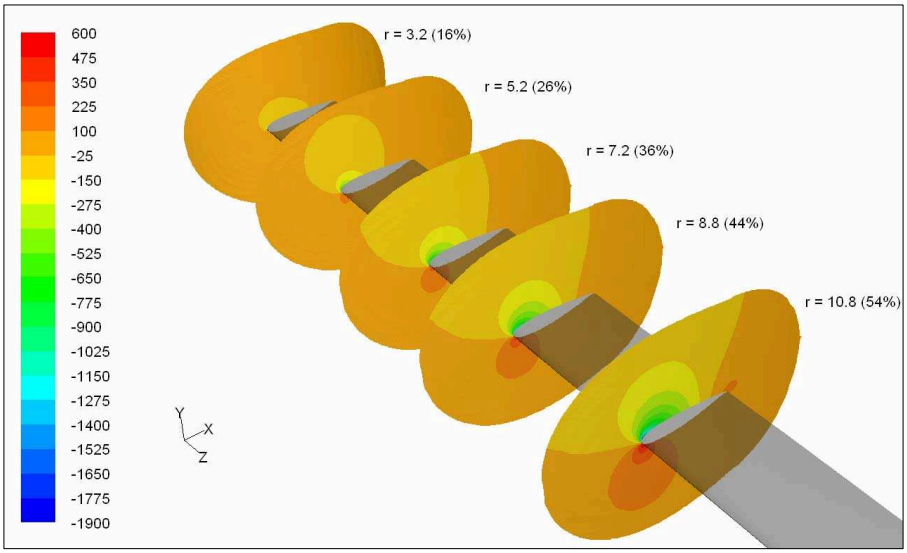

Figure 7.15: *Contours of static pressure p [Pa], radial slices along the cylindrical blade, (U=10 m/s)*

as a thin red-oriented belt around the airfoil sections. Here vorticity is high, non-zero for sure. The boundary layer, initially imperceptible lace gets thicker and thicker while approaching the trailing edge. This being more evident for the suction side, where strong adverse pressure gradients exist. However, the slices provide a vivid description of the different behaviour an airfoil boundary layer flow can experience. The most external section shows almost a symmetric behaviour on the two sides of the airfoil, angle of attack is small and no separation is seen, so that the two boundary layers leave smoothly the trailing edge and combine their selves into a common wake structure. Going inward the flow incidences increase, trailing edge separation occurs on the suction side and it gets closer to the leading edge. At a certain point, which here the internal slice well represents, two local separations occur, one not much after the leading edge and the other at trailing edge. In between the separation bubble that was through streamlines in Figure 7.13 evolves, leading to a much more complex (and *unsteady*) wake structure.

As an example of the post-processing output, the magnitude of the Coriolis and spanwise–convection terms in the governing equations have been evaluated (Figure 7.17). The plotted ratios are, respectively for the crossflow (r_1) and Coriolis (r_2) term

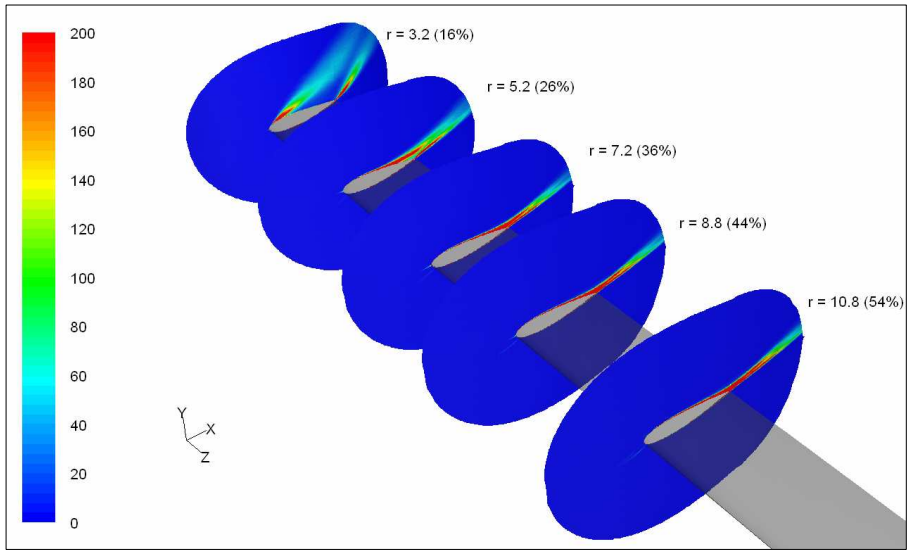

Figure 7.16: *Contours of vorticity magnitude ξ [1/s], radial slices along the cylindrical blade, (U=10m/s)*

$$r_1 = Log\left(\frac{\left|w\frac{\partial u}{\partial z}\right|}{\left|u\frac{\partial u}{\partial x}\right| + \left|v\frac{\partial u}{\partial y}\right|}\right) \tag{7.7}$$

$$r_2 = Log\left(\frac{2\Omega\, w\, \cos\theta}{\left|u\frac{\partial u}{\partial x}\right| + \left|v\frac{\partial u}{\partial y}\right|}\right) \tag{7.8}$$

When separation occurs the rising of both these terms is found and generally Coriolis terms show higher values. The figure above is stemmed from the same simulation, which means that the geometric angle of attack is constant (equal to 10 degrees in that). Since the blade is rotating, different local angles of attack are effectively seen by the blade sections. The higher is the flow incidence, the more inward is the radial distance from the axis. As a consequence, the separation line moves toward the leading edge, along the suction side boundary layer, as approaching the rotational axis. The area depicted in Figure 7.17 is a close up of the boundary layer region, and the local normal-to-wall coordinate is scaled on the computed boundary layer thickness. The very first portion of the airfoil section has not been considered, since the boundary layer is there still rather low and the processed data are badly influenced by the sensible curvature the flow experiences past the leading edge. A more comprehensive analysis on the boundary layer integral properties is still in progress, which could help in finding the most important causes of the rotational effects.

• $r/R = 5.2\,(c/r \cong 0.2) - Re = 1.6 \cdot 10^6 - AOA = 15.2°$

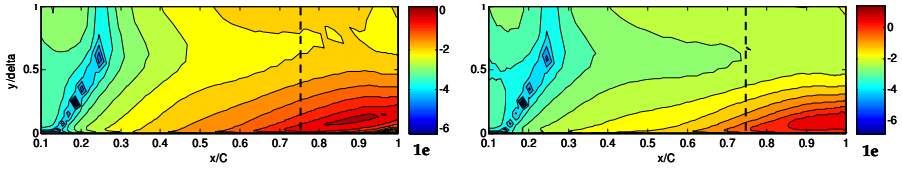

• $r/R = 10.8\,(c/r \cong 0.1) - Re = 3.0 \cdot 10^6 - AOA = 10.5°$

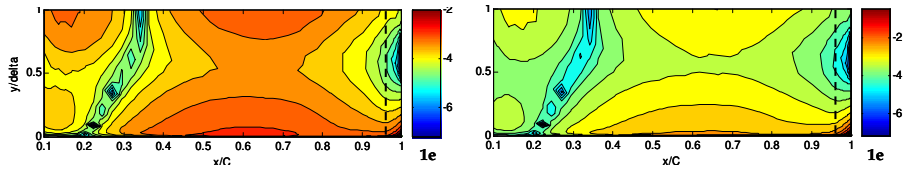

Figure 7.17: *Relative magnitude of crossflow derivative (*left*) and Coriolis term (*right*) in the boundary layer x-momentum equations, in logarithmic scale. Separation is marked with a black dashed line.*

An important result of the post-processing is the evaluation of aerodynamic coefficients (Figure 7.18). It is visible that lift losses are strongly reduced in post-stalled conditions by rotation, as much as higher the flow incidence is. On the other hand we registered higher values of drag coefficients. The results have been compared with a pure 2–D airfoil, showing that 3–D values are higher for the whole range of flow angles. However, the real 3–D rotating results differ from the reference for the lower angles of attack and attached flow conditions. This might be explained because the 2–D section is isolated, while in the corresponding three-bladed rotor the local lift coefficient is increased due to a *cascade* effect. Moreover, in spite of the magnitude of the domain, boundary conditions could play an important role in influencing the flow field. In fact the wind turbine has been modelled as a sort of *ducted* machine, rather than an open–flow rotor like it is in the real case. As is concluded from Figure 7.18, this drawback could be overcome if we regard at a sufficiently outboard section (*e.g.* $r/R = 0.76$) as a reference 2–D situation.

A further comparison was carried out with the Snel *et al.* correction method [48], which is simply based on the square of the local ratio c/r, and on the distance from the linearity of the 2D lift distribution. The r/R=16% section was considered. Under the same inflow characteristcs (AOA, Re), 2D Fluent simulations were run on the NACA0018 airfoil section. The Snel *et al.* correction was applied to the resulting 2D lift distribution, producing the plot in Figure 7.19. Here, the dashed line represents the linear trend of the first part of the 2D curve. The computed 3D results evidence higher values respect to the 2D case all along the range of the flow incidences, much more than the correction method does. Even though, the sensible distance found between the 2D and 3D in the fully separated area, is confirmed by the Snel *et al.* method.

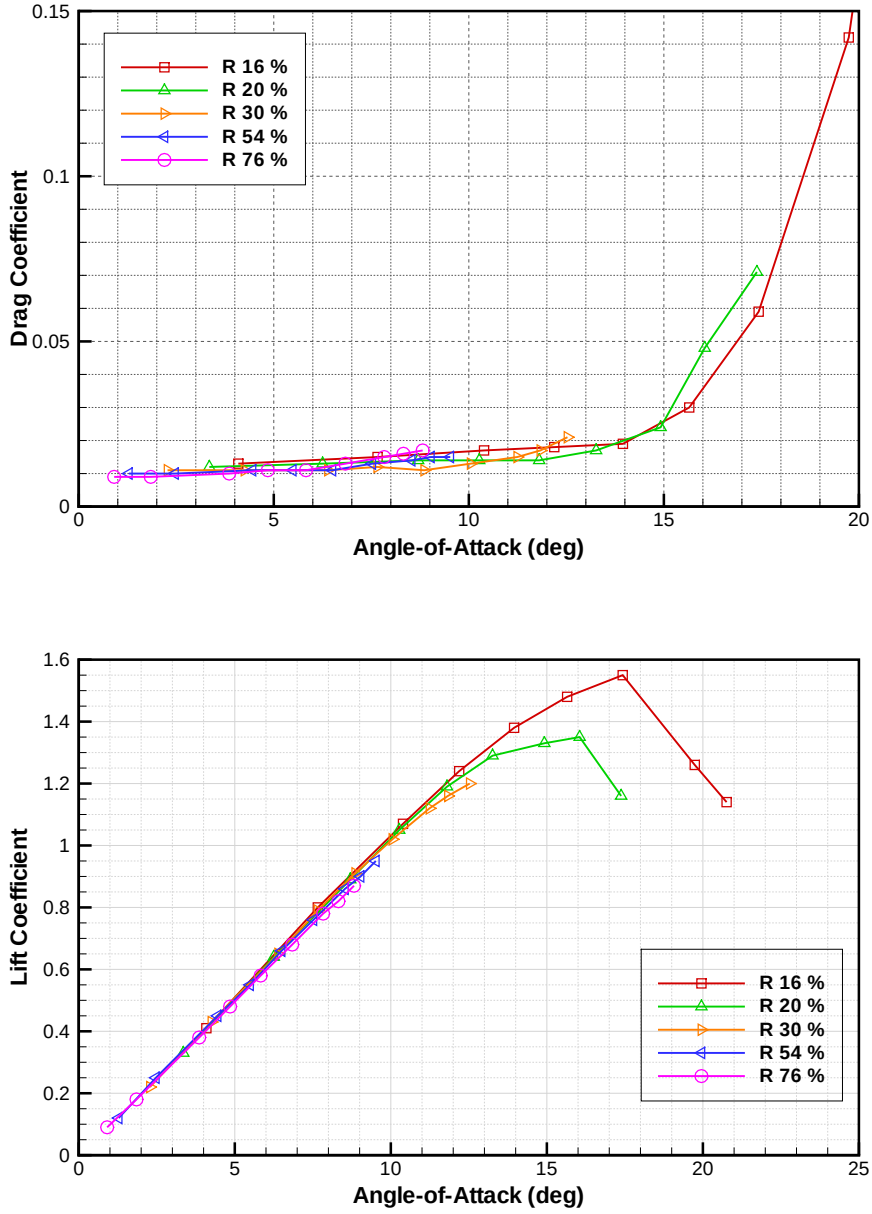

Figure 7.18: *Drag and lift coefficients for the 3–D rotating blade sections at r/R = 0.16, 0.56 and 0.76 and the corresponding 2–D case. In the x-axis is the effective angle of attack*

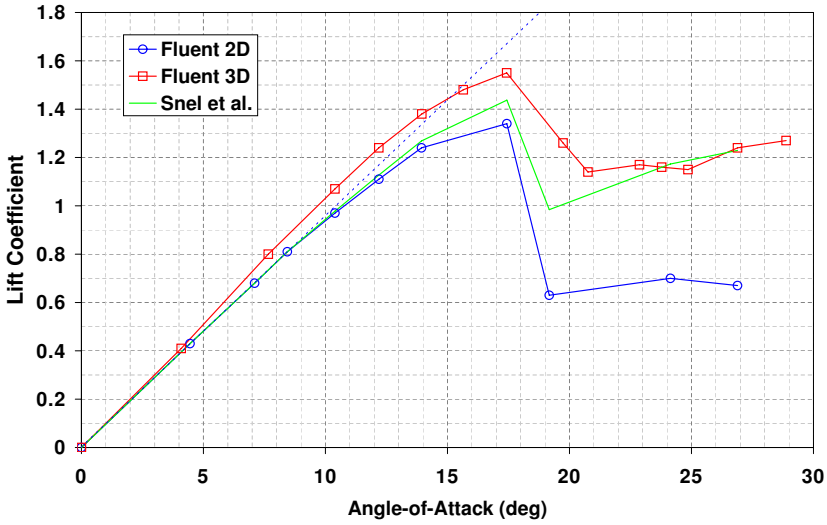

Figure 7.19: *2D and rotating 3D predicted C_L compared to the Snel et al. correction method output for the r/R=16% section, Re = 10^6*

7.3.2 NREL/NASA Ames Rotor

The NASA/NREL rotor computation are recalled now together with the famous experimental case study. The two-bladed model has been simulated under a set of wind conditions ranging from 4 to 12 m/s wind speed and from 1 to 10 % turbulence intensity. Under these conditions, the fixed-pitch (zero degrees at tip) turbine operates first with fully attached flow, then separation starts in the inboard sections and propagates outward from the hub. As approaching the highest velocity, the stalled area covers almost the whole blade and a distinct separation line is visible on the suction side. A depiction of the described behaviour is given by plotting the limiting streamlines on the blade surface (Figure 7.21). For attached flow conditions, *e.g.* mainly for the low speed cases and in the inboard, the limiting streamlines appear parallel, and aligned to the main stream. Hence, the flow pattern follows there a 2D-alike behaviour, as said before referring to Figure 7.13, and already noticed for instance by [25]. On the other, the separated flow portion is characterized by the presence of secondary flow, spanwise oriented.

The blades are coloured with the static pressure magnitude, evidencing the heavier loaded parts, which correspond with the middlespan-outward sections and more if flow is attached, whereas after separation pressure drops fast near to zero. It is interesting to notice the vortex close to the tip, which origins at 8-9 m/s and then gets stronger, and a second eddy structure localized around the middlespan.

A rough comparison could be make with the computed results by Risø and

reported at page 301 in [11] and here in Figure 7.22. The NREL Phase 6 turbine was simulated with a 3 degree tip pitch at 10 m/s, using EllipSys 3D. The picture shows a sudden leading edge separation around $r/R = 0.47$, which resembles the phenomenon occurring in the 10 m/s case of the above results.

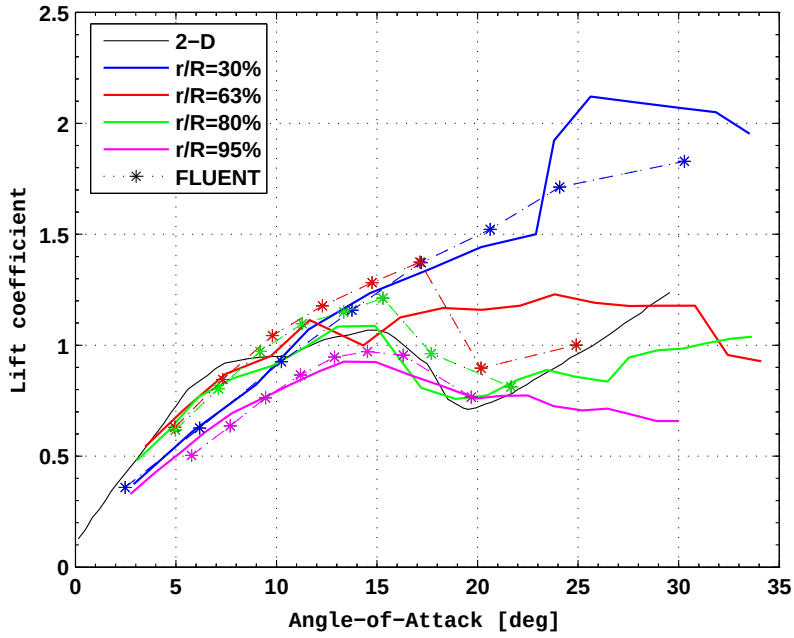

Figure 7.20: *NREL rotor. CL vs. AOA at different spanwise stations. Experimental data are indicated with continuous line, whereas the stars and the dashed line are used for the CFD-RANS results. The local AOA are evaluated according to Shen et al.*

Moreover, the force distributions along the blade have been studied. Four radial sections have been selected, *i.e.* $r/R = 30$, 63, 80 and 95%, that correspond to the instrumented sections of the wind tunnel tests and therefore the measured data are available in there, as well as other computed results are found in literature.

Regarding loads, the computed data output from Fluent solutions are integral forces or continuous pressure distributions. Since we need local force coefficients, the blade should be discretised radially so that the local lift and drag forces can be estimated. For the passage to non-dimensional lift and drag coefficient besides the chord length, the effective apparent velocity seen by the profile section needs to be known both in magnitude and direction . We should evaluate hence the angle-of-attack as was done for the cylindrical blade. The post-processed results are plotted in Figure 7.20.

When comparing the 95% position data the different shape of blade tip

should be accounted for, since our model is simply truncated at the end whereas the original experimental shape is swept at the leading edge, as one evidently figures out from the drawn illustrations.

Figure 7.23 and Figure 7.24 allow further considerations and clarify those already said. Four slices are taken within the domain, corresponding to 4 of the 5 instrumented sections of the NREL experiment, *i.e.* $r/R = 30$, 47, 63 and 80%. Likewise was done for the cylindrical blade, within these radial cuts the physics behind the blade rotation can be carefully analysed. The pressure field is described by means of the pressure coefficients, or pressure to stagnation-pressure (*i.e.* the maximum) ratios within each slice.

In the second plot, the radial velocity component is drawn. What is clearly visible, it is the expected correspondence between the red zones, *i.e.* the highest values of spanwise flow, and the separated boundary layer regions.

7.4 Concluding remarks

The present design approach for wind turbines is typically based on employing the blade–element momentum (BEM) theory, with lift and drag forces determined from 2–D measurements. Although CFD is not a practical design tool, useful suggestions for classical design codes can be derived, based on a quantitative explanation of rotational phenomena.

In this thesis the full CFD–RANS approach has been followed to solve the flow field past the rotating blade of a wind turbine blade and for investigating the rotational effects in its the boundary layer.

A useful post-processing tool for studying the local velocity profiles and for evaluating quantitatively the terms of interest in the boundary layer equations has been implemented. For instance, the integral properties of boundary layer will be analysed in order to find practical suggestions for design procedures. The early results for a simple blade geometry have been presented, confirming that 3–D loads on a rotating blade are higher than the corresponding non-rotating case, mostly for inboard sections and separated flow conditions. Then the well-known NASA/NREL Phase VI wind turbine was considered and a analogous CFD-RANS study was carried out with this geometry. The main findings of the cylindrical blade study were confirmed, even if new compliances were introduced by the more realistic rotor model. Thus, the post-processing analysis resulted more to be proper regarding the simpler blade.

A more detailed analysis of the results is needed. Further flow situations (Reynolds number, angle of attack and rotational speed) will be studied for the simpler geometry and pitched operation will be explored with the NREL rotor.

The planned development includes the implementation of a BEM-correction model, to be compared with the existing examples.

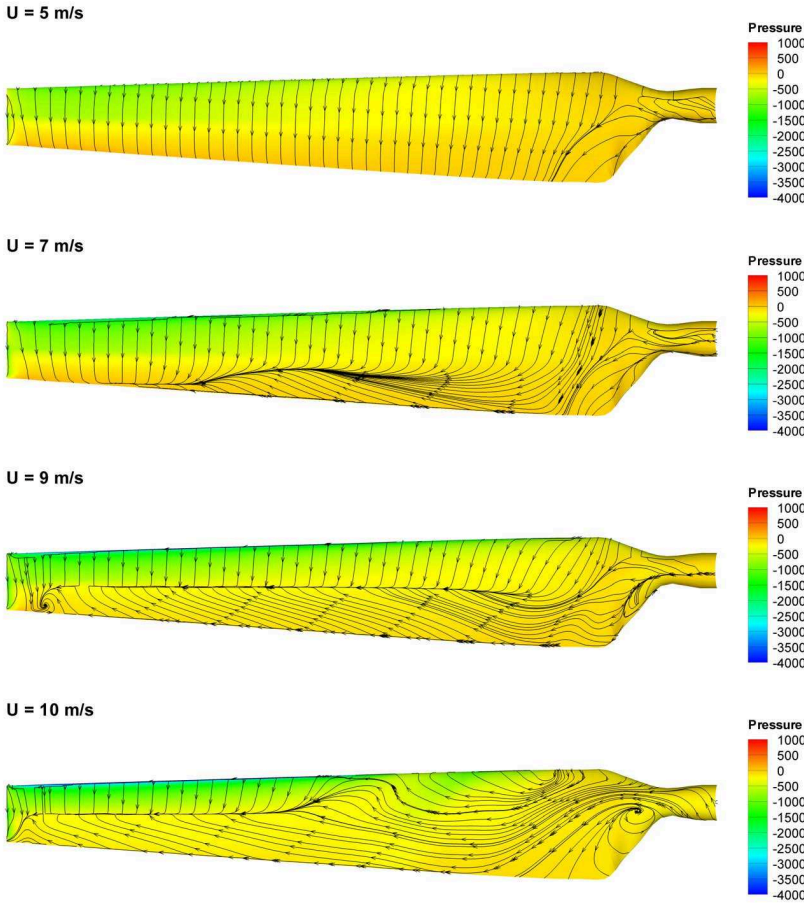

Figure 7.21: *NREL Rotor. Limiting streamlines on blade suction side for different wind speed, coloured with the static pressure levels.*

Figure 7.22: *Limiting streamlines on the NREL Phase- VI rotor for the 10 m/s axial case. RISOE EllipSys 3D Computations*

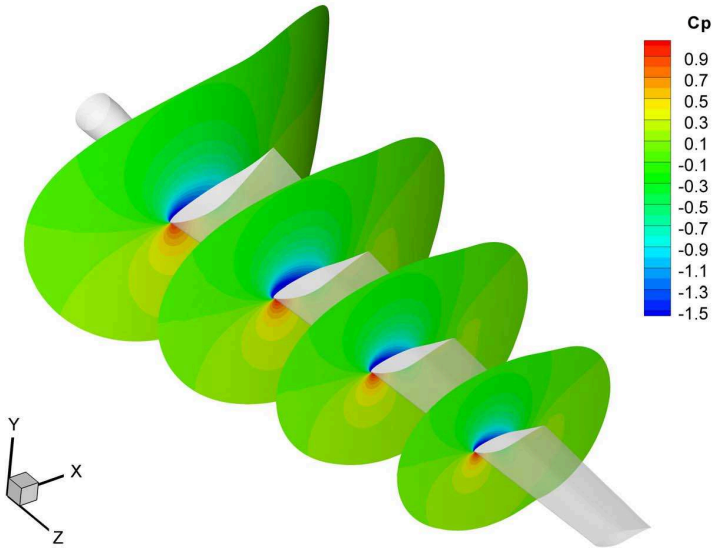

Figure 7.23: *NREL rotor Cp distribution at different spanwise stations (r/R = 30%, 47%, 63%, 80%), U = 7 m/s*

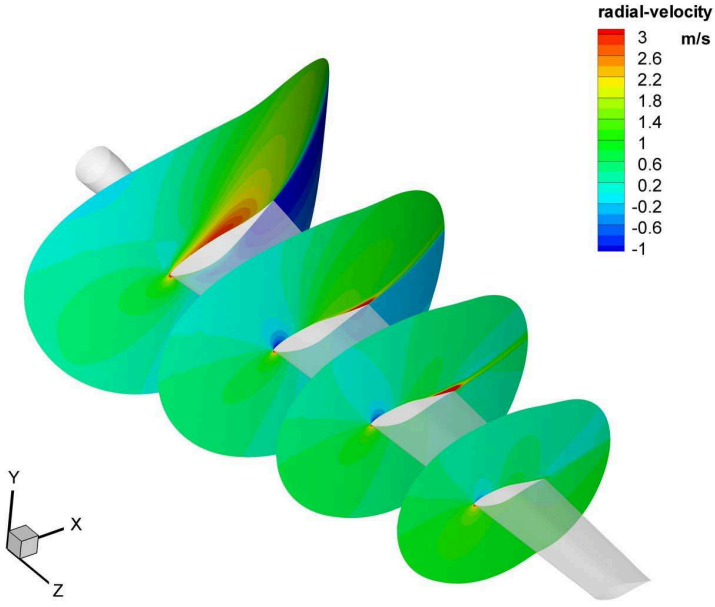

Figure 7.24: *NREL rotor radial velocity component at different spanwise stations (r/R = 30%, 47%, 63%, 80%), U = 7 m/s*

Chapter 8

Conclusions and future work

The aim of the project was to produce a review and to get a better understanding of wind turbine blades aerodynamics, by means of a wide-range CFD-RANS simulation campaign. Several issues were addressed, mainly regarding the blade inboard and tip design, the boundary layer and the near wake flow. The results from the computations were quite satisfactory and, in our opinion, they can represents a good foundation for future work in this area. The more significant findings are summarized below.

- The capabilities of CFD-RANS methods for computing performances and loads on wind turbine blade were verified. However, the agreement with referenced data was better for attached flow and in the proximity of nominal conditions, for which steady computations are sufficient and even a wall-function approach to the boundary layer flow gives good results as well as simpler turbulence models (*e.g.* the one-equation Spalart-Allmaras).

- A broad description of the flow field past the rotating blade of a wind turbine was given by postprocessing the CFD data. Diagrams and plots of velocity, induced velocity, vorticity, pressure etc. were presented, which are suitable for understanding the physical problem.

- The issue of exploring the capabilities of CFD for design optimization was addressed. The innovative hub connection adopted by some modern wind turbines was studied, and the improvements are shown in terms of global performances. Also, the study focussed on evaluating the advantages of a tapered geometry for the blade tip and the complex mechanism of the tip vortex was investigated in detail. The study confirmed the possibility to use the CFD as an analysis tool for innovative design.

- A wake analysis was also carried out. Both the near and far wake velocity field have been described, and the most significant features of the vortex structure have been predicted. Even if promising results were obtained

in capturing the mean values, some discrepancies arose in predicting the turbulence decay. Thus, we must conclude by considering a real challenge the complete discovering of wind turbine wake dynamics by CFD-RANS.

- The flow field past the rotating blade of a wind turbine and the rotational effects on its boundary layer were investigated by a full CFDŨRANS approach. The early results for both a simple blade geometry and the well-known NREL Phase VI test case were presented, confirming that 3–D loads on a rotating blade are higher than the corresponding non-rotating case, mostly for inboard sections and separated flow conditions. A post-processing tool for evaluating quantitatively the terms of interest in the boundary layer equations has been implemented, and a database of solution cases has been provided.

8.1 Future work

Further investigation are needed to address the open questions. Future work should be aimed mainly at

- Simulation on the real LM19.l blade and on the NREL blade in pitched operation should be carried out to further validate the numerical method.
- The methods presented in this study can be applied to an extensive experimental case like the *MEXICO* project database, in order to firmly validate and to improve them. In the past the lack of complete measurements caused often the numerical studies to be incomplete or to introduce strong simplifications.
- More extensive unsteady computation analysis is suggested and DES and LES techniques, which now become affordable, can be explored. This might be useful for the wake analysis and the deep stall operating conditions, where strong unsteadiness exists.
- A more advanced analysis is required on the existing database, for achieving the goal of a BEM-correction model based on the rotational effects. For instance, the integral properties of the boundary layer will be carefully reviewed.

List of publications

Published in journals

- Mandas, N., Cambuli, F., **Carcangiu, C.E.**, The Economy of Large Scale Wind Turbines, 2005, Fluent News, Fluent Inc., Vol. XV, Summer

Published in proceedings

- Cambuli, F., **Carcangiu, C.E.**, Mandas, N., Studio Numerico del Flusso su Rotori Eolici ad Asse Orizzontale (*Italian*), 60^{th} Convegno ATI, Roma, 13-15 September 2005
- Mandas, N., Cambuli, F., **Carcangiu, C.E.**, Numerical Prediction of Horizontal Axis Wind Turbine Flow, Proceedings of the European Wind Energy Conference and Exhibition 2006, Athens, 27 February - 2 March
- **Carcangiu, C.E.**, Sørensen, J.N., Cambuli, F., Mandas, N., CFD-RANS analysis of the rotational effects on the boundary layer of wind turbine blades, Proc. of 2^{nd} Conference on Making Torque from Wind, Lyngby (DK), 28-31 Aug (J. of Physics: Conference Edition 2007)

Presented at conferences

- Mandas, N., Cambuli, F., **Carcangiu, C.E.**, Numerical Prediction of Horizontal Axis Wind Turbine Flow (poster), Conferenza d'ateneo sulla ricerca scientifica, Università di Cagliari, 15 March 2006
- **Carcangiu, C.E.**, Sørensen, J.N., Cambuli, F., Mandas, N., CFD-RANS analysis of the rotational effects on the boundary layer of wind turbine blades, 11^{th} DCAMM symposium, Silkeborg - DK, 19-21 March 2007
- **Carcangiu, C.E.**, Sørensen, J.N., Cambuli, F., Mandas, N., CFD-RANS analysis of the rotational effects on the boundary layer of wind turbine blades, Dansk Vindkraftkonference 2007, Trinity, Snoghøj, Fredericia, 25-27 April 2007

References

[1] VV.AA. Annual report. Technical report, EWEA, European Wind Energy Agency, 2006.

[2] VV.AA. Wind energy annual report. Technical report, IEA, International Energy Agency, 2006.

[3] Hau E. *Windturbines*. Springer: Berlin, 2000.

[4] Gasch R. and Twele J. *Wind Power Plants*. Solarpraxis: Berlin – James & James: London, 2002.

[5] VV.AA. Global wind 2006 report. Technical report, GWEA, Global Wind Energy Council, 2006.

[6] Sørensen J.N. and Shen W.Z. Numerical modeling of wind turbine wakes. *Journal of Fluid Engineering*, 124:393–9, 2002.

[7] Vermeer L.J. Sørensen J.N. and Crespo A. Wind turbine wake aerodynamics. *Progress in Aerospace Sciences*, 39:467–510, 2003.

[8] Burton T. Sharpe D. Jenkins N. and Bossanyi E. *Wind Energy Handbook*. John Wiley & Sons Ltd: Chichester, 2001.

[9] Ivanell S.S.A. *Numerical Computations of Wind Turbine Wakes*. PhD thesis, KTH Mechanics, Royal Institute of Technology, Stockholm, Sweden, 2005.

[10] Hansen A.D. and Hansen L.H. Wind turbine concept market penetration over 10 years (1995-2004). *Wind energy*, 10(1):81–97, 2007.

[11] Hansen M.O.L. Sørensen J.N. Voutsinas S. Sørensen N. and Madsen H.Aa. State of the art in wind turbine aerodynamics and aeroelasticity. *Progress in Aerospace Sciences*, 42:285–330, 2006.

[12] Hansen M.O.L. *Aerodynamics of Wind Turbines. Rotors, Load and Structures*. James & James: London, 2000.

[13] Hansen M.O.L. Sørensen N.N. Sørensen J.N. and Michelsen J.A. Extraction of lift, drag and angle of attack from computed 3-D viscous flow around a rotating blade. In *Proceedings of EWEC 97: Dublin*, pages 499–502, 1997.

[14] Sørensen J.N. *Three-level viscous-inviscid interaction technique for the prediction of separated flow past rotating wings.* PhD thesis, DTU, Technical University of Denmark, 1986.

[15] Mikkelsen R. *Actuator disc methods applied to wind turbines.* PhD thesis, Technical University of Denmark: PhD Dissertation, 2003.

[16] Arakawa C. Fleigl O. Iidal M. and Shimooka M. Numerical approach for noise reduction of wind turbine blade tip with Earth Simulator. *Journal of the Earth Simulator*, 2(March):pp. 11–30, 2005.

[17] Sørensen N.N. Johansen J. and Conway S. CFD computations of wind turbine blade loads during standstill operation. KNOW–BLADE Task 3.1. Technical Report R-1465, Risø National Laboratory Roskilde - DK, 2004. June.

[18] Iida M. Shimooka M. and Arakawa C. Basic study of winglet effects on aerodynamics and aeroacoustics using Large-Eddy Simulation. In *Proceedings of EWEC 06: Athens*, 2006.

[19] Anderson J.D.Jr. *Computational Fluid Dynamics.* McGraw-Hill Inc.: New York, 1995.

[20] Versteeg H.K. and Malalasakera W. *An Introduction to Computational Fluid Dynamics: The Finite-Volume Method.* Harlow : Longman Scientific & Technical: New York, 1995.

[21] Ferziger J.H. and Peric M. *Computational Methods for Fluid Dynamics.* Springer-Verlag: Berlin, 1999.

[22] Batchelor G.K. *An Introduction to Fluid Dynamics.* Cambridge University Press, 1967.

[23] Benjanirat S. Sankar L.N. and Xu G. Evaluation of turbulence models for the prediction of wind turbine aerodynamics. In *Proc. of 41st AIAA Aerospace Sciences Meeting and Exhibit*, volume 517, 2003.

[24] VV.AA. Fluent 6.3 Documentation, user's guide. Technical report, ANSYS Inc., 2006.

[25] Kang S. and Hirsch C. Features of the 3D flow around wind turbine blades based on numerical solutions. In *Proceedings of EWEC 06: Copenhagen*, 2001.

[26] Alinot C. and Masson C. Aerodynamic simulation of wind turbines operating in atmospheric boundary layer with various thermal stratifications. In *Proc. of 40th AIAA Aerospace Sciences Meeting and Exhibit*, pages 1–10, 2002.

[27] Xu G. and Sankar L.N. Computational study of HAWT. In *Proc. of 37th AIAA Aerospace Sciences Meeting and Exhibit*, volume 48, 1999.

[28] Xu G. and Sankar L.N. Effects of transition, turbulence and yaw on the performance of hawt. In *Proc. of 38th AIAA Aerospace Sciences Meeting and Exhibit*, volume 48, 2000.

[29] Benjanirat S. and Sankar L.N. Recent improvements to a combined navier–stokes full potential methodology for modeling hawts. In *Proc. of 42nd AIAA Aerospace Sciences Meeting and Exhibit*, volume 830, 2004.

[30] Sørensen N.N. 3-D background aerodynamics using CFD. Technical Report R-1376, Risø National Laboratory Roskilde - DK, 2002. Dec.

[31] Sørensen N.N. *et al.* Tip shape study. Technical Report R-1495, Risø National Laboratory Roskilde - DK, 2005. Jan.

[32] Rohden R. Revolutionary blade design. *Wind Blatt, the Enercon Magasine*, 03, 2004.

[33] Anderson D.A. Tannehill J.C. and Pletcher R.H. *Computational Fluid Mechanics and Heat Transfer.* Taylor & Francis: New York, 1997.

[34] Abbott J.H. and Von Dohenoff A.E. *Theory of wind sections.* Dover Publications Inc.: New York, 1959.

[35] Sørensen N.N. Transition Prediction on the NORDTANK 500/41 Turbine Rotor. Technical Report R-1365, Risø National Laboratory Roskilde - DK, 2002. September.

[36] Johansen J. and Sørensen N.N. Airfoil characteristics from 3-D CFD rotor computations. *Wind Energy*, 7:283–94, 2004.

[37] Hand M.M. Simms D.A. Fingersh L.J. Jager D.W. Cotrell J.R. Schreck S. and S.M. Larwood. Unsteady aerodynamics experiment phase–vi: Wind tunnel test configurations and available data campaigns. Technical Report NREL/TP-500-29955, NREL, 2001. December.

[38] Johansen J. Madsen H.A. Sørensen N.N. and Bak C. Numerical investigation of a wind turbine rotor with an aerodynamically redesigned hub-region. In *Scientific Proceedings of EWEC 06: Athens*, pages 37–41, 2006.

[39] De Vries O. Fluid dynamics aspects of wind energy conversion. Technical Report AG–243, AGARD, 1979.

[40] Madsen H.A. and Fuglsang P. Numerical investigation of different tip shapes for wind turbine blades: Aerodynamic and aeroacoustic aspects. Technical Report R-891, Risø National Laboratory Roskilde - DK, 1996. Dec.

[41] Johansen J. and Sørensen N.N. Numerical investigation of three wind turbine blade tips. Technical Report R-1353, Risø National Laboratory Roskilde - DK, 2002. Aug.

[42] Johansen J. and Sørensen N.N. Aerodynamic investigation of winglets on wind turbine blades using CFD. Technical Report R-1543, Risø National Laboratory Roskilde - DK, 2006. Feb.

[43] Snel H. Schepers J. G. and Montgomerie B. The MEXICO project (model experiments in controlled conditions) - the database and first results of data processing and interpretation. In *Proc. of The Science of Making Torque (J.of Physics - Conference Series)*, volume 75, pages 1–11, 2007.

[44] Hahm T. and Kröning J. In the wake of a wind turbine. *Fluent News*, XI(I)(Spring):5–7, 2002.

[45] Ruith M.R. Shashidhar S. Vishak T. and Kumar R. A powerful wind of change. *Fluent News*, Fall:4–5, 2004.

[46] Troldborg N. Sørensen J.N. and Mikkelsen R. Determination of Angle-of-Attack (AOA) for rotating blades. In *Proc. of The Science of Making Torque (J.of Physics - Conference Series)*, volume 75, pages 1–15, 2006.

[47] Wilson R.E. and Lissaman P.B.S. *Applied Aerodynamics of Wind Power Machines*. Oregon State University, 1974.

[48] Snel H. Houwink R. Bosschers J. Piers W.J. van Bussel G.J.W. and Bruining A. Sectional prediction of 3D effects for stalled flow on rotating blades and comparison with measurements. In *Proceedings of EWEC 93: Lübeck-Travemunde*, pages 395–9, 1993.

[49] Harris F.D. Preliminary study of radial flow effects on rotor blades. *Journal of the American Helicopter Society*, 11(3):1–21, 1966.

[50] Himmelskamp H. *Profile investigation on a rotating airscrew*. PhD thesis, Göttingen University: PhD Dissertation, 1945.

[51] Ronsten G. Static pressure measurements on a rotating and non-rotating $2.375m$ wind turbine blade. comparison with 2D calculations. *Journal of Wind Engineering and Industrial Aerodynamics*, 39(1–3):105–18, 1966.

[52] Tangler J.L. and Kocurek J.D. Wind turbine post-stall airfoil performance characteristics guidelines for blade-element momentum methods. In *Proc. of 43^{rd} AIAA Aerospace Sciences Meeting and Exhibit*, volume 591, pages 1–10, 2005.

[53] Schlichting H. *Boundary layer theory.* McGraw-Hill: New York, 1955.

[54] Sears W.R. Potential flow around a rotating cylindrical blade. *Journal Aeronautical Sciences: Readers' Forum*, 17(3):183, 1950.

[55] Fogarty L.E. and Sears W.R. Potential flow around a rotating, advancing cylinder blade. *Journal Aeronautical Sciences: Readers' Forum*, 17(9):599, 1950.

[56] Fogarty L.E. The laminar boundary layer on a rotating blade. *Journal Aeronautical Sciences: Readers' Forum*, 18(4):247, 1951.

[57] Banks W.H.H. and Gadd G.E. Delaying effects of rotation on laminar separation. *AIAA Journal*, 1(4):941–2, 1963.

[58] McCroskey W.J. and Dwyer H.A. Methods of analyzing propeller and rotor boundary layers with crossflows. Technical Report SP–228, NASA, 1969. 473–514.

[59] Sørensen J.N. Prediction of the three-dimensional stall on wind turbine blade using three-level, viscous-inviscid interaction model. In *Proceedings of EWEC 86: Rome*, pages 429–35, 1986.

[60] Shen W.Z. and Sørensen J.N. Quasi-3D Navier-Stokes model for a rotating airfoil. *Journal of Computational Physics*, 150:518–48, 1999.

[61] Chaviaropoulos P.K. and Hansen M.O.L. Three-dimensional and rotational effects on wind turbine blades by means of a quasi-3D Navier-Stokes solver. *Journal of Fluid Engineering*, 122:330–6, 2000.

[62] Du Z. and Selig M.S. The effect of rotation on the boundary layer of a wind turbine blade. *Renewable Energy*, 20:pp. 167–81, 2000.

[63] Hu D. Hua O. and Du Z. A study on stall-delay for horizontal axis wind turbine. *Renewable Energy*, 31:821–36, 2006.

[64] Lindenburg C. Modelling of rotational augmentation based on engineering considerations and measurements. In *Proceedings of EWEC 04: London*, 2004.

[65] Bak C. Johansen J. and Andersen P.B. Three-dimensional corrections of airfoil charcteristics based on pressure distributions. In *Proceedings of EWEC 06: Athens*, 2006.

[66] Shen W.Z. Hansen M.O.L. and Sørensen J.N. Determination of Angle-of-Attack (AOA) for rotating blades. In *Proc. of Euromech Colloquium (Wind Energy)*, pages 205–9, 2006.

[67] Stock H.W. and Haase W. Feasibility study of e^N transition prediction in Navier-Stokes methods for airfoils. *AIAA Journal*, 37(10):1187–96, 1999.

Appendix A

BEM-designed turbine blade

Computed chord and twist distributions for the BEM-designed wind turbine blade follow.

Table A.1: *Chord and twist distributions computed with BEM*

Radius [m]	Airfoil section	Chord [m]	Twist angle [deg]
2.050	NACA 63-421	2.995	28.500
2.511	NACA 63-421	2.813	24.616
3.433	NACA 63-421	2.489	18.812
4.355	NACA 63-421	2.145	14.672
5.277	NACA 63-421	1.864	11.585
6.200	NACA 63-418	1.607	9.187
7.122	NACA 63-418	1.397	7.260
8.044	NACA 63-418	1.227	5.672
8.966	NACA 63-418	1.088	4.343
9.889	NACA 63-418	0.974	3.220
10.811	NACA 63-418	0.881	2.267
11.733	NACA 63-418	0.804	1.461
12.655	NACA 63-418	0.741	0.890
13.578	NACA 63-418	0.688	0.480
14.500	NACA 63-418	0.643	0.220
15.422	NACA 63-418	0.605	0.078
16.344	NACA 63-418	0.592	0.020
17.267	NACA 63-412	0.563	0.005
18.189	NACA 63-412	0.536	0.003
19.111	NACA 63-412	0.511	0.002
20.033	NACA 63-412	0.487	0.000
20.500	NACA 63-412	0.469	0.000

Appendix B

Rotating boundary layer post-processing tool

All the post-processing codes were implemented in MATLAB. In the following, the tool for the transformation of the primitive data into a set of variable in the local boundary layer system of coordinate (Figure 7.3) is described, including also the determination of the effective angle-of attack. The procedures are briefly summarized, since some of the main topics have been already presented, mainly in Chapter 7.

The data file imported from Fluent included the following variables:

- node number
- x, y, z coordinate
- axial, radial, relative-tangential velocity
- vorticity magnitude
- x, y wall-shear stress
- radial-coordinate
- boundary-normal distance

Three constant–radius cut planes were imported from Fluent (Figure 7.9, including the former listed variables. A list of further input was thus required:

- Rotational speed
- Geometric AOA
- Fluid density and viscosity

The "undisturbed" velocity components were computed from geometric consideration, and data sorting follows.

According with the value of the cell boundary normal distance (BND), matrices were built where the row and the columns corresponded to the desired geometric i, j indices (Figure 7.10). For boundary normal distance equal to zero the airfoil coordinates were identified, which determined also the maximum i index, *i.e.* one size in the matrix N. Thus, being the nodes aligned in rows for nearly constant BND, at each "level" of wall distance, a row of N-element was filled in the matrix.

A function was made for computing the normal and tangential to the wall directions (a 2^{nd} order polynomial fitting of a 5 nodes stencil), which is therefore expressed through a local θ angle.

The boundary layer thickness was evaluated as well with a subfunction, with checking both the vorticity magnitude and the velocity gradient values along the normal direction. The last technique has been suggested by Stock and Haase [67] and it is based on the behaviour of the diagnostic function F

$$F = Y^a \left[\frac{dU}{dY}\right]^b \tag{B.1}$$

The boundary-layer thickness was then defined as follows

$$\delta = \epsilon \; Y_{max} \tag{B.2}$$

where Y_{max} is the wall distance for which $F = F_{max}$. In the Matlab code the values of expression B.1 were evaluated throughout the grid and for each i-position the maximum of the function was found and the corresponding j-position was saved. This position was the Y_{max} we needed for computing the BL thickness. Through numerical experimentation, the constants a, b have been determined by the same authors and a nearly unique value for ϵ in all different considered cases has been produced, resulting in the values presented in Table B.1

Table B.1: *Parameters for computing the BL thickness according to [67]*

	Laminar BL	**Turbulent BL**
a	3.9	1
b	1	1
ϵ	1.294	1.938

The separation point, where present, was found for negative normal to wall tangential velocity gradient $\partial u/\partial y$.

All the derivatives in the curvilinear coordinates were estimated taking a 2^{nd} order CDS polynomial fitting of the output data for non–uniform spaced grids Figure B.1, for a variable ϕ reads [21]

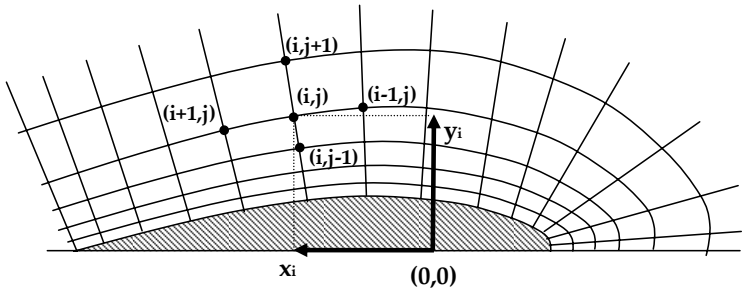

Figure B.1: *Computing derivatives*

$$\left(\frac{\partial\phi}{\partial x}\right)_i = \frac{\Delta x_{i+1}\Delta x_i\left(\Delta x_i + \Delta x_{i+1}\right)}{\phi_{i+1}\left(\Delta x_i\right)^2 - \phi_{i-1}\left(\Delta x_{i+1}\right)^2 + \phi_i\left[\left(\Delta x_{i+1}\right)^2 - \left(\Delta x_i\right)^2\right]} \tag{B.3}$$

where $\Delta x_i = x_i - x_{i-1}$ and $\Delta x_{i+1} = x_{i+1} - x_i$, or referring to Figure B.1

$$dx_i = \sqrt{\left(\bar{y}_{i,j} - \bar{y}_{i-1,j}\right)^2 + \left(\bar{x}_{i,j} - \bar{x}_{i-1,j}\right)^2} \tag{B.4}$$

$$dx_{i+1} = \sqrt{\left(\bar{y}_{i+1,j} - \bar{y}_{i,j}\right)^2 + \left(\bar{x}_{i+1,j} - \bar{x}_{i,j}\right)^2} \tag{B.5}$$

and similarly for the j-derivatives terms.

The terms in the governing equation were computed as products and sums of the available variables and derivatives in the new system of coordinates. See for instance the expression 7.8 at page 93.

Pressure coefficient distribution were also given.

Finally, a section of the code allows the plot to be drawn automatically.

The 2-D simulation cases were likewise post-processed, but a few changes in the code have been made for the scope.

Evaluating the effective Angle-of-Attack

As previously said in section 7.2.4 for computing the effective AOA the technique proposed by Shen *et al.* [66], which is based on the determination of the local induced velocities created by bound vortices, was followed in this project for the scope. It consists of an iterative process. The blade and the flow field around are subdivided into n annuli between the minimum and the maximum radius.

As an input the following properties are needed for a series of control points taken in front of each resulting blade section leading edge, neither far away nor

too close respect to the nose (we chose a distance of 2 chords). The input set includes

- x, y, z, coordinates of control points
- θ, angular coordinate
- V_a, V_θ, axial velocity, relative-tangential velocity

Moreover, the cartesian coordinates of the aerodynamic centres are taken. From Fluent solution data the normal and tangential forces are imported for each annulus.

Finally the incoming undisturbed velocity profile is inserted into the code, together with the following scalar inputs

- c_i, chord length/lengths (if not constant)
- Ω, rotational speed
- θ_p, pitch angle
- ρ, air density
- e, the desired tolerance for the convergence process

STEP 1

A set of initial flow angles and corresponding relative-velocity magnitudes is computed for the i-annuli, *i.e.* at every control point

$$\Phi_i^0 = tan^{-1}\left(\frac{V_{z,i}}{V_{\theta,i}}\right) \tag{B.6}$$

$$V_{rel,i}^0 = \sqrt{V_{z,i}^2 + V_{\theta,i}^2} \tag{B.7}$$

The iterative cycle starts.

STEP 2

Lift and drag forces are estimated for the i-annuli using the previous angles of attack and the computed local blade forces

$$L_i^n = F_{z,i} cos\phi^n - F_{\theta,i} sin\phi^n \tag{B.8}$$

$$D_i^n = F_{z,i} sin\phi^n - F_{\theta,i} cos\phi^n \tag{B.9}$$

STEP 3

Circulation magnitude is computed for the i-annuli from the estimated lift forces

$$\Gamma_i^n = \frac{L_i^n}{\rho\sqrt{\Omega^2 r^2 + V_0^2}} \tag{B.10}$$

where V_0 denotes wind speed and Ω is the angular velocity of the rotor. Being the $\vec{G}$ vector z-oriented, it is hence $\vec{G}_i = [0, 0, G_i]$

STEP 4
The induced velocity vector created by bound vortex is computed for the i-annuli using circulations

$$u_i^n(x) = (u_x^n, u_y^n, u_z^n)_i = \frac{1}{4\pi}\sum_{j=1}^{NB}\int_0^R \Gamma^n(y) \times \frac{(x-y)}{|x-y|^3} dr \tag{B.11}$$

and in curvilinear coordinates is

$$u_{\theta,i}^n = u_{x,i}^n cos\theta + u_{z,i}^n sin\theta \tag{B.12}$$

$$u_{\theta,i}^n = -u_{x,i}^n sin\theta + u_{z,i}^n cos\theta \tag{B.13}$$

STEP 5
The new flow angles and relative velocities are computed for the i-annuli

$$\Phi_i^{n+1} = tan^{-1}\left(\frac{V_{z,i} + u_{z,i}^n}{V_{\theta,i} + u_{\theta,i}^n}\right) \tag{B.14}$$

$$V_{rel,i}^{n+1} = \sqrt{\left(V_{z,i} + u_{z,i}^n\right)^2 + \left(V_{\theta,i} + u_{\theta,i}^n\right)^2} \tag{B.15}$$

STEP 6
Convergence is checked as follows

$$max\left|V_{rel,i}^{n+1} - V_{rel,i}^n\right| < e \tag{B.16}$$

If verified, the iterative cycle ends otherwise the procedure needs to go back to STEP 2.

The output includes the effective AOA, lift and drag coefficients:

$$\alpha_i = \Phi_i - \beta_i \tag{B.17}$$

$$C_{l,i} = \frac{2L_i}{\rho V_{rel,i}^2 c_i} \tag{B.18}$$

$$C_{d,i} = \frac{2D_i}{\rho V_{rel,i}^2 c_i} \tag{B.19}$$

where β_i is the sum of the pitch and twist angles and c_i is the chord.